Multipass Beam Breakup Study at Jefferson Lab for the 12 GeV CEBAF Upgrade

Ilkyoung Shin, Ph.D.

University of Connecticut, 2013

Recirculating linear accelerators (linacs) provide a compact and efficient way of accelerating particle beams to medium and high energies by reusing the same linac for multiple passes. In recirculating linacs, maximum current can be limited by multipass beam breakup (BBU), which occurs when an electron beam interacts with the higher order modes (HOMs) of accelerating cavities during multipass recirculations.

The average current of the CEBAF 12 GeV Upgrade accelerator at Jefferson Lab, a 5-pass recirculating linac, may be limited by multipass BBU. This dissertation work was performed as part of the 12 GeV Upgrade project at Jefferson Lab to investigate limits on average beam currents from the BBU instability. Experimental and simulation studies were carried out, and revealed that the multipass BBU will not be a limiting factor to the average beam current in the 12 GeV Upgrade of the CEBAF accelerator.

This dissertation includes the theoretical calculation for longitudinal BBU, which revealed that the maximum current limit from longitudinal BBU is much higher than the transverse one. Therefore, longitudinal BBU will not become a problem, as long as transverse BBU does not cause instability. A cumulative BBU simulation study for a new injector in the 12 GeV accelerator also was conducted. The results showed that the transient behavior of cumulative BBU in the injector is not problematic.

Multipass Beam Breakup Study at Jefferson Lab for the 12 GeV CEBAF Upgrade

Ilkyoung Shin

B.S., Kyungpook National University, 1998

M.S., Kyungpook National University, 2000

A Dissertation

Submitted in Partial Fulfillment of the

Requirements for the Degree of

Doctor of Philosophy

at the

University of Connecticut

2013

APPROVAL PAGE

Doctor of Philosophy Dissertation

Multipass Beam Breakup Study at Jefferson Lab for the 12 GeV CEBAF Upgrade

Presented by

Ilkyoung Shin,

Major Advisor

Kyungseon Joo

Associate Advisor

Richard Jones

Associate Advisor

Todd Satogata

University of Connecticut

2013

To my youth and efforts, and for my future.

ACKNOWLEDGEMENTS

First and foremost, I must thank my advisor, professor Kyungseon Joo, who has given me a precious opportunity to study at the University of Connecticut and tremendous help over the past 6 years. I really appreciate his time and support in pursuing my Ph.D. Special thanks must go to my JLab sponsor, Byung Yunn, who has provided me tremendous amount of advice and physical insights during my research. I must also thank Todd Satogata, who served as the experiment director as well as my advisory committee member. I benefited is not only his deep understanding of accelerator physics but also his great personality and attitudes for research. The inspiration from him will last for the rest of my life.

Many thanks must go to the director of the Center for the Advanced Studies of Accelerators (CASA), Geoffrey Krafft. It was a great privilege to work in such a fascinating environment surrounded by great physicists in the CASA group. There are a number of individuals who helped me over the past several year. That help was indispensable for my research and I am grateful to all of them. They are Alex Bogacz, Michael Tiefenback, Yves Roblin, Mike Spata, Balsa Terzic, Yaroslav Derbenev, Alicia Hofler, Vasiliy Morozov, Edward Nissen, Rui Li, Fanglei Lin, and Yuhong Zhang. I would also like to thank Haipeng Wang, Frank Marhauser, Mircea Stirbet, and Jiquan Guo in the SRF group for introducing me to the field

of an RF engineering and providing many comments, advice, and help.

I am grateful to other graduate students who helped me to cure my homesickness and loneliness in the US: Ryan Bodenstein, Danial Bowring, Paul Matione, and other friends. Ryan Bodenstein especially deserves tremendous thanks. He helped me in physics, English, my daily and social life in the US etc. Part of my Ph.D. has been made by him. I also want to thank my office mate, Subashini de Silva, who contributed to extending my understanding in RF cavities. Many discussions with her were of great help to me.

Contents

List of Figures

List of Tables

Chapter 1

Introduction

1.1 Thomas Jefferson National Accelerator Facility

Thomas Jefferson National Accelerator Facility, commonly called Jefferson Lab or JLab, is a U.S. national laboratory located in Newport News, Virginia. Its primary mission is to conduct basic research on the structure of atomic nuclei using an electron accelerator, known as the Continuous Electron Beam Accelerator Facility (CEBAF). CEBAF consists of a polarized electron source and injector, two superconducting radio frequency (SRF) linear accelerators (linacs), and nine arc sections which connect the linacs. A schematic of the CEBAF machine and the user end stations is depicted in Figure 1.1. As the electron beam orbits up to five passes through each linac, its energy is increased up to a maximum of 6 GeV [1].

The beam is directed to three end stations, named Hall A, Hall B, and Hall C, for nuclear physics experiments. In each hall, the electron beam collides with a stationary target. This allows physicists to study the structure of atomic nuclei, particularly the distributions and interaction of quarks and gluons. Jefferson Lab

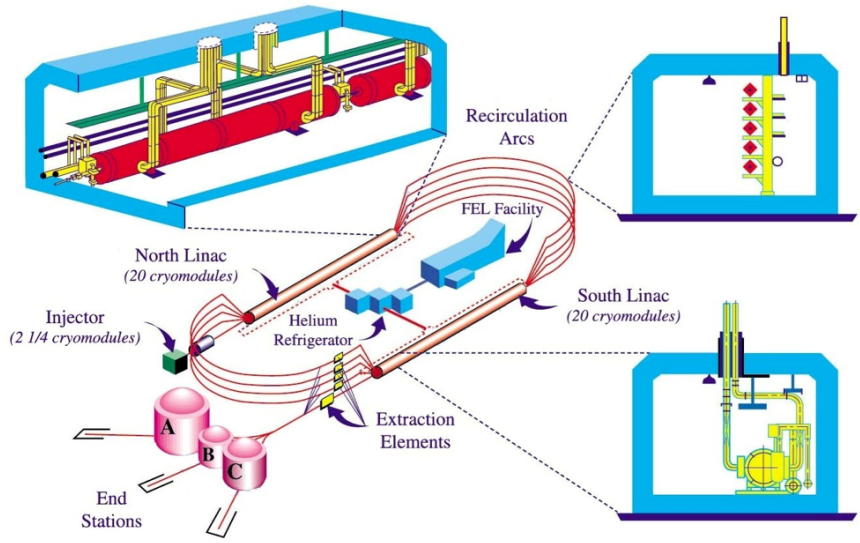

Fig. 1.1: Schematic of the CEBAF accelerator.

also conducts a variety of research using its Free Electron Laser (FEL), which is based on the same SRF technology used in CEBAF. (Picture from [1]).

1.2 CEBAF Overview

The CEBAF accelerator is a five-pass recirculating linac based on SRF technology. It is capable of simultaneous delivery of continuous wave (cw) electron beams of up to 6 GeV to the three end stations. The most important innovations in CEBAF are the choice of SRF technology and the use of multipass beam recirculation. Neither of these had been previously applied on such a large scale [1]. The cw electron beam is also a distinguishing feature which is enabled by employing the SRF technology. The recirculating linac configuration saves space and cost by using the accelerating cavities multiple times during multipass.

(a) 5-cell cavity used for 4 GeV CEBAF. **(b)** 7-cell cavity for the 12 GeV Upgrade.

Fig. 1.2: 5-cell cavity and 7-cell cavity.

CEBAF is in a racetrack configuration, comprised of two antiparallel linacs, called the North and South linacs, and arcs for recirculation. Each linac contains 20 cryomodules, and one cryomodule contains eight 5-cell cavities made of Niobium (see Figure 1.2a). At the exit of each linac, dipole magnets separate the beam vertically into different arcs according to energy. At the end of the arc, another set of dipoles are used to merge the individual beams into the next linac. Extra spaces were allocated at the end of each linac for future purposes. The 12 GeV Upgrade utilizes those spaces for new cryomodules containing 7-cell cavities (see Figure 1.2b).

180° recirculation arcs connect the two linacs. Because of the difference in energy, each recirculation pass needs an independent beam transport system. The arcs themselves consist of a total of nine transport lines (five in the east arc and four in the west arc) making a total of five passes possible [1].

1.3 The 12 GeV Upgrade

To expand the research opportunity in the nuclear physics, Jefferson Lab is upgrading its facility by doubling the beam energy from 6 to 12 GeV, constructing a new experimental hall, and upgrading its existing experimental halls. The increase in energy is achieved by adding five new cryomodules at the end of each linac as in Figure 1.3. New cryomodules to be used for the 12 GeV Upgrade use higher gradient 7-cell cavities (Figure 1.2b) while maintaining the overall length of the original cryomodule design, which uses 5-cell cavities (Figure 1.2a). The 12 GeV beam current may be varied from a few pico amperes up to 80 μA.

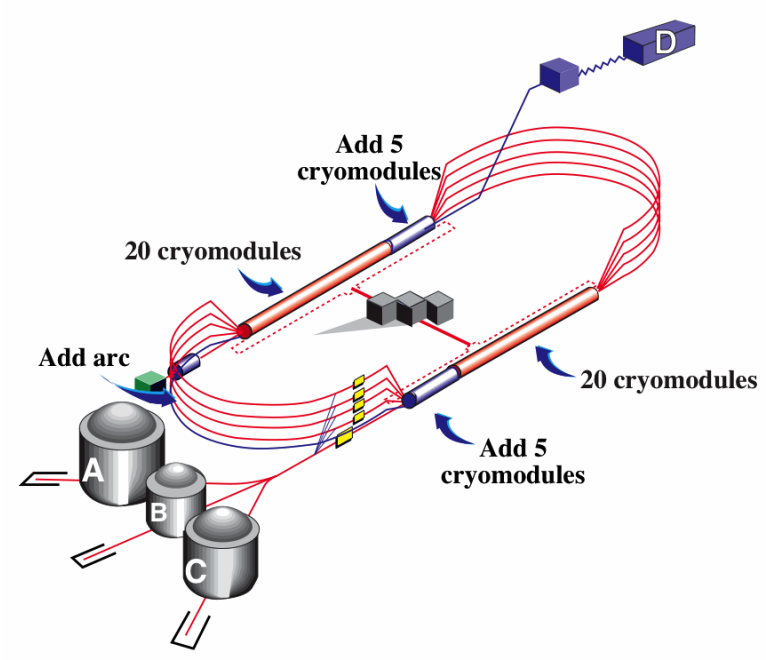

Fig. 1.3: Schematic of the 12 GeV Upgrade.

In addition to upgrading the energy, a new experimental hall, Hall D, will be

constructed and use a 12 GeV electron beam to carry out experiments mainly on gluons to test the current understanding of quark confinement. All three existing halls will be upgraded to take advantage of the new 5-pass 11 GeV beams.

1.4 Beam Breakup Instability

A radio frequency (RF) cavity is a device that establishes RF resonating electromagnetic fields in a confined region. An external RF source can excite resonant modes in the cavity. In addition, a charged particle traversing a cavity can also excite resonant modes in the cavity. The beam-excited modes alter incoming particle motion and can make the particle beam unstable [2]. This instability can limit the maximum available beam current in recirculating linacs such as CEBAF.

1.4.1 Mulitpass Beam Breakup

Recirculating linear accelerators provide a compact and efficient way of accelerating particle beams to medium and high energies by reusing the same linac for multiple passes. Recently there have been many projects around the world employing recirculating linacs such as CEBAF and FEL at Jefferson Lab, LHeC at CERN, ERL at BNL, ERL at Cornell, ALICE at Daresbury Lab, BERLinPro at HZB, cERL at KEK, MARS at BINP, and others [3,4]. In recirculating linacs, the maximum current can be limited by multipass beam breakup (BBU), which occurs when the electron beam interacts with the dipole higher order modes (HOMs) of

accelerating cavities during multipass recirculations.

In recirculating linacs, a particle deflected by an HOM on the first pass comes back to the same cavity again on the second or higher passes. A distinguishing feature is that the recirculating particle can constructively or destructively interfere with the HOM which deflected it on the previous pass. Therefore, there exists a feedback to the HOM field by the recirculating particle. The enhancing feedback by a series of particles can cause an exponential increase in the HOM field if the HOM is not sufficiently damped. The mode excitation can grow high enough so that the beam strikes a wall and is lost. This phenomenon is referred to as multipass BBU instability, and it provides the primary current limitation in the operation of superconducting recirculating linacs [3, 5, 6]. Recirculating linacs are generally more sensitive to the transverse BBU than the longitudinal BBU for the current limitation.

In 2007, CEBAF, having installed earlier prototype high-gradient cavities for the 12 GeV Upgrade, experienced multipass BBU at the beam current of 54 μA [7]. Great effort was made to improve HOM damping and performance with DESY-type coaxial HOM couplers and careful control of fabrication methods [8]. These new cavities in Figure 1.2 (b) will be used for the 12 GeV Upgrade. A performance test with beam is needed to demonstrate that the new cavities for the 12 GeV Upgrade are not vulnerable to multipass BBU. Experimental as well as simulation studies for the BBU instability at Jefferson Lab will be presented in

this thesis.

1.4.2 Cumulative BBU

Linear accelerators are usually made up of many accelerating cavities arranged in a line, along with various drift spaces and focussing elements between the cavities. Assume that an HOM is excited in a cavity. Particles are deflected by the HOM in the cavity, and they drift to the next cavity with a displacement due to the deflection. These displaced particles can excite a stronger HOM. Then, following particles arriving at the cavity can be more severely deflected due to the enhanced HOM. In this cumulative manner, the HOM in the earlier cavities can produce a larger beam displacement in the later cavities [9, 10].

Cumulative BBU effects can be categorized by two parts: transient behavior and steady state behavior. A simulation study for the transient behavior in the injector of the 12 GeV Upgrade was conducted [11], and will be described in this thesis.

Chapter 2

Theory of Multipass Beam Breakup Instability

2.1 RF Cavity

An RF cavity is a resonator, consisting of a closed metal structure that confines oscillating electromagnetic fields in the RF region of the spectrum. The electromagnetic fields can accelerate or decelerate beams of charged particles, and they can also change the direction of charged particles. The linacs of CEBAF consist of SRF cavities which are elliptical in shape and operate with a fundamental frequency of 1497 MHz.

2.2 Pillbox Cavity and Its Resonant Modes

Real accelerating cavities are more complicated than a simple pillbox shape. However, because a simple pillbox cavity is analytically solvable, it provides physical insights about resonant electromagnetic fields and the characteristics of the cavity. The pillbox cavity analysis also provides the natural basis for field expansions of resonant electromagnetic fields in cavities. The analytical expressions of

electromagnetic fields in a pillbox cavity will be derived in this section.

2.2.1 Resonant Modes of a Pillbox Cavity

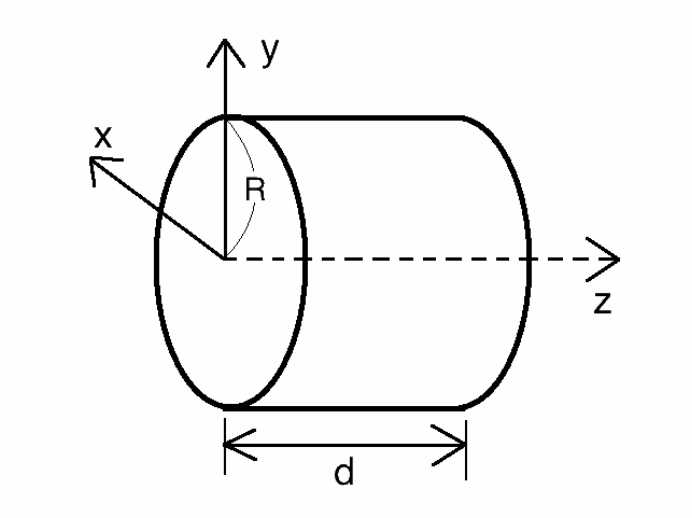

Fig. 2.1: Schematic of a pillbox cavity.

Consider a cylindrical cavity with a uniform nondissipative medium having permittivity ϵ and permeability μ. In a source free region, where charge density $\rho = 0$ and current density $\vec{J} = 0$, the Maxwell equations in SI units take the forms

$$\begin{aligned} \nabla \cdot \vec{E} = 0, \quad \nabla \times \vec{E} = -\tfrac{\partial \vec{B}}{\partial t} \\ \nabla \cdot \vec{B} = 0, \quad \nabla \times \vec{B} = \mu\epsilon \tfrac{\partial \vec{E}}{\partial t}. \end{aligned} \tag{2.1}$$

Maxwell equations combine to yield the wave equation

$$\left(\nabla^2 - \mu\epsilon \frac{\partial^2}{\partial t^2}\right) \left\{ \begin{array}{c} \vec{E} \\ \\ \vec{B} \end{array} \right\} = 0. \tag{2.2}$$

Assuming a sinusoidal time dependence, $e^{-i\omega t}$, and standing waves in the z direction as

$$\vec{E}(\rho,\phi,z,t) = \vec{E}(\rho,\phi)e^{\pm ikz-\omega t} \tag{2.3}$$

$$\vec{B}(\rho,\phi,z,t) = \vec{B}(\rho,\phi)e^{\pm ikz-\omega t}, \tag{2.4}$$

the wave equations become two independent Helmholtz equations,

$$\left[\ \nabla_t^2 + (\mu\epsilon\omega^2 - k^2)\ \right] \left\{ \begin{array}{c} \vec{E} \\ \\ \vec{B} \end{array} \right\} = 0, \tag{2.5}$$

where

$$\nabla_t^2 = \nabla^2 - \frac{\partial^2}{\partial z^2}. \tag{2.6}$$

The $\vec{E}$ and $\vec{B}$ fields can be determined by solving the eigenvalue equation subject to boundary conditions for a perfect conductor as

$$\hat{n} \times \vec{E} = 0 \quad \text{and} \quad \hat{n} \cdot \vec{B} = 0, \tag{2.7}$$

where $\hat{n}$ is a unit normal at the surface.

The Maxwell Equations 2.1 can be combined to express the transverse fields, $E_\perp$ and $B_\perp$, as a function of the longitudinal components, E_z and B_z. Moreover, the boundary condition at the cavity surface can be written as

$$E_z|_s = 0 \quad \text{and} \quad \left.\frac{\partial B_z}{\partial n}\right|_s = 0, \tag{2.8}$$

where s stands for values at the surface. Since the boundary conditions on E_z and B_z are different, Equations 2.5 in general have different eigenvalues. Because E_z

and B_z are independent, they form two families of solutions which are classified as transverse magnetic (TM) and transverse electric (TE) modes [12] . These modes are denoted as TM_{mnp} or TE_{mnp}, where m, n, and p are integers and describe the azimuthal, radial, and longitudinal periodicity, respectively. The general expressions for the field components are as follows [10]:

- TM_{mnp} modes

$$\begin{aligned}
E_z &= E_0 J_m\left(\tfrac{u_{mn}}{R}\rho\right)\cos(m\phi)\cos\left(\tfrac{p\pi z}{d}\right)e^{-i\omega_{mnp}t} \\
E_\rho &= -\tfrac{p\pi}{d}\tfrac{R}{u_{mn}}E_0 J'_m\left(\tfrac{u_{mn}}{R}\rho\right)\cos(m\phi)\sin\left(\tfrac{p\pi z}{d}\right)e^{-i\omega_{mnp}t} \\
E_\phi &= -\tfrac{p\pi}{d}\tfrac{mR^2}{u_{mn}^2\rho}E_0 J_m\left(\tfrac{u_{mn}}{R}\rho\right)\sin(m\phi)\sin\left(\tfrac{p\pi z}{d}\right)e^{-i\omega_{mnp}t} \\
H_z &= 0 \\
H_\rho &= i\tfrac{m\omega_{mnp}R^2}{u_{mn}^2\rho}\mu E_0 J_m\left(\tfrac{u_{mn}}{R}\rho\right)\sin(m\phi)\cos\left(\tfrac{p\pi z}{d}\right)e^{-i\omega_{mnp}t} \\
H_\phi &= i\tfrac{\omega_{mnp}R}{u_{mn}}\mu E_0 J'_m\left(\tfrac{u_{mn}}{R}\rho\right)\cos(m\phi)\cos\left(\tfrac{p\pi z}{d}\right)e^{-i\omega_{mnp}t}
\end{aligned} \tag{2.9}$$

- TE_{mnp} modes

$$\begin{aligned}
H_z &= H_0 J_m\left(\tfrac{u'_{mn}}{R}\rho\right)\cos(m\phi)\sin\left(\tfrac{p\pi z}{d}\right)e^{-i\omega_{mnp}t} \\
H_\rho &= \tfrac{p\pi}{d}\tfrac{R}{u'_{mn}}H_0 J'_m\left(\tfrac{u'_{mn}}{R}\rho\right)\cos(m\phi)\cos\left(\tfrac{p\pi z}{d}\right)e^{-i\omega_{mnp}t} \\
H_\phi &= -\tfrac{p\pi}{d}\tfrac{mR^2}{u'^2_{mn}\rho}H_0 J_m\left(\tfrac{u'_{mn}}{R}\rho\right)\sin(m\phi)\cos\left(\tfrac{p\pi z}{d}\right)e^{-i\omega_{mnp}t} \\
E_z &= 0 \\
E_\rho &= -i\tfrac{m\omega_{mnp}R^2}{u'^2_{mn}\rho}H_0 J_m\left(\tfrac{u'_{mn}}{R}\rho\right)\sin(m\phi)\sin\left(\tfrac{p\pi z}{d}\right)e^{-i\omega_{mnp}t} \\
E_\phi &= -i\tfrac{\omega_{mnp}R}{u'_{mn}}H_0 J'_m\left(\tfrac{u'_{mn}}{R}\rho\right)\cos(m\phi)\sin\left(\tfrac{p\pi z}{d}\right)e^{-i\omega_{mnp}t}.
\end{aligned} \tag{2.10}$$

Here $J_m(u)$ is the Bessel function, and u_{mn} is the n^{th} root of $J_m(u) = 0$ (see Figure 2.2a) . $J'_m(u)$ is the derivative of the Bessel function with respect to u, and u'_{mn}

is the n^{th} root of $J'_m(u) = 0$ (see Figure 2.2b). A few values of these roots are tabulated in Table 2.1 [10].

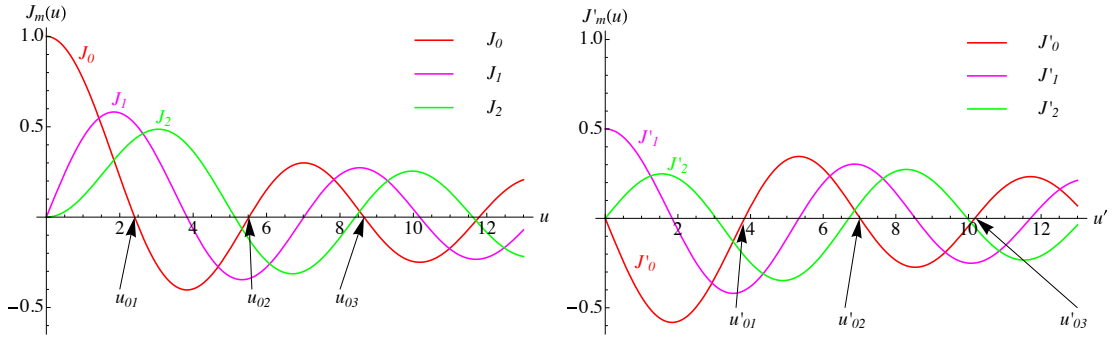

(a) Bessel function of the first kind, $J_m(u)$, for integer orders $m = 0, 1, 2$.

(b) Derivative of the Bessel function of the first kind, $J'_m(u)$, for integer orders $m = 0, 1, 2$.

Fig. 2.2: Bessel functions and their derivatives for integer orders $m = 0, 1, 2$.

m	u_{m1}	u_{m2}	u_{m3}
0	2.405	5.520	8.654
1	3.832	7.016	10.173
2	5.136	8.417	11.620

(a) Roots of $J_m(u) = 0$.

m	u'_{m1}	u'_{m2}	u'_{m3}
0	3.832	7.016	10.174
1	1.841	5.331	8.536
2	3.054	6.706	9.970

(b) Roots of $J'_m(u) = 0$.

Table 2.1: Zeros of $J_m(u)$ and $J'_m(u)$.

The resonant frequencies of TM or TE modes are given by [12]

$$\omega_{mnp} = \frac{1}{\sqrt{\mu\epsilon}}\sqrt{\left(\frac{u_{mn}}{R}\right)^2 + \left(\frac{p\pi}{d}\right)^2} \qquad \text{(TM modes)} \tag{2.11}$$

$$\omega_{mnp} = \frac{1}{\sqrt{\mu\epsilon}}\sqrt{\left(\frac{u'_{mn}}{R}\right)^2 + \left(\frac{p\pi}{d}\right)^2}, \qquad \text{(TE modes)} \tag{2.12}$$

where R is the radius of the cylinder, and d is the length of the cavity.

2.2.2 Accelerating Mode and Higher Order Modes

To accelerate particles, the longitudinal component of the electric field, E_z, must not be zero on the z axis. Only the Bessel function of J_0 does not vanish on the z axis; in Equation 2.9, $J_0(0) \neq 0$, and then $E_z \neq 0$. The TM_{010} mode is usually chosen for acceleration. It is also called a monopole mode because of its field distribution.

Modes of the type TM_{1np} and TE_{1np} have net deflecting fields on the z axis. These are referred to as dipole modes, and they are undesirable in accelerating cavities because they deflect the beam. Modes with m=2 are called quadrupole modes. Any electromagnetic mode that is not the fundamental accelerating mode is generally called a parasitic or higher order mode (HOM). Figure 2.3 shows a pillbox cavity with a TM_{110} mode which has an on-axis magnetic field and an electric field that varies linearly with distance off-axis near the beam axis. A charged particle passing through the cavity can be deflected by the magnetic field and excite the mode through the longitudinal electric field if it passes off-axis.

The dipole modes in actual CEBAF cavities have the same TM_{110}-like structure near the axis.

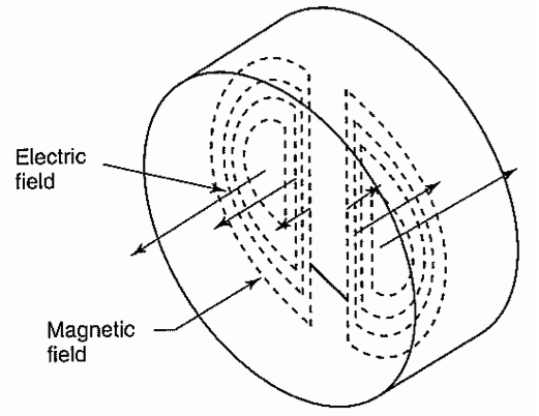

Fig. 2.3: Schematic of a TM_{110} mode.

Although electromagnetic fields in an multi-cell elliptical cavity are not exactly same as fields in the pillbox cavity, the pillbox nomenclature is usually used for mode identification. The mode polarization and phase advance per cell are also used for mode identification. A 7-cell cavity can be modeled by seven coupled harmonic oscillators. The phase advance is ideally a multiple of $\pi/7$ for a 7-cell standing wave pattern, and seven modes with different phase advances exist for a resonant mode [13].

2.3 Figures of Merit

Several figures of merit characterizing RF cavities are briefly described for the future description of the bream breakup instability.

1. Accelerating voltage and accelerating field:

   The accelerating voltage is defined as

   $$V_{acc} = \left| \frac{1}{q} \times \text{maximum energy gain possible during transit of the cavity} \right|,$$

   where q is the charge of a particle. The acceleration voltage is directly given by integrating the electric field along the beam. The accelerating field is defined by the accelerating voltage divided by a reference length. It is usually expressed in units of accelerating voltage per meter.

2. Quality factor, Q_0:

   The Q_0 value of a cavity is a measure of the sharpness of response to an external excitation. It is defined as the ratio of the energy stored in the cavity to the energy dissipated on cavity walls per radian:

   $$\begin{aligned} Q_0 &= \frac{\text{Energy stored in cavity}}{\text{Energy dissipated during one radian}} \\ &= \omega \frac{U}{P_{wall}}, \end{aligned} \tag{2.13}$$

   where ω is a resonant frequency, U is an energy stored in the cavity, and P_{wall} is a power dissipation by the ohmic heating of cavity walls.

3. Loaded quality factor, Q_L:

   For a cavity whose RF power source is turned off, the stored energy evolves as

   $$\frac{dU}{dt} = -P_{tot}, \tag{2.14}$$

where P_{tot} is the total power dissipated due to cavity couplers in addition to cavity walls. Analogous to Q_0, the loaded Q_L is defined as

$$Q_L = \omega \frac{U}{P_{tot}}. \tag{2.15}$$

The loaded quality factor takes into account the total power loss due to leaks in the cavity couplers in addition to the ohmic heating of cavity walls. The Q_L indicates how many oscillations it will take for the mode to dissipate its stored energy. The stored energy satisfies the equation:

$$U(t) = U_0 e^{-\frac{\omega}{Q_L}t}, \tag{2.16}$$

where U_0 is the stored energy at t = 0.

4. Shunt impedance, R_{sh}:

   The shunt impedance is a quantity used to characterize losses in a cavity and is defined as

   $$R_{sh} = \frac{V_{acc}^2}{P_{wall}}. \tag{2.17}$$

   It measures the efficiency of the accelerating voltage for a given dissipation. Ideally one wants the shunt impedance to be large for the accelerating mode so that the dissipated power is minimized.

   As a brief aside, note that in circuit theory one uses

   $$R_{sh} = \frac{V_{acc}^2}{2P_{wall}},$$

and a definition for linacs is

$$R_{sh} = \frac{V_{acc}^2}{P'_{wall}},$$

where P'_{wall} is the power dissipated per unit length. The linac shunt impedance is in ohms per meter [14].

5. Impedance, R/Q:

Taking the ratio of Equation 2.17 and Equation 2.13 results in another useful figure of merit,

$$\begin{aligned} \frac{R}{Q} &\equiv \frac{R_{sh}}{Q_0} \\ &= \frac{V_{acc}^2}{\omega U}. \end{aligned} \tag{2.18}$$

The R/Q is independent of the surface resistance and the cavity size but depends solely on the geometry of the cavity. It is a measure of the efficiency of the accelerating voltage for a given stored energy.

Dipole modes deflect a beam in the transverse direction. Analogous to Equation 2.18, the R/Q of dipole mode can be written as

$$\frac{R}{Q} = \frac{V_{\perp}^2}{\omega U}, \tag{2.19}$$

where $V_{\perp}$ is the effective deflecting voltage experienced by a charged particle while passing through the cavity. The R/Q of a mode indicates the extent of HOM excitation by charges passing through the cavity. In that sense, it

measures the strength of the coupling between the mode and beam. One of the goals of cavity design is to maximize the impedance R/Q for the accelerating mode to minimize the power dissipation while minimizing the impedance R/Q of higher order modes.

2.3.1 HOM Nomenclature and HOM Coupler

An HOM coupler is a waveguide which absorbs HOM energy, thereby lowering $V_\perp$ and the loaded quality factor of HOMs. If not sufficiently damped, the HOM may cause beam instabilities such as multipass beam breakup.

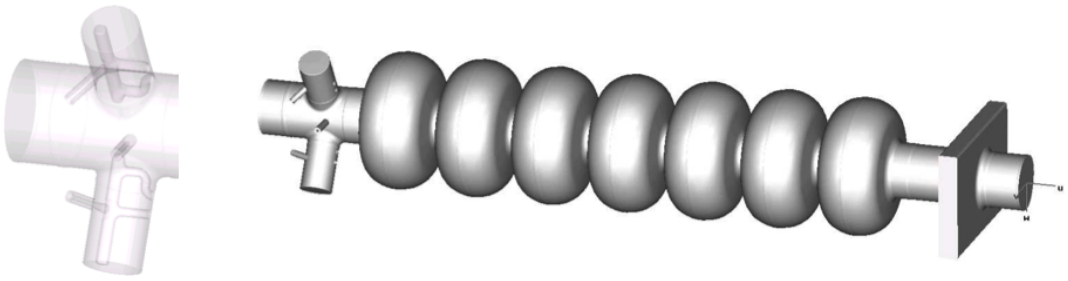

Fig. 2.4: 7-cell cavity model for the 12 GeV Upgrade (right). The transparent view of the HOM couplers (left). They are oriented 120 degrees with respect to each other. (Picture from [13]).

2.3.2 Transfer Matrix

At any specified position in a system, a charged particle is presented by a vector (single column matrix), and the transfer matrix $\boldsymbol{M}$ maps a particle vector

from a starting point to a new point:

$$\begin{pmatrix} x \\ \theta_x \\ y \\ \theta_y \\ z \\ \delta \end{pmatrix} = \boldsymbol{M} \begin{pmatrix} x_0 \\ \theta_{x,0} \\ y_0 \\ \theta_{y,0} \\ z_0 \\ \delta_0 \end{pmatrix}, \tag{2.20}$$

where the definitions of the particle vector elements are:

x : the horizontal displacement of the particle from the nominal trajectory

θ_x : the angle of the particle in the horizontal plane from the nominal trajectory

y : the vertical displacement of the particle from the nominal trajectory

θ_y : the angle of the particle in the vertical plane from the nominal trajectory

z : the path length difference in the longitudinal direction between the particle and the nominal trajectory

$\delta \equiv \Delta p/p$: the fractional momentum deviation of the particle from the nominal momentum.

The transfer matrix element, M_{ij}, will be referred through out this thesis.

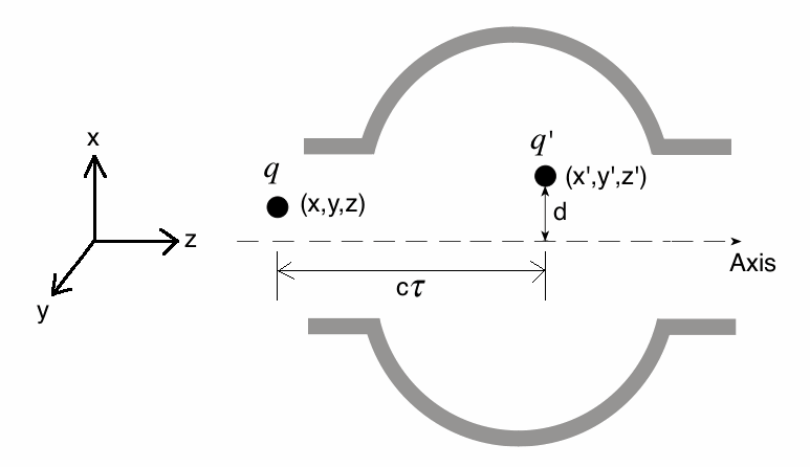

Fig. 2.5: Schematic of a test and source charge in a cavity. The test charge, q, follows the source charge, q'. Particles travel from left to right.

2.4 BBU Theory

2.4.1 Wakefield and Wake Function

The following discussion will focus on the transverse wakefield and its description in terms of the transverse HOMs in cavities. Figure 2.5 shows the configuration of this analysis where beam motion in the x plane will be considered. A source charge, q', at $\vec{r'} = (x', y', z')$ creates a wakefield in a cavity, and a test charge, q, at $\vec{r} = (x, y, z)$ follows at a distance $c\tau$ behind the source. Here c is the speed of light, and τ is the time delay of the test charge, q, relative to the source charge, q' in the lab frame. The test charge experiences the Lorentz force from the wakefield of the source charge. The transverse momentum kick and the

wakefield are related as

$$\begin{aligned}\frac{dp_x}{dt} &= c\frac{dp_x}{dz} \\ &= q\left(E_x(\vec{r},\frac{z}{c}+\tau;d)-cB_y(\vec{r},\frac{z}{c}+\tau;d)\right). \end{aligned} \tag{2.21}$$

Here the charges are assumed to be ultrarelativistic. The transverse momentum change is

$$\begin{aligned}\Delta p_x &= \frac{q}{c}\int\left(E_x(\vec{r},\frac{z}{c}+\tau;d)-cB_y(\vec{r},\frac{z}{c}+\tau;d)\right)\,dz \\ &\equiv \frac{q}{c}V, \end{aligned} \tag{2.22}$$

where the integration is performed over the cavity structure, and an effective deflecting voltage, V, is defined as

$$V(\tau,d)\equiv\int\left(E_x(\vec{r},\frac{z}{c}+\tau;d)-cB_y(\vec{r},\frac{z}{c}+\tau;d)\right)\,dz. \tag{2.23}$$

The transverse wake function is defined as the integrated wakefields seen by the test particle, q, traveling behind the source particle, divided by the source charge, q', and its off-axis displacement, d [15, 16]:

$$W(\tau) \equiv \frac{1}{q'd}\int\left(E_z(\vec{r},\frac{z}{c}+\tau;d)-cB_y(\vec{r},\frac{z}{c}+\tau;d)\right)\,dz \tag{2.24}$$

$$= \frac{1}{q'd}V(\tau,d). \tag{2.25}$$

The wake function describes the total transverse momentum change, Δp_x, imparted to the test particle, q, due to the wakefield of the source particle, q', at time, τ, after the HOM was excited.

For one source particle, q', the deflecting voltage and the wake function are simply related by

$$V(\tau) \;=\; W(\tau)q'd. \tag{2.26}$$

Consider the excitation of an HOM in a cavity by a beam current, $I(t')$, passing at transverse position, $d(t')$, off axis. A charge passing the cavity at time, t, experiences a deflecting voltage of

$$V(t) = \int_{-\infty}^{t} W(t-t')d(t')I(t')dt'. \tag{2.27}$$

It is useful to express the wake function in terms of HOM parameters by using the definition given by Equation 2.25. The wake function is in the form of a damped harmonic oscillation [6, 16]:

$$W_\lambda(\tau) = \frac{(R/Q)_\lambda k_\lambda \omega_\lambda}{2} e^{-\frac{\omega_\lambda}{2Q_\lambda}\tau} \sin(\omega_\lambda \tau), \tag{2.28}$$

where ω_λ and k_λ are the frequency and wave number of the HOM denoted by the subscript λ. The impedance $(R/Q)_\lambda$ is a purely geometric property of the cavity. This quantity describes the strength of the excitation of HOMs due to the passage of a charge. The quantity Q_λ is the loaded quality factor for the HOM which determines the time it takes for the HOM excitation to decay after the passage of a particle. In a superconducting cavity, the peaks tend to be fairly narrow and isolated so that the complete wake function that describes all the HOMs in the cavity is approximated as a summation over all the HOMs in the

cavity [17]:

$$W(\tau) = \sum_{\lambda} W_{\lambda}(\tau). \tag{2.29}$$

Using the concepts of wakefield and wake function, a theoretical description for multipass beam breakup will be discussed in the next section.

2.5 Derivation of the BBU Threshold Current

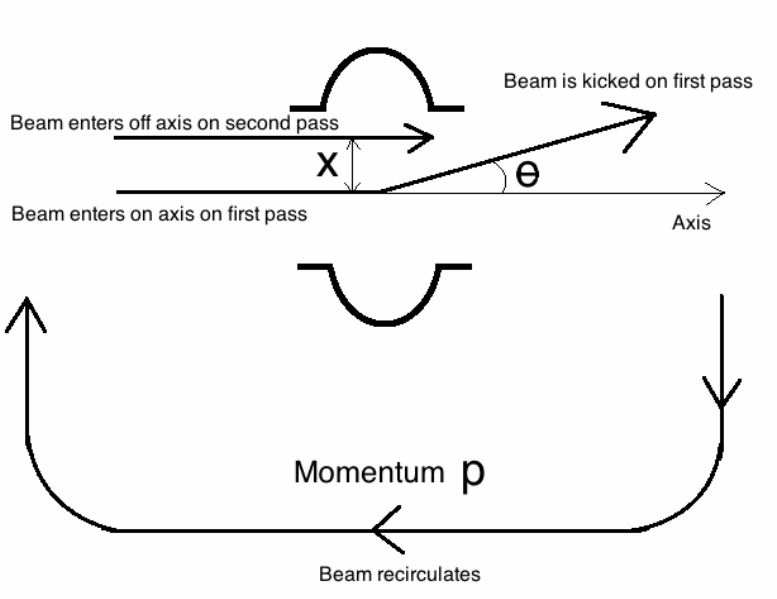

Fig. 2.6: Schematic of a single cavity with 2-pass beam. The beam enters on axis from the left and experiences a transverse kick, $\theta = \Delta p_x/p$, by an HOM. Then the beam recirculates along the return path with momentum p and enters the cavity again with a transverse displacement x off axis.

Figure 2.6 describes a simple model for BBU, which has one cavity with an HOM for 2-pass beam. Assume that an HOM exists in the cavity and a particle

is injected on the central axis. The particle does not excite the HOM on its first pass through the cavity, but the HOM exerts a transverse kick, which deflects the particle. On the second crossing of the cavity, the deflected particle has a transverse offset $x(t')$ at crossing time t'. If the returned particle increases the HOM energy, transverse kicks experienced by subsequent particles will be larger, which will in turn lead to a further growth of the HOM energy.

A particle passing the cavity at time t receives a transverse kick, $\theta = \Delta p_x/p$, by a deflecting voltage from Equation 2.27 given by

$$V(t) = \int_{-\infty}^{t} W(t-t')\, x(t')\, I(t')\, dt'. \tag{2.30}$$

The transverse offset, x', on the second pass can be written in terms of the angular deflection of the beam at the exit of the cavity on the first pass as

$$x(t') = M_{12}\ \theta(t' - T_r), \tag{2.31}$$

where T_r is the recirculation time to travel from a point in the cavity on the first pass to the same point on the second pass. M_{12} is the transfer matrix elements in Equation 2.20, and $\theta(t' - T_r)$ is the angular deflection of the beam at the exit of the cavity on the first pass given by

$$\theta(t' - T_r) = \frac{p_x(t' - T_r)}{p}. \tag{2.32}$$

Recalling Equation 2.22, $p_x(t' - T_r)$ can be expressed by a deflecting voltage as

$$p_x(t' - T_r) = \frac{e}{c}\ V(t' - T_r), \tag{2.33}$$

where e is the electron charge. Combining Equations 2.32 and 2.33 with Equation 2.31 yields

$$x(t') = M_{12}\ \frac{e}{pc}\ V(t' - T_r). \tag{2.34}$$

Substituting Equation 2.34 into Equation 2.30 results in an integral equation for the deflecting voltage:

$$V(t) = \frac{eM_{12}}{pc} \int_{-\infty}^{t} W(t - t')I(t' - T_r)V(t' - T_r)\ dt'. \tag{2.35}$$

Assuming that the current is a continuous stream of short pulses being injected at multiples of a time interval, t_b, between particles, the current on the second pass is given by

$$I(t') = I_0\ t_b \sum_{n=-\infty}^{\infty} \delta(t' - nt_b), \tag{2.36}$$

where I_0 is the average beam current.

The solution for the wake potential is assumed to be of the form

$$V(t) = V_0 e^{-i\Omega t}. \tag{2.37}$$

Inserting Equations 2.28, 2.36, and 2.37 into Equation 2.35 yields

$$V_0\, e^{-i\Omega t} = \mathcal{K}\ V_0 \sum_{n=-\infty}^{\infty} \int_{-\infty}^{t} e^{-\frac{\omega_\lambda (t-t')}{2Q_\lambda}} \sin\left(\omega_\lambda (t - t')\right)\ \delta(t' - T_r - nt_b)\ e^{-i\Omega(t'-T_r)}\, dt', \tag{2.38}$$

where

$$\mathcal{K} \equiv \frac{eI_0 t_b (R/Q)_\lambda k_\lambda \omega_\lambda M_{12}}{2pc}. \tag{2.39}$$

Integrating over the delta function yields

$$e^{-i\Omega t} = \frac{\mathcal{K}}{2i}\, e^{-\frac{\omega_\lambda (t-T_r)}{2Q_\lambda}} \sum_{n=-\infty}^{n_p} \left(e^{i\omega_\lambda (t-T_r)} e^{n\left\{\frac{\omega_\lambda}{2Q_\lambda} - i(\Omega+\omega_\lambda)\right\} t_b} - e^{-i\omega_\lambda (t-T_r)} e^{n\left\{\frac{\omega_\lambda}{2Q_\lambda} - i(\Omega-\omega_\lambda)\right\} t_b} \right), \tag{2.40}$$

where the upper limit of the summation, n_p, is the number of particles that have passed through the cavity on the second pass at time t, given by

$$n_p = \frac{t - T_r}{t_b}. \tag{2.41}$$

The sum in Equation 2.40 takes the form of a geometric series

$$\sum_{n=-\infty}^{n_p} e^{nz_\pm} = \frac{e^{(n_p+1)z_\pm}}{e^{z_\pm} - 1}, \tag{2.42}$$

where

$$z_\pm = \left\{ \frac{\omega_\lambda}{2Q_\lambda} - i(\Omega \pm \omega_\lambda) \right\} t_b. \tag{2.43}$$

Substitution of Equation 2.42 into Equation 2.40 and simplification of the results yield an equation for the complex frequency Ω,

$$e^{-i\Omega T_r} = \left(\frac{e I_0 t_b (R/Q)_\lambda k_\lambda \omega_\lambda M_{12}}{2pc} \right) \frac{\left(e^{\frac{\omega_\lambda t_b}{2Q_\lambda}}\, e^{-i\Omega t_b} \right) \sin(\omega_\lambda t_b)}{1 - 2\left(e^{\frac{\omega_\lambda t_b}{2Q_\lambda}}\, e^{-i\Omega t_b} \right) \cos(\omega_\lambda t_b) + \left(e^{\frac{\omega_\lambda t_b}{2Q_\lambda}}\, e^{-i\Omega t_b} \right)^2}. \tag{2.44}$$

For given HOM parameters, the threshold current can be found numerically from Equation 2.44 by scanning the real value of Ω [18]. In general the current, I_0, turned out to be complex except for a few isolated real frequency values and the smallest positive, I_0, among them is the threshold current for the BBU.

A perturbative solution to Equation 2.44 can be obtained by introducing an expansion parameter

$$\varepsilon \ = \frac{eI_0 t_b (R/Q)_\lambda k_\lambda \omega_\lambda M_{12}}{2pc}. \tag{2.45}$$

Assuming ε is small, the complex frequency is approximated to first order in ε by

$$\Omega = A_0 + A_1 \varepsilon, \tag{2.46}$$

where A_0 and A_1 are parameters to be determined. Inserting Equations 2.45 and 2.46 into Equation 2.44 and expanding terms in ε, as well as keeping terms only to first order, we find

$$A_0 \ = \ \pm\omega_\lambda - i\frac{\omega_\lambda}{2Q_\lambda} \tag{2.47}$$

$$A_1 \ = \ \mp\frac{1}{2t_b}\, e^{iA_0 T_r}, \tag{2.48}$$

and

$$\Omega = \pm\omega_\lambda - i\frac{\omega_\lambda}{2Q_\lambda} \mp \frac{1}{2t_b} e^{i\left(\pm\omega_\lambda - i\frac{\omega_\lambda}{2Q_\lambda}\right)T_r}\varepsilon. \tag{2.49}$$

The imaginary part of Ω is

$$\mathrm{Im}(\Omega) = -\frac{\omega_\lambda}{2Q_\lambda} - \frac{1}{2t_b}\sin(\omega_\lambda T_r) e^{\frac{\omega_\lambda}{2Q_\lambda}T_r}\,\varepsilon, \tag{2.50}$$

where Im denotes the imaginary part of complex number. The threshold current, I_{th}, is found from the condition, $\mathrm{Im}(\Omega) = 0$ at $I_0 = I_{th}$. Applying this condition, the formula for the BBU threshold current to first order is [6, 18, 19]

$$I_{th} = -\frac{2\ pc/e}{(R/Q)_\lambda Q_\lambda k_\lambda\ M_{12}\ \sin(\omega T_r)\ e^{\frac{\omega_\lambda}{2Q_\lambda}T_r}}. \tag{2.51}$$

It is notable that the first order formula provides an infinitely large threshold current value when $\sin(\omega_\lambda T_r)$ is close to zero. In such a case, the first order formula provides an inadequately large threshold current value, and an expansion in ε to second order is needed. Performing calculations for the expansion of

$$\Omega = A_0 + A_1\varepsilon + A_2\varepsilon^2 \tag{2.52}$$

yields

$$A_2 = \pm\frac{1}{4t_b}\left(\frac{\cot(\omega_\lambda t_b)}{2} \mp i\frac{T_r + 2t_b}{t_b}\right)e^{2iA_0T_r}, \tag{2.53}$$

with A_0 and A_1 defined in Equation 2.47 and 2.48.

Consequently, the second order formula is given by [18]

$$I_{th} = \frac{2\,(pc/e)\left(\sin(\omega_\lambda T_r) \pm \sqrt{\sin^2(\omega_\lambda T_r) + (\frac{2\omega_\lambda}{Q_\lambda})\Delta}\right)}{\left(\frac{R}{Q}\right)k_\lambda\omega_\lambda M_{12}\,e^{\frac{\omega_\lambda T_r}{2Q_\lambda}}\,\Delta}, \tag{2.54}$$

where

$$\Delta = \frac{t_b}{2}\left\{(1-\sin(\omega_\lambda t_b))\cos(2\omega_\lambda T_r) - \sin(\omega_\lambda(2T_r+t_b))\right\} + T_r\cos^2(\omega_\lambda T_r). \tag{2.55}$$

Note that the first order formula can be obtained from the second order formula when $\sin^2(\omega_\lambda T_r) \gg 2\omega_\lambda\Delta/Q_\lambda$, which clearly shows the validity of Equation 2.54. Figure 2.7 compares first and second order solutions for the threshold currents. The second order solution describes when $\sin(\omega_\lambda T_r)$ is close to zero, but it still does not cover the full frequency range. A numerical calculation is needed for the frequency range where the analytical formulae fail to give a physically meaningful solution.

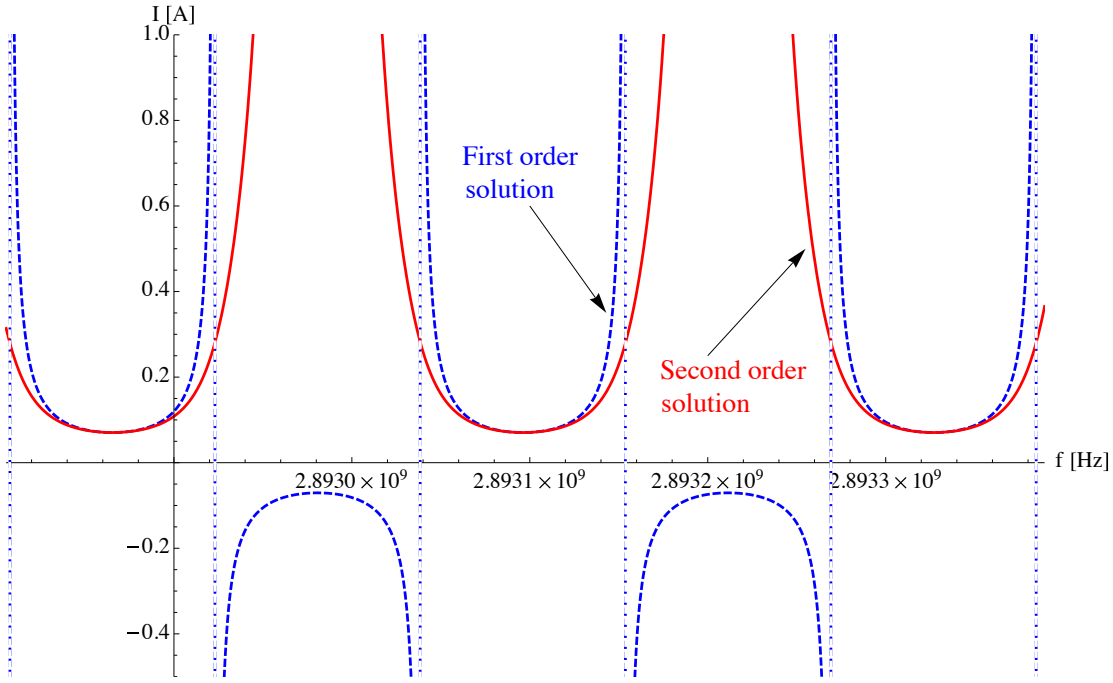

Fig. 2.7: First and second order solutions for BBU threshold current. The graph describes the threshold current behavior around 2893 MHz as an example. The blue (dashed) line represents first order solution (Equation 2.51), and the red (solid) line second order solution (Equation 2.54).

2.6 Longitudinal BBU

In the optics for the 12 GeV Upgrade accelerator, the higher pass arcs are particularly intended to operate with non-zero isochronicity, which means that the time of flight is not equal for all particles. Because of this choice, it is possible that multipass BBU in longitudinal HOMs could cause instability. A simple model of longitudinal BBU instability which can be solved analytically is described in this section [20]. An analytical calculation for the 12 GeV Upgrade accelerator is

performed at the end of this section, which concludes that the longitudinal BBU is not a concern for the 12 GeV Upgrade.

Consider a series of particles passing through a simplest multipass configuration: two pass recirculation linac containing a single cavity with one HOM. Suppose there is an initial excitation of a longitudinal HOM. Let a series of equally spaced particles enter the cavity on the first pass. On exiting the cavity, the longitudinal HOM modulates the energy of the particles. If the recirculation optics is not isochronous, the transit time of particles depends on the energy modulation. The variation in the transit time appears as a spacing modulation.

On the second crossing of the cavity, the modulated current can enhance the excitation of the HOM which created the energy modulation on the previous pass. A feedback loop is formed which is analogous to that which generates transverse beam breakup. The threshold condition for instability is met when an excitation produces, through the induced current, a self-enhancement which matches the original cavity excitation. A significant difference of the longitudinal BBU from the transverse one is the saturation behavior of an HOM excitation [20].

2.6.1 Longitudinal Wakefield

A test charge follows the exciting charge, q', with a time delay, τ, through a region of the accelerator. The longitudinal wake function for the region, $W_l(\tau)$, is defined to be the energy gain of the unit test charge from the electromagnetic

field induced by the exciting charge in a region, divided by the exciting charge. An expression for the longitudinal wake function is

$$W_l(\tau) \equiv \frac{1}{q'} \int_{region} E_z(\vec{r}, \frac{z}{c} + \tau)\, dz, \tag{2.56}$$

where $E_z(z,t)$ is the longitudinal electric field induced by the exciting particle, which is assumed to cross $z = 0$ at $t = 0$.

Similar to the transverse wake function as Equation 2.28, the longitudinal wake function can be expressed in terms of HOM parameters [6, 16],

$$W_l(\tau) = \frac{(R/Q)_\lambda \omega_\lambda}{2} e^{-\frac{\omega_\lambda}{2Q_\lambda}\tau} \cos(\omega_\lambda \tau), \tag{2.57}$$

where ω_λ is the HOM frequency, and the subscript, λ, serves as an index for an HOM.

2.6.2 Longitudinal Impedance

The wake potential at time t is given by

$$V(t) = \int_{-\infty}^{+\infty} W_l(t - t') I(t')\, dt, \tag{2.58}$$

where

$$W_l(t - t') = 0, \quad \text{for } t - t' < 0, \tag{2.59}$$

and $I(t')$ is the current at time t'.

The Fourier transforms of $V(t)$, $I(t)$, and $W(t)$ can be defined as

$$\tilde{V}(\omega) = \int_{-\infty}^{+\infty} V(t)e^{i\omega t}\, dt \tag{2.60}$$

$$\tilde{I}(\omega) = \int_{-\infty}^{+\infty} I(t)e^{i\omega t}\, dt \tag{2.61}$$

$$\tilde{Z}(\omega) = \int_{-\infty}^{+\infty} W(t)e^{i\omega t}\, dt. \tag{2.62}$$

Applying the convolution theorem to Equation 2.58, the longitudinal wake potential in the frequency domain can be expressed as

$$\tilde{V}(\omega) = \tilde{Z}(\omega)\tilde{I}(\omega). \tag{2.63}$$

The impedance, $\tilde{Z}(\omega)$, is independent of the current and only depends on cavity characteristics. The impedance can be calculated by sending a single particle through the cavity and then using this impedance to compute wake potentials for other currents.

Consider a charge, q, passing through a cavity at time, $t = 0$. The currents are

$$I(t) = q\ \delta(t) \tag{2.64}$$

$$\tilde{I}(\omega) = q\int_{-\infty}^{+\infty} \delta(t)e^{i\omega t}\, dt \tag{2.65}$$

$$= q. \tag{2.66}$$

From Equation 2.57, the HOM voltage, $V(t)$, induced by the traversal of this charge through a cavity is

$$V(t) = \frac{q\omega_\lambda (R/Q)_\lambda}{2} e^{-\frac{\omega_\lambda}{2Q_\lambda}t} \cos(\omega_\lambda t), \quad t > 0. \tag{2.67}$$

The Fourier transform of $V(t)$ is

$$\tilde{V}(\omega) = -\frac{q\omega_\lambda (R/Q)_\lambda}{4}\left(\frac{1}{i\omega + i\omega_\lambda - \frac{\omega_\lambda}{2Q_\lambda}} + \frac{1}{i\omega - i\omega_\lambda - \frac{\omega_\lambda}{2Q_\lambda}}\right). \tag{2.68}$$

The longitudinal impedance, $\tilde{Z}(\omega)$, is given by

$$\begin{aligned} \tilde{Z}(\omega) &\equiv \frac{\tilde{V}(\omega)}{\tilde{I}(\omega)} && (2.69)\\ &= -\frac{\omega_\lambda (R/Q)_\lambda}{4}\left(\frac{1}{i\omega + i\omega_\lambda - \frac{\omega_\lambda}{2Q_\lambda}} + \frac{1}{i\omega - i\omega_\lambda - \frac{\omega_\lambda}{2Q_\lambda}}\right). && (2.70) \end{aligned}$$

Applying Equation 2.57 to Equation 2.62 and directly integrating give the same impedance as Equation 2.70.

2.6.3 Current Spectrum of a Modulated Current

Consider a sequence of particles injected into a two-pass recirculating linac with a single cavity. The particles of charge q are equally spaced with a time interval of t_b. At a reference point, the current is of the form:

$$I(t) = q\sum_{m=-\infty}^{\infty}\delta(t - mt_b). \tag{2.71}$$

Note that the current is a periodic function with a period, $t_b = \frac{2\pi}{\omega_b}$. The Fourier decomposition coefficient, I_n, is

$$\begin{aligned} I_n &= \frac{1}{t_b}\int_{-\frac{t_b}{2}}^{\frac{t_b}{2}} I(t)\, e^{-in\omega_b t}dt \\ &= \frac{1}{t_b}\int_{-\frac{t_b}{2}}^{\frac{t_b}{2}} q\sum_{m=-\infty}^{\infty}\delta(t - mt_b)e^{-in\omega_b t} \\ &= \frac{q}{t_b}. \end{aligned} \tag{2.72}$$

The Fourier decomposition of the current can be expressed as

$$I(t) = \frac{q}{t_b} \sum_{n=-\infty}^{\infty} e^{in\omega_b t}, \tag{2.73}$$

and the result implies that a uniform sequence of point charges produces a signal at all harmonics of the bunching frequency.

Assume that an HOM exists in the cavity at a frequency $\nu\omega_b$, where ν is real, and $\omega_b = \frac{2\pi}{t_b}$ is a bunching frequency. On the first crossing of the particles through the cavity, their energy will be modulated at the HOM frequency as $\sin(\nu\omega_b t + \phi)$, where ϕ is an arbitrary phase of the perturbation. If the isochronicity of the recirculation optics is not zero, the recirculation time depends on the particle energy during the recirculation. The energy modulation will be translated into the modulation of the arrival time of particles. The modulation of the arrival time of particle k for the second crossing through the cavity is of the form:

$$t_m = mt_b + \Delta t \sin(\nu\omega_b m t_b + \phi) + T_r, \tag{2.74}$$

where T_r is the recirculation time of the particle, and Δt is the small amplitude of the perturbation. This modulation generates the current

$$I(t) = q \sum_{m=-\infty}^{\infty} \delta(t - mt_b - \Delta t \sin(\nu\omega_b m t_b + \phi) - T_r). \tag{2.75}$$

The Fourier transform of the current is

$$\begin{aligned}
\tilde{I}(\omega) &= \int_{-\infty}^{\infty} I(t) e^{i\omega t} dt \\
&= q \sum_{m=-\infty}^{\infty} \int_{-\infty}^{\infty} \delta(t - mt_b - \Delta t \sin(\nu\omega_b m t_b + \phi) - T_r)\ e^{i\omega t}\ dt \\
&= q \sum_{m=-\infty}^{\infty} e^{i\omega T_r}\ e^{i\omega m t_b}\ e^{i\omega \Delta t \sin(2\pi\nu m + \phi)}. \qquad (2.76)
\end{aligned}$$

Applying the identities:

$$e^{ix\sin y} = \sum_{\mu=-\infty}^{\infty} J_\mu(x)\ e^{i\mu y} \qquad (2.77)$$

$$\sum_{m=-\infty}^{\infty} e^{imt_b\omega} = \omega_b \sum_{n=-\infty}^{\infty} \delta(\omega - n\omega_b), \qquad (2.78)$$

the current becomes

$$\begin{aligned}
\tilde{I}(\omega) &= q \sum_{m=-\infty}^{\infty} \sum_{\mu=-\infty}^{\infty} e^{i\omega T_r}\ e^{i\omega m t_b}\ J_\mu(\omega\Delta t)\ e^{i\mu(2\pi\nu m + \phi)} \\
&= q \sum_{m=-\infty}^{\infty} \sum_{\mu=-\infty}^{\infty} e^{i(\omega T_r + \mu\phi)}\ J_\mu(\omega\Delta t)\ e^{imt_b(\omega + \mu\nu\omega_b)} \\
&= q\omega_0 \sum_{n=-\infty}^{\infty} \sum_{\mu=-\infty}^{\infty} e^{i(\omega T_r + \mu\phi)}\ J_\mu(\omega\Delta t)\ \delta(\omega + \mu\nu\omega_b - n\omega_b). \qquad (2.79)
\end{aligned}$$

The modulated current by the HOM has been calculated so far in this section. In the next section, the HOM voltage induced by this modulated current will be discussed.

2.6.4 Voltage Induced by a Modulated Current

On the second crossing through the cavity, the modulated current in Equation 2.79 interacts with the cavity through the impedance in Equation 2.70. It

will induce a voltage in the frequency domain given by

$$\begin{aligned}
\tilde{V}(\omega) &= \tilde{Z}(\omega)\tilde{I}(\omega) \\
&= -\frac{\omega_\lambda (R/Q)_\lambda}{4}\left(\frac{1}{i\omega + i\omega_\lambda - \frac{\omega_\lambda}{2Q_\lambda}} + \frac{1}{i\omega - i\omega_\lambda - \frac{\omega_\lambda}{2Q_\lambda}}\right) \times \\
&\quad q\omega_0 \sum_{n=-\infty}^{\infty}\sum_{\mu=-\infty}^{\infty} e^{i(\omega T_r + \mu\phi)}\; J_\mu(\omega\Delta t)\; \delta(\omega - (n-\mu\nu)\omega_b) \qquad (2.80)
\end{aligned}$$

The Fourier conjugate voltage, $V(t)$, is

$$\begin{aligned}
V(t) &= \frac{1}{2\pi}\int_{-\infty}^{+\infty} \tilde{V}(\omega) e^{-i\omega t}\, d\omega \\
&= -\frac{1}{2\pi}\int_{-\infty}^{+\infty} \frac{\omega_\lambda (R/Q)_\lambda}{4}\left(\frac{1}{i\omega + i\omega_\lambda - \frac{\omega_\lambda}{2Q_\lambda}} + \frac{1}{i\omega - i\omega_\lambda - \frac{\omega_\lambda}{2Q_\lambda}}\right) \times \\
&\quad q\omega_0 \sum_{n=-\infty}^{\infty}\sum_{\mu=-\infty}^{\infty} e^{i\{\omega(T_r - t) + \mu\phi\}}\; J_\mu(\omega\Delta t)\; \delta(\omega - (n-\mu\nu)\omega_b)\; d\omega \\
&= -\frac{I_0 \omega_\lambda (R/Q)_\lambda}{4} \sum_{n=-\infty}^{\infty}\sum_{\mu=-\infty}^{\infty} e^{i\{(n-\mu\nu)\omega_b(T_r - t) + \mu\phi\}} J_\mu((n-\mu\nu)\omega_b\Delta t) \times \\
&\quad \left\{\frac{1}{i\omega_b(n-\mu\nu) + i\omega_\lambda - \frac{\omega_\lambda}{2Q_\lambda}} + \frac{1}{i\omega_b(n-\mu\nu) - i\omega_\lambda - \frac{\omega_\lambda}{2Q_\lambda}}\right\}, \qquad (2.81)
\end{aligned}$$

where $I_0 \equiv \frac{q\omega}{2\pi}$ is an average beam current.

In the limit of a small coherent modulation of the bunching frequency, the argument of $J_\mu((n-\mu\nu)\omega_b\Delta t)$ is small. Thus, the lower order terms of $J_\mu((n-\mu\nu)\omega_b\Delta t)$ contribute significantly. A few low order terms of the Bessel function are

$$J_0(x) = 1 - \frac{x^2}{4} + \frac{x^4}{64} - \cdots \qquad (2.82)$$

$$J_{\pm 1}(x) = \pm\frac{x}{2} \mp \frac{x^3}{16} \pm \frac{x^5}{384} \mp \cdots \qquad (2.83)$$

$$J_{\pm 2}(x) = \frac{x^2}{8} - \frac{x^4}{96} + \frac{x^6}{3072} - \cdots . \qquad (2.84)$$

The J_0 and $J_{\pm 1}$ contain a constant and linear terms, and they dominate the expansion of $J_\mu((n-\mu\nu)\omega_b\Delta t)$. The lowest order term of the J_0 expansion in Equation 2.82, which is a constant, is independent of the amplitude of the modulation and describes simple energy loss to the HOM. It will not contribute to a possible instability since it does not provide feedback with respect to the modulation amplitude. The first order term of $J_{\pm 1}$ in Equation 2.83 provides such a feedback mechanism. In the following calculations, only the first order term of $J_{\pm 1}$ is considered.

From Equation 2.81, the HOM voltage at a particle-crossing time, mt_b, is

$$V(mt_b) = -\frac{I_0\omega_\lambda(R/Q)_\lambda}{4}\sum_{n=-\infty}^{\infty}\sum_{\mu=-\infty}^{\infty} e^{i\{(n-\mu\nu)\omega_b(T_r-mt_b)+\mu\phi\}} J_\mu((n-\mu\nu)\omega_b\Delta t)\times \left\{\frac{1}{i\omega_b(n-\mu\nu)+i\omega_\lambda-\frac{\omega_\lambda}{2Q_\lambda}}+\frac{1}{i\omega_b(n-\mu\nu)-i\omega_\lambda-\frac{\omega_\lambda}{2Q_\lambda}}\right\}. \quad (2.85)$$

The main contribution is from the $J_{\pm 1}$ terms when $|(n-\mu\nu)\omega_b\Delta t| \ll 1$. Keeping the J_1 term yields

$$V_{J_1}(mt_b) = -\frac{I_0\omega_\lambda(R/Q)_\lambda}{4}\sum_{n=-\infty}^{\infty} e^{i\{(n-\nu)\omega_b(T_r-mt_b)+\phi\}} J_1((n-\nu)\omega_b\Delta t)\times \left\{\frac{1}{i(n-\nu)\omega_b+i\omega_\lambda-\frac{\omega_\lambda}{2Q_\lambda}}+\frac{1}{i(n-\nu)\omega_b-i\omega_\lambda-\frac{\omega_\lambda}{2Q_\lambda}}\right\}. \quad (2.86)$$

For a narrow resonance, one particular term such that $|n-\nu|\omega_b \approx \omega_\lambda$ will dominate the HOM voltage.

Similar to the J_1 case, keeping the J_{-1} term gives

$$V_{J_{-1}}(mt_b) = -\frac{I_0\omega_\lambda(R/Q)_\lambda}{4}\sum_{n=-\infty}^{\infty} e^{i\{(n+\nu)\omega_b(T_r-mt_b)-\phi\}}J_{-1}((n+\nu)\omega_b\Delta t)\times \left\{\frac{1}{i(n+\nu)\omega_b+i\omega_\lambda-\frac{\omega_\lambda}{2Q_\lambda}}+\frac{1}{i(n+\nu)\omega_b-i\omega_\lambda-\frac{\omega_\lambda}{2Q_\lambda}}\right\}. \quad (2.87)$$

Using the $\pm$ symmetry of the summation index, n, one can replace n with $-n$. Utilizing the relations, $J_{-1}(x) = -J_1(x)$ and $J_1(-x) = -J_1(x)$, the above equation is rewritten as

$$V_{J_{-1}}(mt_b) = -\frac{I_0\omega_\lambda(R/Q)_\lambda}{4}\sum_{n=-\infty}^{\infty} e^{-i\{(n-\nu)\omega_b(T_r-mt_b)+\phi\}}J_1((n-\nu)\omega_b\Delta t)\times \left\{\frac{1}{-i(n-\nu)\omega_b+i\omega_\lambda-\frac{\omega_\lambda}{2Q_\lambda}}+\frac{1}{-i(n-\nu)\omega_b-i\omega_\lambda-\frac{\omega_\lambda}{2Q_\lambda}}\right\} \quad (2.88)$$

One can define the tuning angles, ψ_n^+ and ψ_n^-, of the HOM by the relations:

$$\tan\psi_n^+ = \frac{\omega_\lambda+(n-\nu)\omega_b}{\frac{\omega_\lambda}{2Q_\lambda}} \quad (2.89)$$

$$\tan\psi_n^- = \frac{\omega_\lambda-(n-\nu)\omega_b}{\frac{\omega_\lambda}{2Q_\lambda}}. \quad (2.90)$$

The terms in the cursive bracket in Equations 2.86 and 2.88 can be reexpressed as

$$\frac{1}{i(n-\nu)\omega_b+i\omega_\lambda-\frac{\omega_\lambda}{2Q_\lambda}} = -\frac{2Q_\lambda}{\omega_\lambda}\frac{1}{1-i\tan\psi_n^+} = -\frac{2Q_\lambda}{\omega_\lambda}e^{i\psi_n^+}\cos\psi_n^+ \quad (2.91)$$

$$\frac{1}{-i(n-\nu)\omega_b-i\omega_\lambda-\frac{\omega_\lambda}{2Q_\lambda}} = -\frac{2Q_\lambda}{\omega_\lambda}\frac{1}{1+i\tan\psi_n^+} = -\frac{2Q_\lambda}{\omega_\lambda}e^{-i\psi_n^+}\cos\psi_n^+ \quad (2.92)$$

$$\begin{aligned}
\frac{1}{i(n-\nu)\omega_b - i\omega_\lambda - \frac{\omega_\lambda}{2Q_\lambda}} &= -\frac{2Q_\lambda}{\omega_\lambda}\frac{1}{1+i\tan\psi_n^-} \\
&= -\frac{2Q_\lambda}{\omega_\lambda}e^{-i\psi_n^-}\cos\psi_n^- \qquad (2.93) \\
\frac{1}{-i(n-\nu)\omega_b + i\omega_\lambda - \frac{\omega_\lambda}{2Q_\lambda}} &= -\frac{2Q_\lambda}{\omega_\lambda}\frac{1}{1-i\tan\psi_n^-} \\
&= -\frac{2Q_\lambda}{\omega_\lambda}e^{i\psi_n^-}\cos\psi_n^-. \qquad (2.94)
\end{aligned}$$

Rewriting $V_{J_1}(mt_b)$ and $V_{J_{-1}}(mt_b)$ using the tuning angles yields

$$\begin{aligned}
V_{J_1}(mt_b) &= -\frac{I_0\omega_\lambda(R/Q)_\lambda}{4}\sum_{n=-\infty}^{\infty} e^{i\{(n-\nu)\omega_b(T_r-mt_b)+\phi\}}J_1((n-\nu)\omega_b\Delta t)\times \\
&\quad \left\{-\frac{2Q_\lambda}{\omega_\lambda}e^{i\psi_n^+}\cos\psi_n^+ - \frac{2Q_\lambda}{\omega_\lambda}e^{-i\psi_n^-}\cos\psi_n^-\right\} \\
&= \frac{I_0(R/Q)_\lambda Q_\lambda}{2}\sum_{n=-\infty}^{\infty} e^{i\{(n-\nu)\omega_b(T_r-mt_b)+\phi+\psi_n^+\}}J_1((n-\nu)\omega_b\Delta t)\cos\psi_n^+ + \\
&\quad \frac{I_0(R/Q)_\lambda Q_\lambda}{2}\sum_{n=-\infty}^{\infty} e^{i\{(n-\nu)\omega_b(T_r-mt_b)+\phi-\psi_n^-\}}J_1((n-\nu)\omega_b\Delta t)\cos\psi_n^-.
\end{aligned} \qquad (2.95)$$

$$\begin{aligned}
V_{J_{-1}}(mt_b) &= -\frac{I_0\omega_\lambda(R/Q)_\lambda}{4}\sum_{n=-\infty}^{\infty} e^{-i\{(n-\nu)\omega_b(T_r-mt_b)+\phi\}}J_1((n-\nu)\omega_b\Delta t)\times \\
&\quad \left\{-\frac{2Q_\lambda}{\omega_\lambda}e^{i\psi_n^-}\cos\psi_n^- - \frac{2Q_\lambda}{\omega_\lambda}e^{-i\psi_n^+}\cos\psi_n^+\right\} \\
&= \frac{I_0(R/Q)_\lambda Q_\lambda}{2}\sum_{n=-\infty}^{\infty} e^{-i\{(n-\nu)\omega_b(T_r-mt_b)+\phi-\psi_n^-\}}J_1((n-\nu)\omega_b\Delta t)\cos\psi_n^- + \\
&\quad \frac{I_0(R/Q)_\lambda Q_\lambda}{2}\sum_{n=-\infty}^{\infty} e^{-i\{(n-\nu)\omega_b(T_r-mt_b)+\phi+\psi_n^+\}}J_1((n-\nu)\omega_b\Delta t)\cos\psi_n^+.
\end{aligned} \qquad (2.96)$$

The total HOM voltage is

$$\begin{aligned} V(mt_b) &= V_{J_1}(mt_b) + V_{J_{-1}}(mt_b) \\ &= I_0\left(\frac{R}{Q}\right)_\lambda Q_\lambda \sum_{n=-\infty}^{\infty} J_1((n-\nu)\omega_b\Delta t)\cos\psi_n^+ \times \\ &\qquad \cos\left[(n-\nu)\omega_b(T_r - mt_b) + \phi + \psi_n^+\right] + \\ &\quad I_0\left(\frac{R}{Q}\right)_\lambda Q_\lambda \sum_{n=-\infty}^{\infty} J_1((n-\nu)\omega_b\Delta t)\cos\psi_n^- \times \\ &\qquad \cos\left[(n-\nu)\omega_b(T_r - mt_b) + \phi - \psi_n^-\right]. \end{aligned} \tag{2.97}$$

For a narrow resonance, one particular term such that $|n-\nu|\omega_b \approx \omega_\lambda$ will dominate the HOM voltage.

If $(n-\nu)\omega_b \approx \omega_\lambda$, from Equation 2.89,

$$\tan\psi_n^+ \approx \frac{2\omega_\lambda}{\frac{\omega_\lambda}{2Q}} = 4Q_\lambda \gg 1, \tag{2.98}$$

which means

$$\cos\psi_n^+ \approx 0, \tag{2.99}$$

and from Equation 2.90,

$$\tan\psi_n^- = \frac{\frac{\omega_\lambda - (n-\nu)\omega_b}{\omega_\lambda}\omega_\lambda}{\frac{\omega_\lambda}{2Q_\lambda}} = 2\epsilon Q_\lambda \ll 1, \tag{2.100}$$

where $\epsilon \equiv \frac{(n-\nu)\omega_b - \omega_\lambda}{\omega_\lambda} = \frac{\Delta\omega_\lambda}{\omega_\lambda} \ll 1$, which infers

$$\cos\psi_n^- \approx 1. \tag{2.101}$$

If $(n-\nu)\omega_b \approx -\omega_\lambda$, in the same way as the case of $(n-\nu)\omega_b \approx \omega_\lambda$,

$$\cos\psi_n^+ \approx 1 \tag{2.102}$$

$$\cos\psi_n^- \approx 0. \tag{2.103}$$

Therefore, only one tuning angle term, $\cos\psi_n^+$ or $\cos\psi_n^-$, in Equation 2.97 dominates the HOM voltage for either case of $(n-\nu)\omega_b \approx \omega_\lambda$ or $(n-\nu)\omega_b \approx -\omega_\lambda$. To represent the two cases in one equation, redefine the tuning angle as $\psi_n \equiv +\psi_n^+$ or $\psi_n \equiv -\psi_n^-$. Using the approximation, $J_1(x) = \frac{x}{2}$, for small x and keeping the dominant term with a tuning angle ψ_n, the HOM voltage can be written as

$$V(mt_b) = \frac{1}{2} I_0 \left(\frac{R}{Q}\right)_\lambda Q_\lambda \ (n-\nu)\omega_b \Delta t \ \cos\psi_n \ \cos\left[(n-\nu)\omega_b(T_r - mt_b) + \phi + \psi_n\right] \tag{2.104}$$

Up to now, the HOM voltage induced by the modulated particles on the second pass is obtained. In the next section, threshold current will be obtained using this induced HOM voltage.

2.6.5 Analysis of Longitudinal Multipass BBU

The slip factor, η, which relates the recirculation time and particle energy, can be defined by the relation:

$$\Delta T = \eta T_r \frac{\Delta E}{E}, \tag{2.105}$$

where ΔT is the time offset due to the energy offset, ΔE. First-pass energy is denoted by E, and the recirculation time of on-energy particle is T_r. The HOM

voltage modulates particle energy as $\sin(\nu\omega_b t + \phi)$ on the first crossing through the cavity, where ϕ is an arbitrary phase of the perturbation. Through η, the energy modulation causes a modulation of the arrival time of particle m at the second crossing of the cavity in the form of

$$t_m = mt_b + \Delta t \sin(\nu\omega_b m t_b + \phi) + T_r. \tag{2.106}$$

Therefore, the initial perturbation is given by

$$\Delta T_{\text{perturb}} = \Delta t \sin(\nu\omega_b m t_b + \phi). \tag{2.107}$$

This perturbed current induces an HOM voltage according to Equation 2.104 at the second crossing of the cavity. The induced HOM voltage can modulate the recirculating time according to Equation 2.105:

$$\begin{aligned}
\Delta T_{\text{induced}} &= \eta T_r \frac{\Delta E}{E} && (2.108)\\
&= \eta T_r \frac{eV(mt_b)}{E} && (2.109)\\
&= \frac{\eta T_r}{E}\frac{e}{2} I_0 \left(\frac{R}{Q}\right)_\lambda Q_\lambda \ (n-\nu)\omega_b \Delta t \ \cos\psi_n \times \\
&\quad \cos\left[(n-\nu)\omega_b(T_r - mt_b) + \phi + \psi_n\right]. && (2.110)
\end{aligned}$$

The initial perturbation, $\Delta T_{\text{perturb}}$, generates $\Delta T_{\text{induced}}$. If $\Delta T_{\text{perturb}}$ generates the same amount of the time perturbation as $\Delta T_{\text{induced}}$, the HOM voltage can stay in steady state. The condition for the self-generating modulation is

$$\Delta T_{\text{perturb}} = \Delta T_{\text{induced}}. \tag{2.111}$$

The amplitude of the two time modulations satisfy the relation

$$\left| \frac{\eta T_r}{E} \frac{e}{2} I_0 \left(\frac{R}{Q} \right)_\lambda Q_\lambda \ (n-\nu)\omega_b \cos\psi_n \right| = 1. \tag{2.112}$$

Solving the equation for the beam current produces

$$I_0 = \frac{2E}{e\eta T_r (R/Q)_\lambda Q_\lambda \ |(n-\nu)\omega_b \ \cos\psi_n|}. \tag{2.113}$$

From recalling Equations 2.99, 2.101, 2.102, and 2.103, a worst case estimation of the threshold current can is obtained under the assumption that $|(n-\nu)\omega_b| = \omega_\lambda$ and $|\cos\psi_n| = 1$.

The sinusoidal functions in Equations 2.107 and 2.110 should also satisfy the relation for a coherent motion:

$$\sin(\nu\omega_b m t_b + \phi) = \pm\cos[(n-\nu)\omega_b(T_r - m t_b) + \phi + \psi_n], \tag{2.114}$$

where the $\pm$ sign depends on the sign of $(n-\nu)\omega_b \ \cos\psi_n$.

From Equation 2.113 under the worst case condition, the minimum threshold current is given by

$$I_{th} \ = \frac{2E}{e\eta T_r (R/Q)_\lambda Q_\lambda \omega_\lambda}. \tag{2.115}$$

The slip factor can be expressed in terms of the transfer matrix element, M_{56}:

$$\eta \equiv \frac{\frac{\Delta T}{T_r}}{\frac{\Delta E}{E}} \simeq \frac{M_{56}}{L}, \tag{2.116}$$

where L is the one-pass length, and M_{56} maps the momentum deviation, $\frac{\Delta p}{p}$, to the longitudinal displacement, $z = M_{56}\frac{\Delta p}{p}$ as defined in Equation 2.20. Substituting

this relation in Equation 2.115, the minimum threshold current is given by

$$I_{th} = \frac{2EL}{eT_r(R/Q)_\lambda Q_\lambda \omega_\lambda M_{56}}. \tag{2.117}$$

Using $\frac{L}{T_r} \approx c$, the threshold current can be rewritten in a similar form to the threshold current of the transverse BBU as Equation 2.51 :

$$I_{th} = \frac{2E}{e(R/Q)_\lambda \; Q_\lambda \; k_\lambda M_{56}} \tag{2.118}$$

To verify the analytic threshold formula, computer simulations have been performed earlier [20,21], and the results agree well with the theoretical prediction. As the beam current is varied, the HOM excitation (stored energy) exhibits clear threshold behavior as shown in Figure 2.8. Above the threshold, the level of excitation shows a saturation behavior which distinguishes the longitudinal beam breakup from the transverse one.

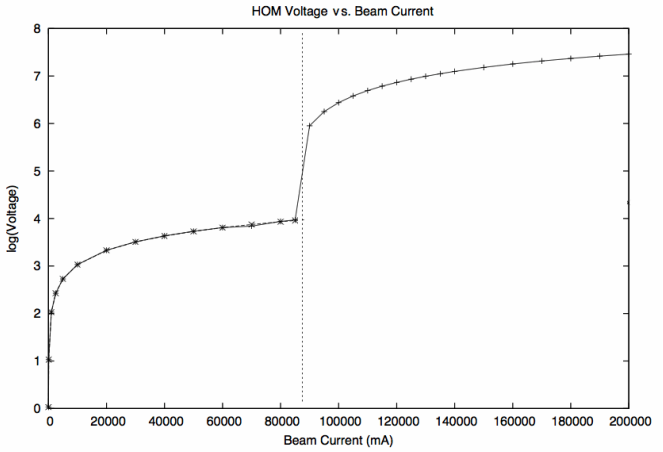

Fig. 2.8: Threshold behavior for longitudinal multipass beam breakup. (Picture from [21]).

Parameter	Value	Unit
E	600	MeV
ω_λ	$2\pi\times$ 1900	MHz
M_{56}	0.5	m
I_{th}	400	μA

Table 2.2: Parameters for the longitudinal HOM damping requirement calculation.

2.6.6 Damping Requirements for Longitudinal BBU

In the optics for the 12 GeV accelerator, it is intended that the arcs, particularly the higher arcs, are run in a mode where there is non-zero isochronicity. Because of this choice, it is possible that the longitudinal BBU instability could be problematic. This section presents numerical calculations for a longitudinal HOM damping requirement.

From Equation 2.118, the impedance requirement can be calculated as

$$\left(\frac{R}{Q}\right)_\lambda Q_\lambda \leq \frac{2E}{e\ k_\lambda M_{56} I_{th}}. \tag{2.119}$$

Using the parameters in Table 2.2, the impedance for a two pass beam should be

$$\left(\frac{R}{Q}\right)_\lambda Q_\lambda \leq 1.5 \times 10^{11}. \tag{2.120}$$

One can judge the significance of the longitudinal BBU by comparing the damping requirement for the longitudinal and transverse BBU. From Equation 2.51,

the damping requirement for the transverse BBU is

$$\left(\frac{R}{Q}\right)_{\lambda} Q_{\lambda} \leq -\frac{2\ pc/e}{k_{\lambda} M_{12} I_{th} \sin\left(\omega_{\lambda} T_r\right)}. \tag{2.121}$$

Substituting $M_{12} \approx 10$ m, $pc \approx 600$ MeV, $\sin\left(\omega_{\lambda} T_r\right) = -1$, and the parameters in Table 2.2 into Equation 2.121 yields

$$\left(\frac{R}{Q}\right)_{\lambda} Q_{\lambda} \leq 7.5 \times 10^{9}. \tag{2.122}$$

Even though the parameters for transverse BBU are very conservative, the longitudinal impedance damping requirement is much greater than the transverse one. Therefore, the longitudinal BBU is not a concern in the 12 GeV accelerator as long as the the longitudinal impedances have the same order of magnitude as the transverse impedances.

Chapter 3

Computer Simulations of Beam Breakup Instability

3.1 Simulation Codes

Even though the analytical expression in Equation 2.51 of the threshold current for a cavity containing a single HOM is helpful to study simple cases and understanding the parametric dependence of the threshold current, computer simulation codes are required to investigate BBU for beams with more than 2 passes and with many cavities containing many HOMs per cavity. Two FORTRAN simulation codes , *TDBBU* and *MATBBU*, were developed at Jefferson Lab [22–24], and they were used extensively for BBU studies.

3.1.1 *TDBBU*

TDBBU is based on a particle tracking algorithm. Particles propagate through beamline elements by iterations of one RF period. In one iteration, *TDBBU* moves a particle to the next beamline element and updates HOM excitation levels in all cavities based on the transverse position of the particles entering

the cavities. To pass a particle to the next element, *TDBBU* uses the transfer matrix method, which multiplies the coordinates of the entering particle by the linear transfer matrix of the element. The result is the injection coordinates of the particle in the next element [22]. The output of *TDBBU* is transverse coordinates at a beamline element, which is specified as an input parameter. The BBU threshold current can be determined by observing the transverse position behavior in time. At the onset of BBU instability, the transverse position increases exponentially when it observed at a certain point with respect to particle number or time, as shown in Figure 3.1.

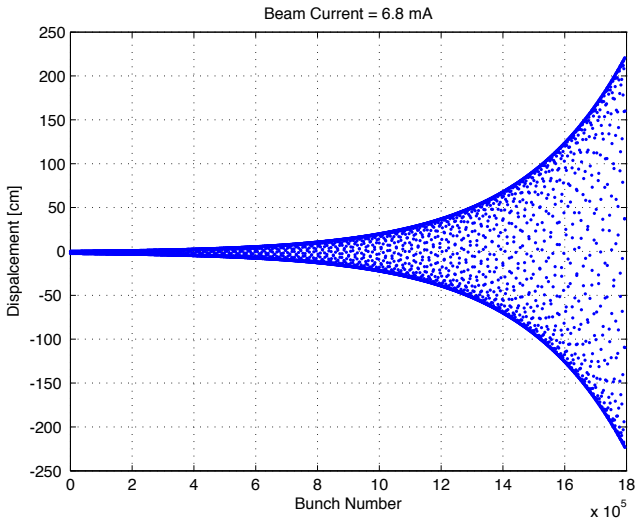

Fig. 3.1: Example of *TDBBU* output. The transverse beam position (y axis) is observed at the end of the CEBAF beamline with respect to the particle number (x axis). The transverse displacement increases exponentially, which means BBU instability is present.

3.1.2 *MATBBU*

MATBBU calculates the threshold current numerically using Equation 2.44. For a given positive current, I_0, the values of Ω in Equation 2.37 are in general complex. If Ω has a negative imaginary part, it produces an exponential decay component. Then, the voltage decreases exponentially, and the beam is stable. When Ω has a positive imaginary part, the beam is unstable because of an exponentially increasing component. If Ω is real, the voltage is a constant and the beam is in a steady state, which is a threshold condition [3].

Numerical solutions can be found by determining the current, I_0, while scanning real Ω. *MATBBU* sweeps the real value of Ω and computes I_0, which is complex in general. Figure 3.2 shows the output of *MATBBU* in a complex current plane. The intersection with the real axis which has the smallest positive value yields the threshold current [23, 24].

3.2 Implementation of the RF Focusing Effect in *TDBBU*

3.2.1 RF Cavity Model in TDBBU

The RF focusing effect is important in understanding beam dynamics in low energy transport such as electron guns and low energy portions of linacs. *TDBBU* did not have this RF focusing feature. It adopted the same accelerating cavity model as the model in a computer simulation program, *TRANSPORT* [25], which considers the adiabatic damping effect, but not the RF focusing effect. It treats an

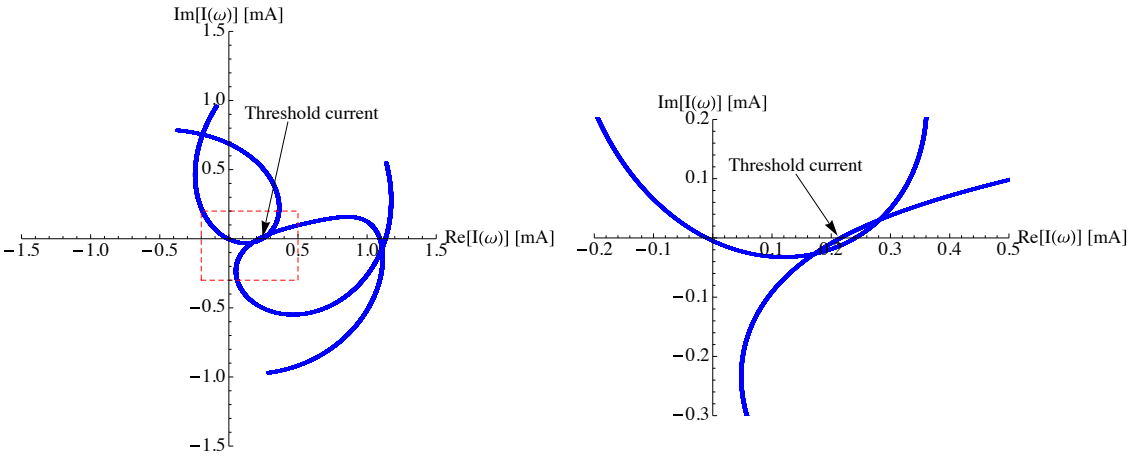

(a) Example of output from *MATBBU* for HOM damping requirement study.

(b) Zoomed in view of the dashed red rectangle in the left figure.

Fig. 3.2: Complex current output from *MATBBU* showing the results of scanning a real value of Ω in Equation 2.44. The lowest positive current intersecting the real current axis is the threshold current.

RF cavity as a simple accelerating section with constant energy gain throughout the RF cavity. For ultra-relativistic particles ($\beta c \cong c$), this transfer matrix is

$$\begin{pmatrix} x \\ \theta \end{pmatrix} = \begin{pmatrix} 1 & L\frac{\gamma_i}{\Delta\gamma\cos(\Delta\phi)}\ln\left(1+\frac{\Delta\gamma\cos(\Delta\phi)}{\gamma_i}\right) \\ 0 & \frac{\gamma_i}{\gamma_i+\Delta\gamma\cos(\Delta\phi)} \end{pmatrix} \begin{pmatrix} x_0 \\ \theta_0 \end{pmatrix}, \tag{3.1}$$

where L is the length of the cavity, γ_i is the Lorentz factor at the entrance of the cavity, $\Delta\gamma$ is the difference in Lorentz factors between the entrance and exit of the cavity, $\Delta\phi$ is the phase of the particle with respect to the maximum acceleration phase, x is the transverse position, and $\theta \equiv p_x/p$ is the particle angle [25].

An accelerator computer simulation program, *elegant* [26], calculated beam-

line optics for the BBU study. *elegant* can include the Rosenzweig-Serafini (R-S) model for the RF focusing as described in the next section. I implemented the R-S model in *TDBBU* to use the RF focusing algorithm in *TDBBU* and *elegant* for this thesis work.

3.2.2 Rosenzweig-Serafini Model

In a cylindrically symmetric and spatially periodic RF cavity, the accelerating RF electric field, E_z, induces fields in the radial and azimuthal directions. These induced fields generate a force in the radial direction, given by

$$F_r \cong -\frac{qr}{2}\frac{d}{dz}E_z, \tag{3.2}$$

where q is the charge of the particle, and r is the radial coordinate [27, 28]. The R-S model combines the focusing effects from this radial force and end-focusing effects due to the fringe fields at the entrance and exit of the cavity. These effects can be incorporated into a single transfer matrix for an RF cavity of arbitrary modes [29]. For a pure π mode cavity, this model simplifies to the Chambers model [30], and the transfer matrix is

$$\begin{pmatrix} \cos\alpha - \sqrt{2}\cos(\Delta\phi)\sin\alpha & \sqrt{8}\frac{\gamma_i}{\gamma'}\cos(\Delta\phi)\sin\alpha \\ -\frac{\gamma'}{\gamma_f}\left(\frac{\cos(\Delta\phi)}{\sqrt{2}} + \frac{1}{\sqrt{8}\cos(\Delta\phi)}\right)\sin\alpha & \frac{\gamma_i}{\gamma_f}\left(\cos\alpha + \sqrt{2}\cos(\Delta\phi)\sin\alpha\right) \end{pmatrix}, \tag{3.3}$$

where $\alpha \equiv \frac{1}{\sqrt{8}\cos(\Delta\phi)}\ln\left(\frac{\gamma_f}{\gamma_i}\right)$, γ_f is the Lorentz factor at the exit of the cavity. $\gamma' \equiv \frac{qE_0\cos(\Delta\phi)}{mc^2}$ is the normalized energy gradient averaged over the RF structure,

where E_0 is defined as the average accelerating field experienced by a particle injected at the phase which gives maximal acceleration [29].

I implemented the RF focusing feature in *TDBBU* using the R-S model. The RF focusing effect gives recognizable influence on the beam dynamics at the beginning of the first pass in CEBAF machine [31]. Incorporation of the RF focusing makes BBU simulations match more closely with experimental results.

The RF focusing effect was also applied to the simulation for the 12 GeV injector prototype design, where beam energy is very low. Section 3.4 will describe *TDBBU* simulation results when the RF focusing effect is present.

3.3 Simulations of Multipass BBU

3.3.1 Simulations for the 12 GeV CEBAF Upgrade

In this section, BBU simulation studies to determine the HOM damping requirement of the new 7-cell cavity will be described.

3.3.1.1 The 12 GeV Upgrade with Standard 4 GeV Arc Optics

Previously, a BBU simulation study was carried out to determine the damping requirements of the new 7-cell cavities for a CEBAF machine with an arc transport design similar to the 4 GeV standard arc optics [32]. Table 3.1 lists dipole mode characteristics of the new 7-cell cavity prototype which were used for simulations.

Assumptions and parameters for the simulations are as follows. The injection energy is 123 MeV. The cavity gradient is 7.5 MV/m for all 5-cell cavities in the 40 old cryomodules; the cavity gradient is 17.5 MV/m for all 7-cell cavities in the 10 additional new cryomudules. The HOMs in the 5-cell cavities are sufficiently damped not to cause BBU. The quadrupoles in the linacs are set to the 120° phase advance per period as the original 4 GeV accelerator. The total recirculation path lengths are 6310, 6310, 6301, and 6298 RF wavelengths for the 1st, 2nd, 3rd, and 4th passes, respectively. These approximations and assumptions should still be closely representative of a machine which is dominated by a single HOM in the cavities.

Figure 3.3 shows the threshold current distribution. The simulation study revealed the HOMs of new 7-cell cavity should be damped to Q_L values less than 7.51×10^6 for 1874 MHz and less than $Q_L = 6.2 \times 10^8/(\frac{R}{Q})$ for all other modes as listed in Table 3.1. The HOM damping requirements were obtained for a beam current of 300 μA, which is greater than the maximum designed beam current of 80 μA for the 12 GeV Upgrade.

An HOM damping requirement study for a 6 GeV operation at the 12 GeV Upgrade accelerator was also performed [32]. The results revealed that a 6 GeV operation up to 200 μA is stable if the HOMs meet the damping requirements for the 12 GeV operation in the Table 3.1.

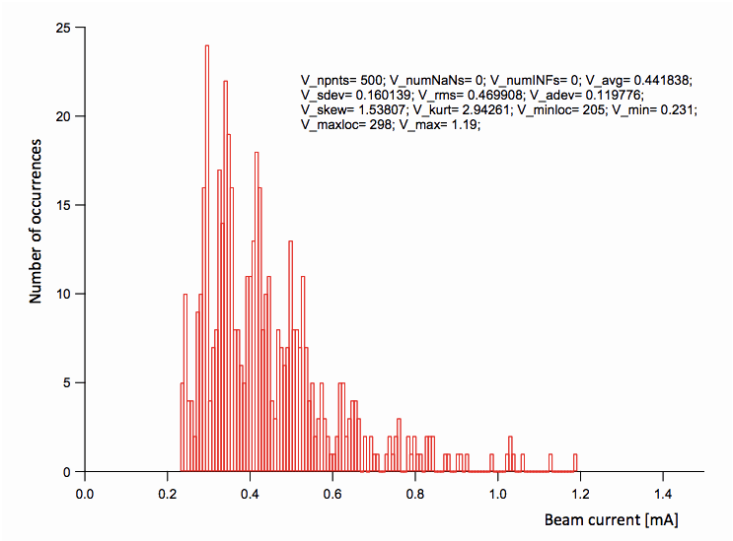

Fig. 3.3: BBU simulation result using the 4 GeV standard arc optics for the 1874 MHz dipole mode with $Q_L = 1 \times 10^7$. The 1874 MHz mode was excited in each cavity and the frequencies were randomly distributed with the full width of 1 MHz. By this method, 500 samples with different HOMs were made. The 500 samples provided adequate statistics for the given amount of computing time. Note that the minimum threshold current is 0.231 mA for $Q_L = 1 \times 10^7$. (Histogram from [32]).

3.3.1.2 The 12 GeV Upgrade with DBA Arc Optics

In the 12 GeV Upgrade using the 4 GeV standard arc optics, the emittance and energy spread increase significantly due to synchrotron radiation in the arcs. As an alternative proposal, a double bend achromat (DBA) arc optics for the 12 GeV Upgrade was developed by Alex Bogacz [33]. This section will compare the BBU threshold currents for the 12 GeV Upgrade using the DBA arc optics

f [MHz]	R/Q [Ω]	Q_L	f [MHz]	R/Q [Ω]	Q_L
1724.152	0.22	2.87×10^9	1746.066	0.06	1.03×10^{10}
1780.721	3.76	1.65×10^8	1825.357	1.91	3.25×10^8
1874.220	**82.55**	$\mathbf{7.51 \times 10^6}$	1928.851	62.03	1.00×10^7
1995.611	3.04	2.04×10^8	2004.930	16.27	3.81×10^7
2073.533	1.96	3.16×10^8	2094.526	29.29	2.12×10^7
2110.941	**27.53**	$\mathbf{2.25 \times 10^7}$	2115.194	1.30	4.76×10^8
2118.917	4.48	1.39×10^8	2119.273	0.53	1.18×10^9

Table 3.1: Dipole modes of 7-cell cavity prototype. The Q_L values are the maximum allowed values acquired by BBU simulation studies.

and the 4 GeV standard arc optics in order to confirm that the HOM damping requirement still valid for CEBAF using the DBA arc optics.

The same assumptions and approximations in the previous section have been applied to the simulations for the 12 GeV Upgrade with DBA arc optics. The two highest impedance modes, 1874 MHz in TE_{111} and 2111 MHz in TM_{110} modes (bold face in Table 3.1), are considered in this simulation. The 7-cell cavity cryomodules are located at the 21st through 25th slots in the North Linac and 21st through 25th slots in the South Linac. Only the 7-cell cavities are excited with an HOM in each threshold calculation while the other cavities give energy gains without the excitation of HOMs. The total recirculation path lengths are

6554, 6549, 6547, and 6546 RF wavelengths for the 1st, 2nd, 3rd, and 4th passes of the CEBAF accelerator, respectively.

The simulation results revealed that the lowest threshold current was 0.219 mA for 1874 MHz modes with $Q_L = 1 \times 10^7$, as shown in Figure 3.4. The threshold

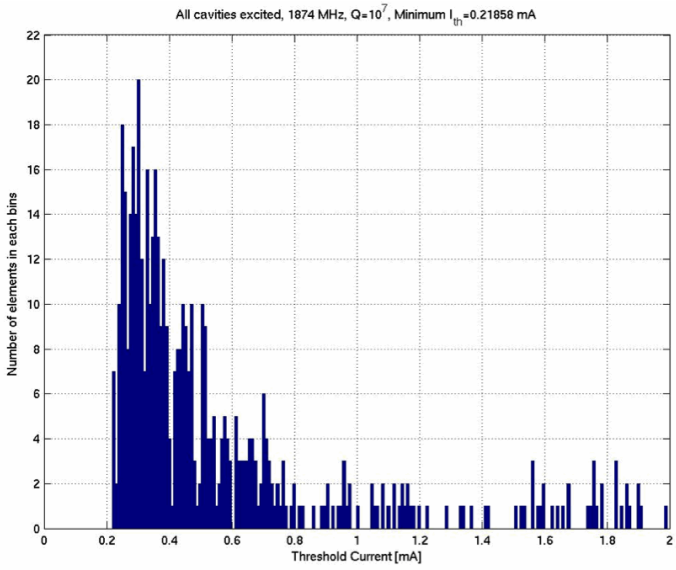

Fig. 3.4: BBU simulation result using DBA arc optics for the 1874 MHz dipole mode with $Q_L = 1 \times 10^7$. The 1874 MHz mode was excited in each cavity and the frequencies were randomly distributed with the full width of 1 MHz. By this method, 500 samples with different HOMs distribution were made. The horizontal axis is the BBU threshold current in mA, and the vertical axis is the number of occurrences. Note that the minimum threshold current is 0.219 mA for $Q_L = 1 \times 10^7$.

current for the DBA optics was found to be 219 μA for $Q_L = 1 \times 10^7$, compared to 231 μA for the previous 4 GeV optics. The threshold current decreased by

approximately 5.2%.

The dependence of the BBU threshold current on Q_L value was investigated. Using the dependence study, one can scale the threshold current according to Q_L values. The cavities located in the 21st cryomodule were excited with only the 1874 MHz mode, and the Q_L value was varied from 1×10^3 to 1×10^8. The results of the study in Table 3.2 shows that the BBU threshold current is inversely proportional to Q_L when $Q_L > 1 \times 10^6$. Therefore, the threshold current can be

Q_L	1×10^3	1×10^4	1×10^5	1×10^6	1×10^7	1×10^8
Threshold current [mA]	1454.5	268.3	50.5	5.7	0.57	0.057

Table 3.2: Dependence of the threshold current on Q_L value.

scaled with the Q_L value when $Q_L > 1 \times 10^6$. In the 12 GeV Upgrade using the DBA arc optics, the HOM damping requirement for 1874 MHz is $Q_L < 7.12 \times 10^6$. The other HOMs damping requirements also can be scaled down by 5.2% of the Q_L values in Table 3.1.

It is notable that, for the BBU simulation analysis, a large number of HOM samples by the variation of an HOM frequency are needed to obtain a sufficient statistical certainty. Small numbers of HOM samples could give premature results because the threshold current changes very rapidly with respect to an HOM frequency.

3.3.2 Two 6 GeV Setups at the 12 GeV Upgrade Accelerator

The study of BBU threshold current for a 6 GeV beam in the 12 GeV accelerator was performed because nuclear physicists may still require a 6 GeV beam after the accelerator has been upgraded to 12 GeV. Three beamline setups were considered in this work: 3-pass, 6.6 GeV; 5-pass, 6.6 GeV; 5-pass, 11 GeV. Only the 1874 MHz mode in Table 3.1 was excited in the 7-cell cavities.

The three energy setups are described in the following sections. For comparison, note that the 12 GeV nominal setup is the 5-pass, 11 GeV setup, and each linac has a 1.1 GeV energy gain; the 3-pass, 6.6 GeV setup also has a 1.1 GeV energy gain per linac; the 5-pass, 4 GeV setup has a 0.4 GeV energy gain in each linac.

3.3.2.1 3-pass, 6.6 GeV Setup

In the 3-pass, 6.6 GeV setup, the linacs have a gradient of 1.1 GeV/linac, which is the nominal energy gain of the 12 GeV setup. Three passes with the energy gain of 1.1 GeV/linac produce a 6.6 GeV beam:

$$\begin{aligned} \text{Energy gain for 3 passes} &= \text{Energy gain per linac} \times \text{Number of linacs} \\ 6.6\ \text{GeV} &= 1.1\ \text{GeV} \times 6\ \text{linacs} \end{aligned} \tag{3.4}$$

Since all different pass (or energy) beams should travel through the same

speaders and recombiners, the injection energy should satisfy the relation [34]:

$$\text{Injection energy} = \frac{9}{80} \times \text{Energy gain per linac.} \tag{3.5}$$

The injection energy for the 3-pass, 6.6 GeV setup will be 123 MeV, which is an important parameter for BBU simulations. The minimum threshold current was found out to be 537 μA, as shown in Figure 3.5.

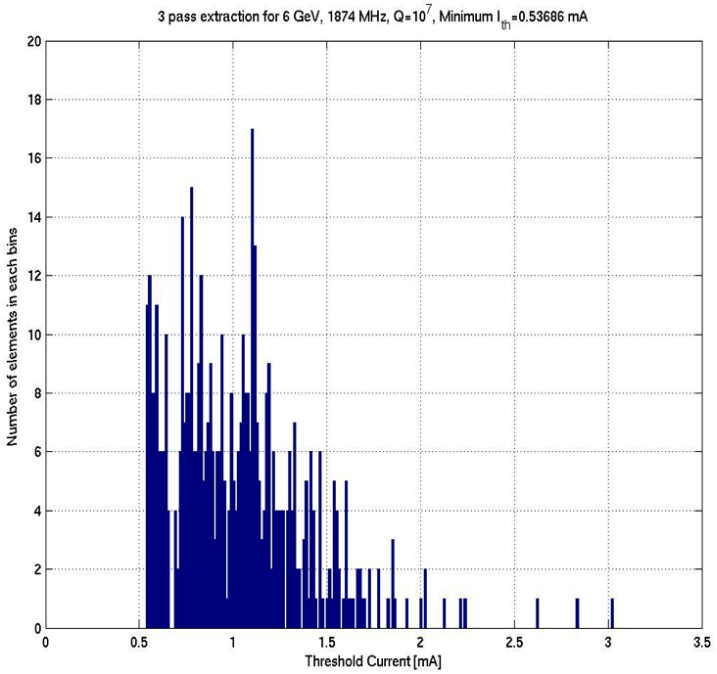

Fig. 3.5: BBU threshold histogram for the 1874 MHz mode with $Q_L = 1 \times 10^7$ using the 3-pass, 6.6 GeV setup. The minimum threshold current is 537 μA.

3.3.2.2 5-pass, 6 GeV Setup

The 60% down version of the 12 GeV setup is the 5-pass, 6.6 GeV setup. The energy gain in linacs and the injection energy are reduced to 60% of the 12

GeV setup values.

$$\begin{aligned} \text{Energy gain for 5 passes} &= \text{Energy gain of 12 GeV nominal setup} \times \frac{60}{100} \\ 6.6 \text{ GeV} &= 11 \text{ GeV} \times \frac{60}{100} \end{aligned} \tag{3.6}$$

From Equation 3.5, the injection energy for the 5-pass, 6 GeV setup is 73 MeV. The minimum threshold current is 131 μA, as shown in Figure 3.6.

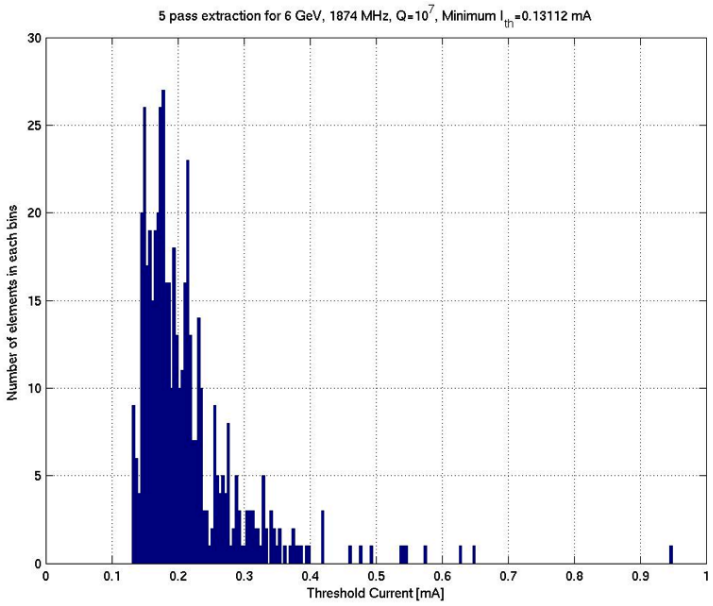

Fig. 3.6: BBU threshold histogram for the 1874 MHz mode with $Q_L = 1 \times 10^7$ using the 5-pass, 6.6 GeV setup. The minimum threshold current is 131 μA.

3.3.2.3 Comparison of Threshold Currents for Three Different Setups

Table 3.3 summarizes the simulation results. The threshold current for the 3-pass, 6.6 GeV setup is approximately four times greater than for the 5-pass,

6.6 GeV setup. Consider two 5-pass setups: the 5-pass, 6.6 GeV and the 5-pass, 11 GeV. As the beam energy is reduced from 11 GeV to 6.6 GeV, which is 60 % reduction, the threshold current and injection energy are also decreased approximately 60 %. It is notable that the threshold current is proportional to the injection energy while the pass number is fixed.

	3-pass, 6.6 GeV	5-pass, 6.6 GeV	5-pass, 11 GeV
Threshold current	715 μA	174 μA	292μA
Injection energy	123 MeV	73 MeV	123 MeV

Table 3.3: Comparison of threshold currents for three different energy setups. The threshold currents are scaled with $Q_L = 7.51 \times 10^6$ using the simulation results for $Q_L = 1 \times 10^7$.

3.3.2.4 Availability of the Maximum Beam Current

The maximum beam current can be limited by the beam dump power.

$$\text{Beam dump power} \geq \text{Beam current} \times \text{Beam energy} \,/\, \text{Electron charge} \quad (3.7)$$

The maximum beam dump power of CEBAF is 1 MW. Applying 6.6 GeV beam energy and 1 MW beam dump power to the formula yields the maximum available beam current, 151 μA. This maximum available beam current is lower than the minimum BBU threshold currents for the two 6.6 GeV setups in Table 3.3. Therefore, the operation of the maximum beam current, 151 μA, is feasible for

the two 6.6 GeV setups under the damping requirements in Table 3.1. However, the 3-pass setup is a better choice than the 5-pass setups because the threshold current of 715 μA for 3-pass setup is greater than the threshold current of 174 μA for 5-pass setup.

3.4 Simulations of Cumulative BBU

A cumulative BBU mechanism occurs for a single pass beam in a linac consisting of a series of cavities. A cumulative BBU effect is particularly serious in its transient behavior, where the amplitude growth can become very large [10]. In this section, the simulation study of the transient behavior in an injector prototype for the 12 GeV Upgrade is illustrated.

3.4.1 Cumulative BBU Instability

The cumulative BBU applies to a single pass beam through a series of cavities. Suppose a beam enters the first cavity with an offset from the central axis. They excite a dipole HOM, which can cause a subsequent beam to be deflected. This deflected beam can excite the stronger HOM in the next cavity, and then the stronger HOM will further deflect the later portions of the beam. The further deflected beam will excite the HOM in the next cavity even more effectively, and so on. Ultimately, the beam transverse amplitude may increase to the wall of the accelerating structure and be lost [10,35]. This beam loss is due to a steady state

behavior.

In addition to this steady state behavior, another concern is transient behavior. Even though the beam behavior eventually reaches a steady state, the transverse amplitude due to the transient behavior should not be greater than a physical aperture of a beamline structure. The purpose of this study is to prove that the transverse amplitude does not increase to the size of a physical aperture in the new injector for the 12 GeV Upgrade.

3.4.2 Injector for the 12 GeV Upgrade

A new injector for the 12 GeV Upgrade is under development. A preliminary prototype of the new injector consists of one 7-cell cavity and two single cell cavities. A simulation study of cumulative BBU for the injector prototype was performed using *TDBBU* to determine the damping requirement of dipole HOMs for the new cavities and the necessity of HOM filters.

Cumulative BBU can be characterized into two parts: the transient behavior and the steady state behavior. Since the injector is short, the transverse displacement at the steady state is not a concern. However, the transverse amplitude due to the transient behavior should be smaller than a physical aperture of the injector beamline. This study proved that the transverse amplitude does not increase to the size of a physical aperture for the new injector and the HOM filters are unnecessary [11].

3.4.3 Numerical Simulations

Figure 3.7 shows the layout of the system considered in this study. It consists of two single-cell (6.35 cm long) and one 7-cell (70 cm long) superconducting RF cavities with an energy gain of 351 keV, 198 keV, and 3.87 MeV for the first, second, and third cavity respectively. Table 3.4 lists the basic parameters of this study, and Table 3.5 summarizes the HOM information used for simulations.

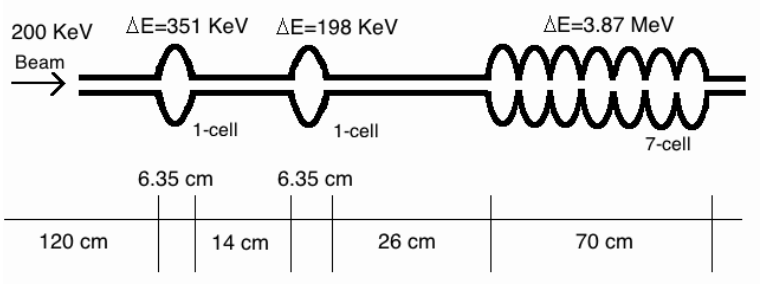

Fig. 3.7: Schematic of the injector prototype layout.

Initial beam energy	200 keV
Energy gain at 1st cavity	351 keV
Energy gain at 2nd cavity	198 keV
Energy gain at 3rd cavity	3.87 MeV
Beam currents	0.5 mA, 1 mA, 2 mA, 4 mA
Initial offset	0.1 cm, 0.2 cm, 0.5 cm, 1.0 cm
Q_L	$1 \times 10^8 \sim 1 \times 10^{12}$

Table 3.4: Parameters for injector simulations.

Cavity type	f [MHz]	R/Q [Ω]	Mode	f [MHz]	R/Q [Ω]	Mode
Single cell	2191.022	53.21	TM_{110}	3566.095	3.77	TM_{111}
	2597.643	7.94	TE_{111}			
7-cell	1972.051	26.28	TE_{111}	2190.125	71.53	TM_{110}
	1973.631	49.74	TE_{111}	2191.228	66.95	TM_{110}
	2007.498	56.93	TE_{111}	2206.870	37.26	TM_{110}
	2007.606	49.29	TE_{111}	2207.985	36.82	TM_{110}
	2133.432	12.90	TM_{110}	2884.505	106.36	TM_{111}
	2134.560	11.58	TM_{110}	2884.563	107.28	TM_{111}
	2168.758	36.42	TM_{110}	2889.306	15.59	TM_{111}
	2169.856	35.41	TM_{110}	2889.817	17.49	TM_{111}

Table 3.5: HOM characteristics used for injector simulations.

3.4.4 RF Focusing Effect

As described in Section 3.2, the RF focusing effect was implemented in *TDBBU*. Cumulative BBU simulations using *TDBBU* showed the RF focusing effect as in Figure 3.8. When there is no RF focusing effect, the transverse position stays at the initial offset (see Figure 3.8a). When the RF focusing influences the beam, the centroid of the beam is shifted to the center line (see Figure 3.8b).

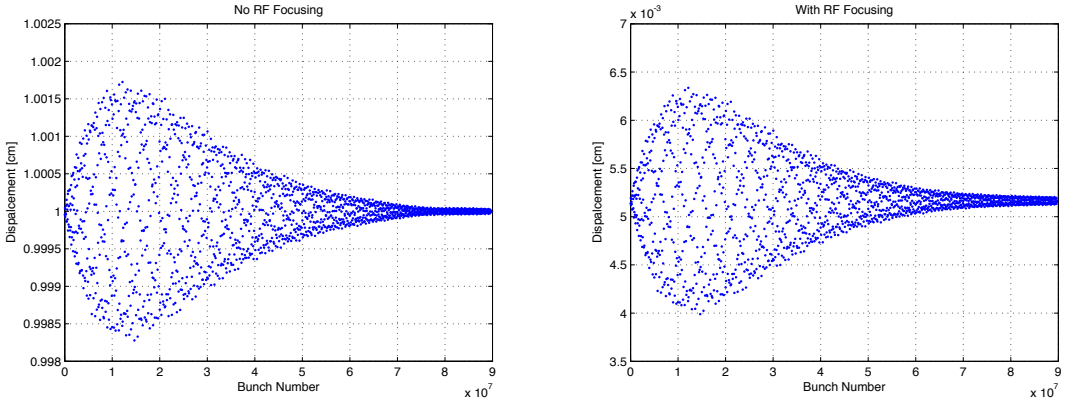

(a) RF focusing inactive. **(b)** RF focusing active.

Fig. 3.8: Transverse displacement versus particle number for the injector prototype design when the RF focusing effect is active and inactive. The transverse position is observed at the exit of the injector. The transverse initial offset is set to 1 cm. The beam current is 1 mA, and the Q_L value is 1×10^{12}.

3.4.5 Transient Behavior

3.4.5.1 Dependence on Q_L Values

To see the dependence of the transient behavior on Q_L value, the Q_L value varies from 1×10^8 to 1×10^{12}, and other parameters are fixed. As the Q_L value increases, the maximum transverse displacement and its build-up time increase [10, 36], as shown in Figure 3.9 and 3.12. Four example plots for different Q_L values in Figure 3.12 show the transient behavior, which is the signature of the cumulative BBU, eventually becomes stable, and reaches a steady state.

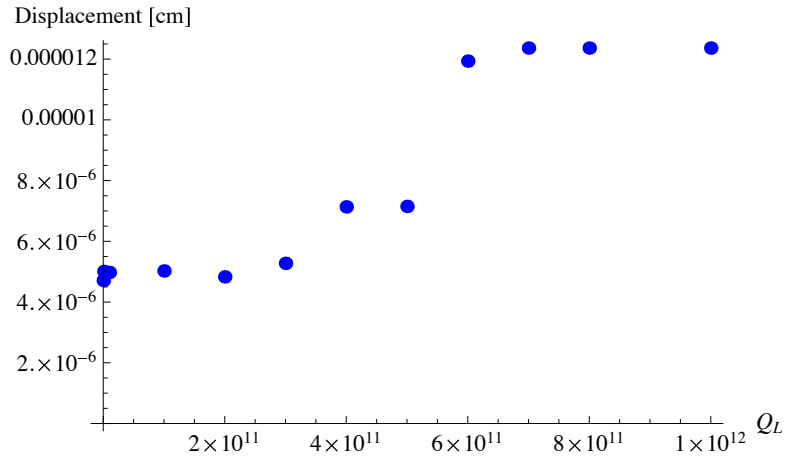

Fig. 3.9: Dependence of transverse displacement on Q_L. The beam current is 1 mA with the initial offset of 1 cm.

3.4.5.2 Dependence on Beam Current

The beam current is varied while the other parameters are fixed. The maximum transverse displacement has a quadratic dependence on beam current, as shown in Figure 3.10 and 3.13. This is expected because the energy gain or loss of a particle is proportional to the square of the particle charge [15, 37].

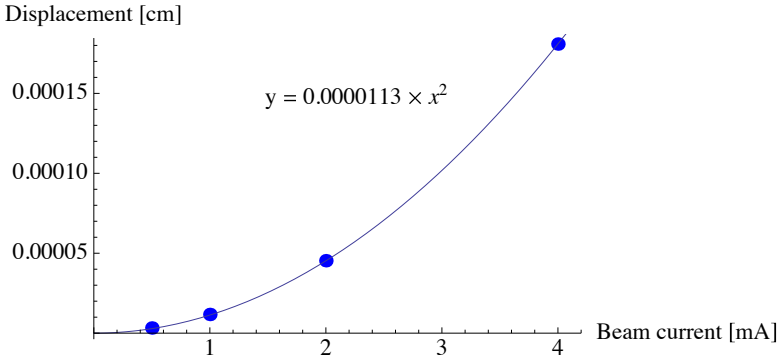

Fig. 3.10: Dependence of transverse displacement on beam current. The initial offset is 1 cm and $Q_L = 1 \times 10^{12}$.

3.4.5.3 Dependence on Initial Transverse Offset

Figure 3.11 and 3.14 illustrates the dependance on the beam initial offset. The initial transverse displacement is varied while the other parameters are fixed. The maximum displacement is proportional to the initial offset, as expected by the fact that the level of HOM excitation is proportional to the transverse displacement [15, 37].

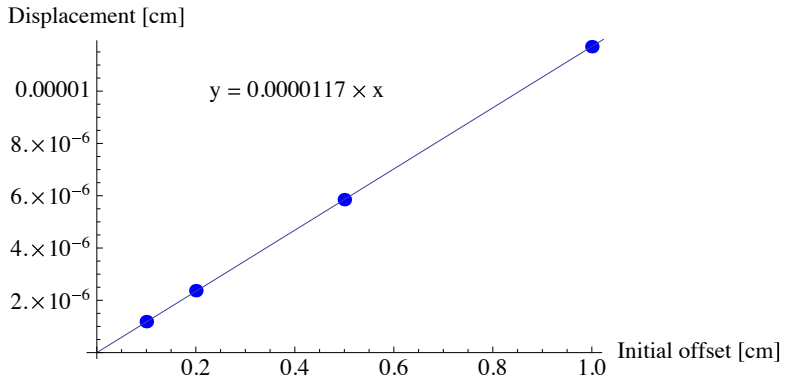

Fig. 3.11: Dependence of transverse displacement on initial transverse offset. The beam current is 1 mA and $Q_L = 1 \times 10^{12}$.

3.4.6 Conclusion from Simulations

The simulation results reveal that the RF cavities in the injector prototype design do not need HOM filters for HOM damping to reduce the transient behavior amplitude. The transverse amplitude is less than the physical aperture of the beam line even in an extreme case, such as the transverse initial offset of 1 cm, the beam current of 4 mA, and $Q_L = 1 \times 10^{12}$.

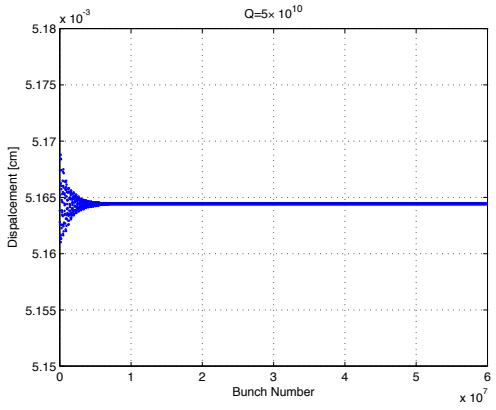

(a) $Q_L = 5 \times 10^{10}$.

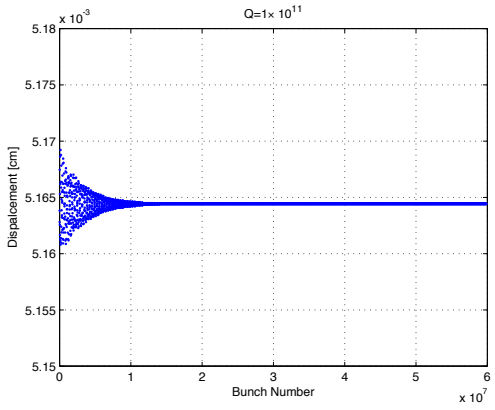

(b) $Q_L = 1 \times 10^{11}$.

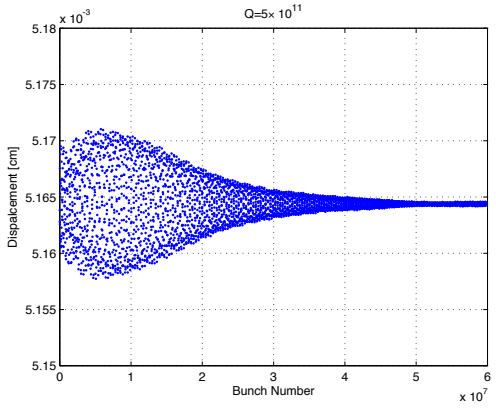

(c) $Q = 5 \times 10^{11}$.

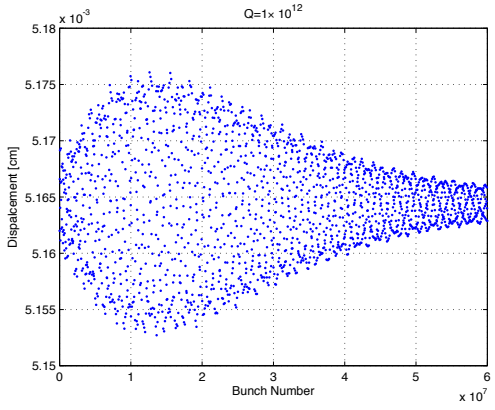

(d) $Q = 1 \times 10^{12}$.

Fig. 3.12: Transverse displacement versus particle number for different Q_L values. The transverse position is observed at the exit of the injector. The beam current is 1 mA, and the initial offset is 1 cm.

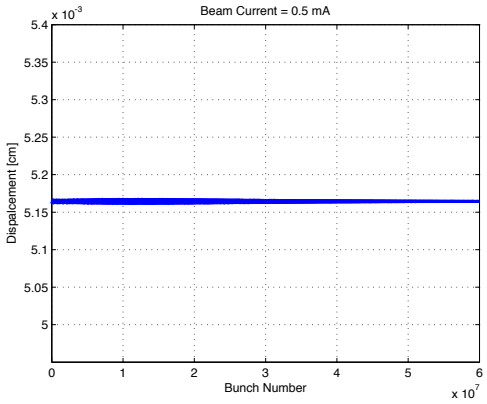

(a) Beam current = 0.5 mA.

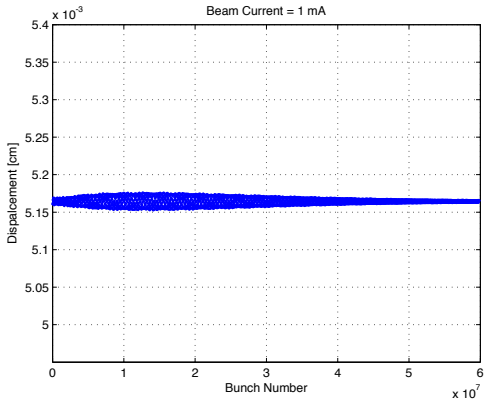

(b) Beam current = 1 mA.

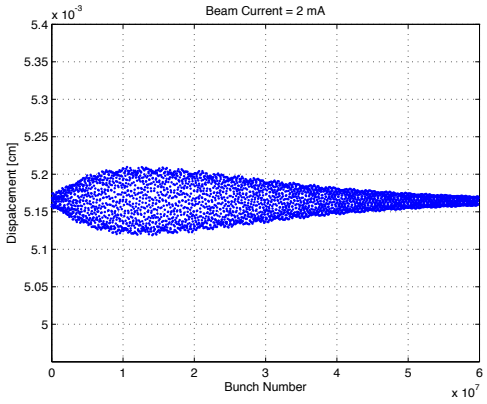

(c) Beam current = 2 mA.

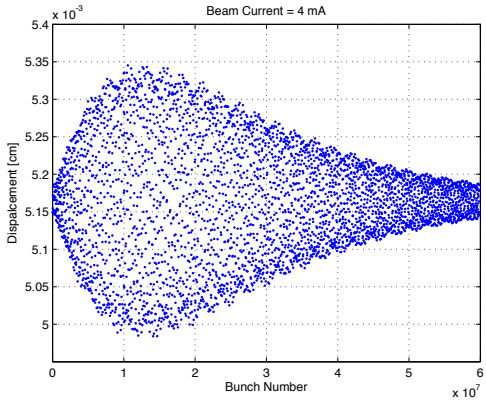

(d) Beam current = 4 mA.

Fig. 3.13: Transverse displacement versus particle number for different beam currents. The transverse position is monitored at the exit of the injector. The beam has the initial offset of 1 cm and $Q_L = 1 \times 10^{12}$.

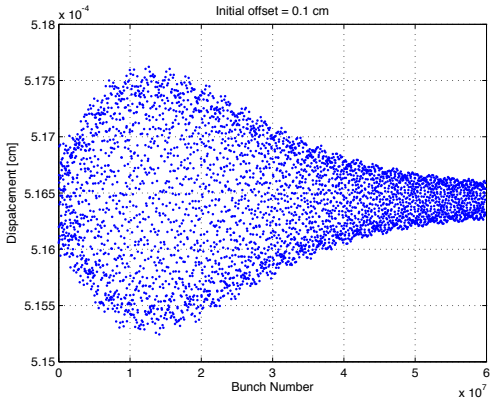

(a) Initial offset = 0.1 cm.

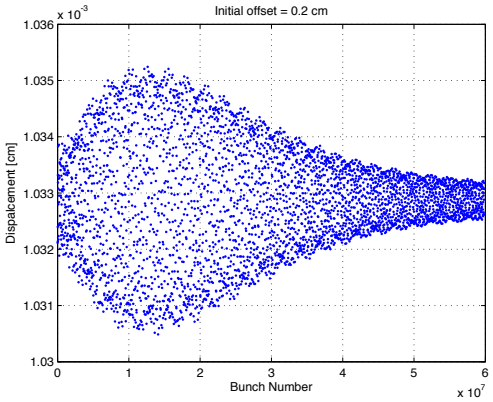

(b) Initial offset = 0.2 cm.

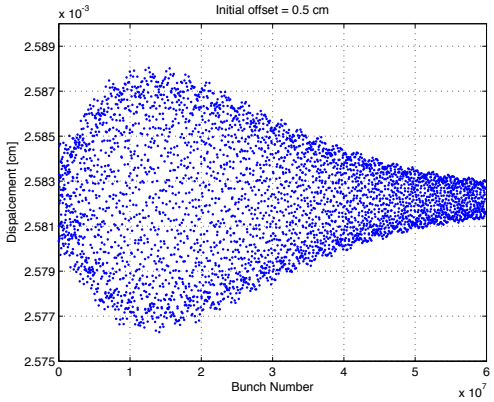

(c) Initial offset = 0.5 cm.

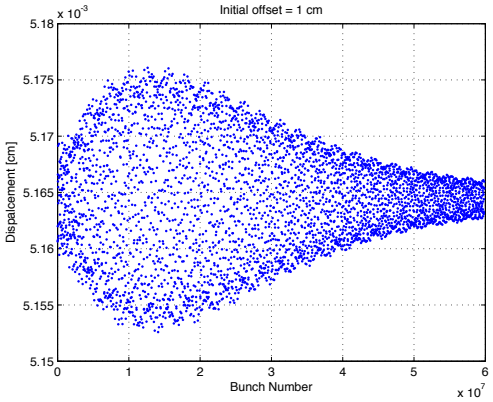

(d) Initial offset = 1.0 cm.

Fig. 3.14: Transverse displacement versus particle number for different transverse initial offsets. The transverse position is monitored at the exit of the injector. Note the y-axis scales are different in each subplot. The beam current is 1 mA and $Q_L = 1 \times 10^{12}$.

Chapter 4

The BBU Experiment and Measurements

4.1 Overview

The BBU experiment was performed to experimentally investigate BBU instability and to estimate the BBU threshold current for two operational cryomodules for the 12 GeV Upgrade. This experiment consists of a series of RF measurements with and without beam to characterize HOMs and estimate the BBU threshold.

A new cryomodule for the 12 GeV Upgrade contains eight new 7-cell RF cavities. The first two fabrications, named C100-1 and C100-2, were installed at CEBAF for operational testing, including the BBU experiment. Once the RF cavities are mounted in a cryogenic vessel and fabricated as a cryomodule, it is technically difficult to manipulate HOM properties such as the resonant frequency, ω_λ, the impedance, $(R/Q)_\lambda$, and the loaded quality factor, Q_λ. Therefore, before installing a cryomodule in CEBAF, the HOM characteristics should be carefully and thoroughly surveyed. With regard to BBU instability, the HOM properties

are characterized as $(R/Q)_\lambda Q_\lambda\, k_\lambda$ in Equation (2.51). The quantity $(R/Q)_\lambda$ is calculated by computer simulation, and the quantities Q_λ and $k_\lambda = \frac{\omega_\lambda}{c}$ are measured using a network analyzer. The HOMs survey process measures Q_λ and $f_\lambda = \frac{\omega_\lambda}{2\pi}$ for all HOMs of interest to evaluate their HOM impedances.

The HOM survey for C100-1 and C100-2 was performed in the Cryomodule Test Facility (CMTF) at Jefferson Lab. The survey results showed that the HOM damping requirements for BBU were satisfied. After the HOM survey in the CMTF, then the two cryomodules were installed at the end of the South Linac of CEBAF at the locations named SL24 and SL25. Under various beam conditions, the same measurements as in the CMTF were conducted. Details of the experimental setups and measurements will be discussed in this chapter.

4.2 RF Measurement: Network Analyzer and Scattering Matrix

A network analyzer (NWA) is one of the most important instruments used for microwave measurements, and was used extensively for this experiment. An NWA measures the response of a device under test (DUT) to an applied sinusoidal input over a range of frequencies. Figure 4.1 shows a schematic illustrating the RF measurement using an NWA. For a given input to a DUT, the incident wave is reflected, transmitted, and attenuated or amplified. $V_{1,in}$ and $V_{2,in}$ are the voltages of incident waves towards port 1 and 2 of the DUT, and $V_{1,out}$ and $V_{2,out}$ are the voltages of emerging waves out of the two ports of the DUT. The scattering matrix

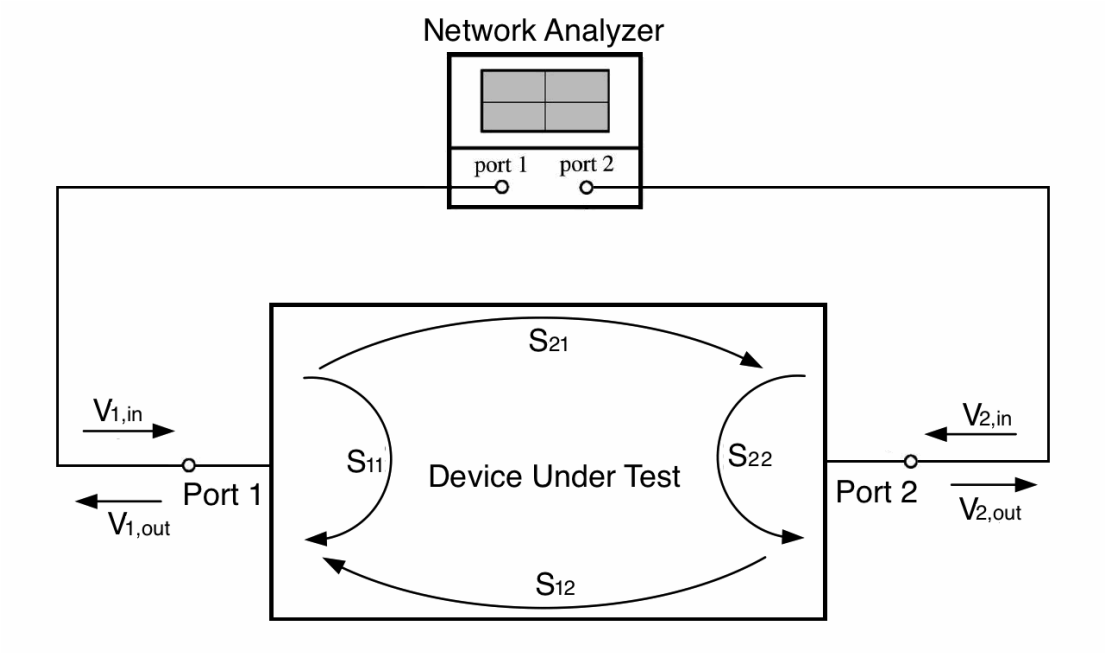

Fig. 4.1: Schematic of a network analyzer.

is defined in terms of voltages, easily measured with an NWA [38, 39]:

$$\begin{pmatrix} V_{1,out} \\ V_{2,out} \end{pmatrix} = \begin{pmatrix} S_{11} & S_{12} \\ S_{21} & S_{22} \end{pmatrix} \begin{pmatrix} V_{1,in} \\ V_{2,in} \end{pmatrix} . \tag{4.1}$$

The matrix elements, S_{11}, S_{12}, S_{21}, and S_{22}, are referred to as the scattering parameters or the S-parameters.

The NWA supplies a known voltage to each port. A voltage $V_{1,in}$ is applied to port 1 of the DUT, and no voltage to port 2. All ports are terminated in the characteristic impedance of the NWA ports and cables to the DUT, which guarantees that $V_{2,in} = 0$. The voltages of the emerging waves out of the ports,

$V_{1,out}$ and $V_{2,out}$, are measured:

$$\begin{pmatrix} V_{1,out} \\ \\ V_{2,out} \end{pmatrix} = \begin{pmatrix} S_{11} & S_{12} \\ \\ S_{21} & S_{22} \end{pmatrix} \begin{pmatrix} V_{1,in} \\ \\ 0 \end{pmatrix}, \tag{4.2}$$

or

$$S_{11} = \frac{V_{1,out}}{V_{1,in}} \qquad \text{and} \qquad S_{21} = \frac{V_{2,out}}{V_{1,in}}. \tag{4.3}$$

The parameter S_{11} is the reflection coefficient, and S_{21} is the transmission coefficient when the output port is terminated by the characteristic impedance. The numbering convention for the S-parameters is that the first number following the S is the port at which energy emerges, and the second number is the port at which energy enters. For example, S_{21} is a measure of the power emerging from port 2 as a result of applying an RF signal into port 1.

Squaring the S-parameters relates an input and output power to the DUT's reflection and transmission behavior:

$$|S_{11}|^2 = \frac{\text{Power reflected from port1}}{\text{Power incident on port 1}} \tag{4.4}$$

$$|S_{21}|^2 = \frac{\text{Power emerging from port 2}}{\text{Power incident on port 1}}. \tag{4.5}$$

The power ratios are usually presented as the logarithmic expression in units of decibels (dB) such as

$$S_{21}^{[dB]} \equiv 10 \log |S_{21}|^2 \tag{4.6}$$

$$= 20 \log |S_{21}|. \tag{4.7}$$

This measurement of S_{21} was used to determine the quality factors, Q_λ, of the dipole modes, and the S_{21} measurement setup was also used for the beam transfer function measurement in the experimental studies of BBU.

Figures 4.2 and 4.3 are examples of the S_{21} measurement using an NWA. It displays $S_{21}^{[dB]}$ versus the frequency. The transmission coefficient, $S_{21}^{[dB]}$, becomes very large at the frequency of a resonant mode and rapidly decreases as the frequency deviates from the resonant frequency.

4.3 HOM Survey at CMTF

The first two C100 cryomodules, named C100-1 and C100-2, were surveyed in the CMTF at Jefferson Lab in June and September, 2011. The survey was to characterize HOMs and verify conformity to the HOM damping requirement for the 12 GeV Upgrade. Figure 4.4a shows the experimental setup in the CMTF. Transmission scattering parameters, S_{21}, were measured through a single cavity using its own and neighboring HOM ports as illustrated in Figure 4.4b. The HOM in the cavity was excited directly through port 1 using an HOM coupler. The HOM signal was then detected through port 2 using another HOM coupler located at a neighboring cavity. Using a four-port NWA in actual measurements, four transmission scattering parameters of different configurations were measured by connecting port A and A′; A and B′; B and A′; B and B′.

Table 4.1 lists the HOM survey ranges. A maximum number of sample

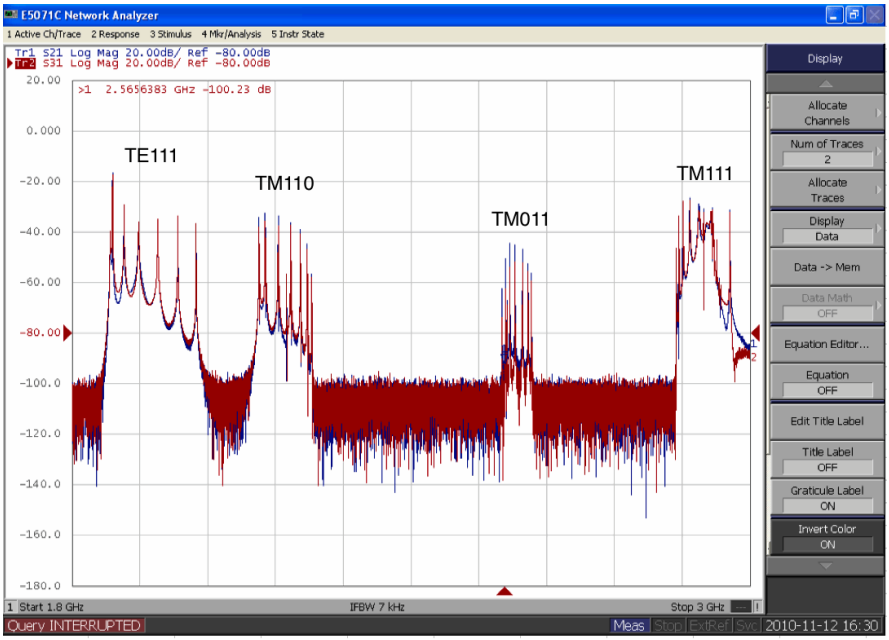

(a) Full range spectrum between 1850 and 3050 MHz.

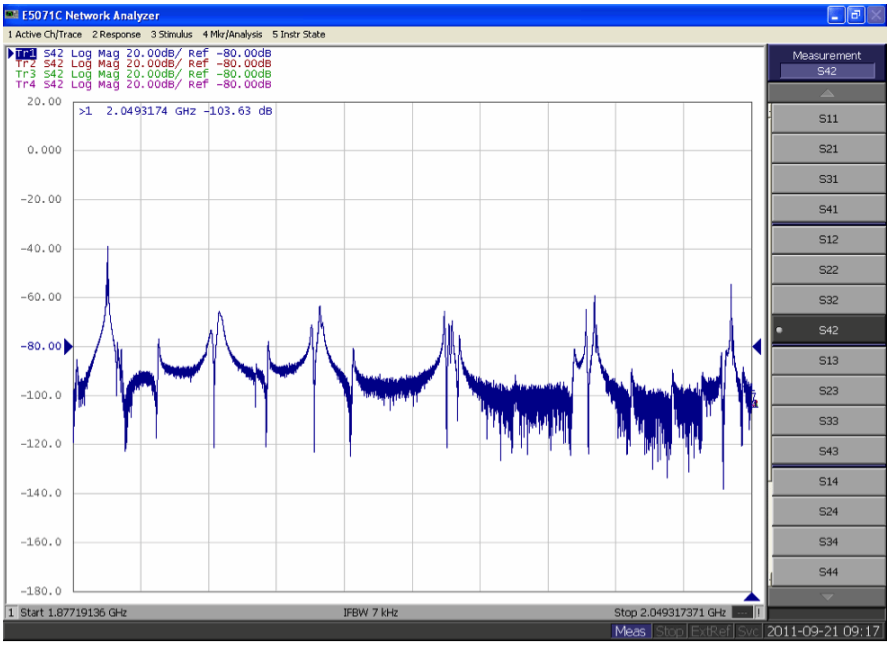

(b) TE_{111} mode spectrum.

Fig. 4.2: Screenshot of HOM measurements in the CMTF. Full spectrum and TE_{111} mode for Cavity 6 in C100-1.

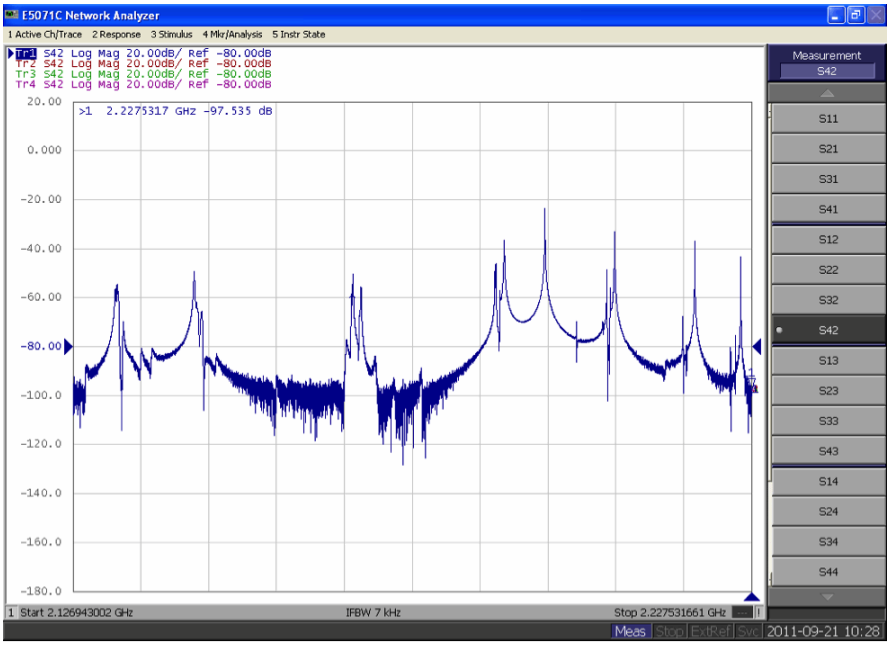

(a) TM_{110} mode spectrum.

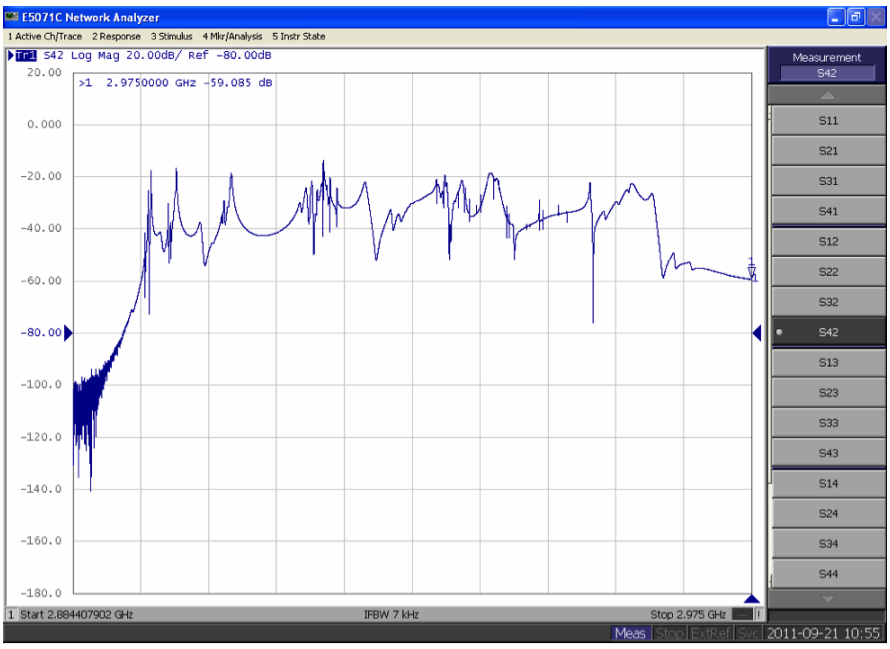

(b) TM_{111} mode spectrum.

Fig. 4.3: Screenshot of HOM measurements in the CMTF. TM_{110} and TM_{111} modes for Cavity 6 in C100-1.

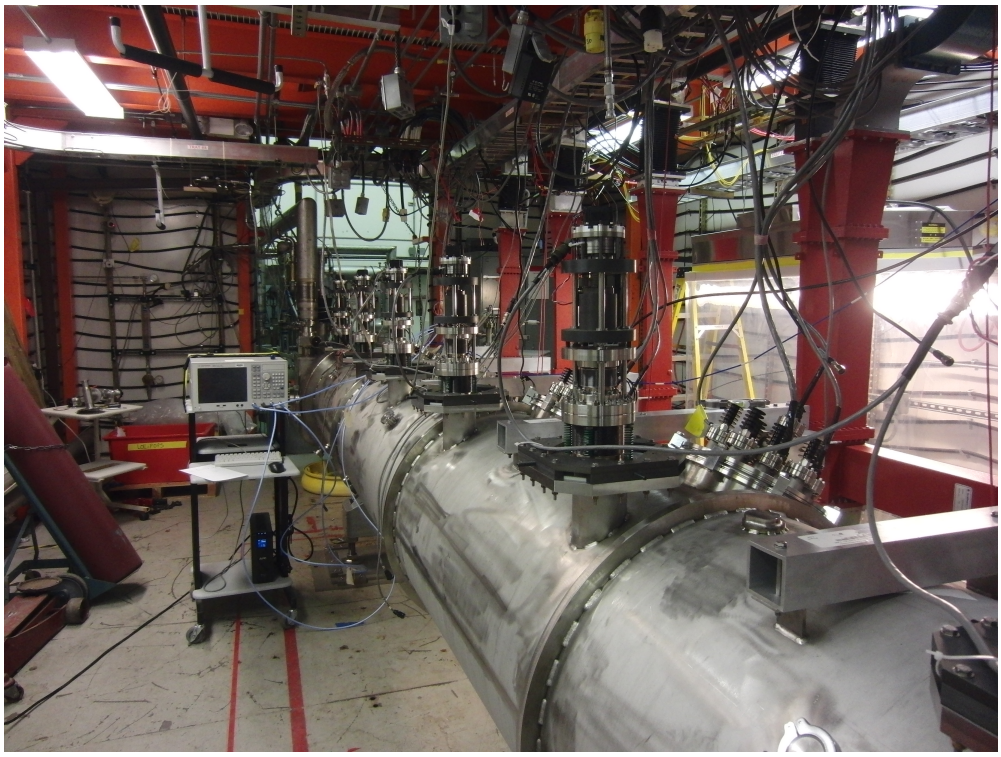

(a) HOM survey setup in the CMTF.

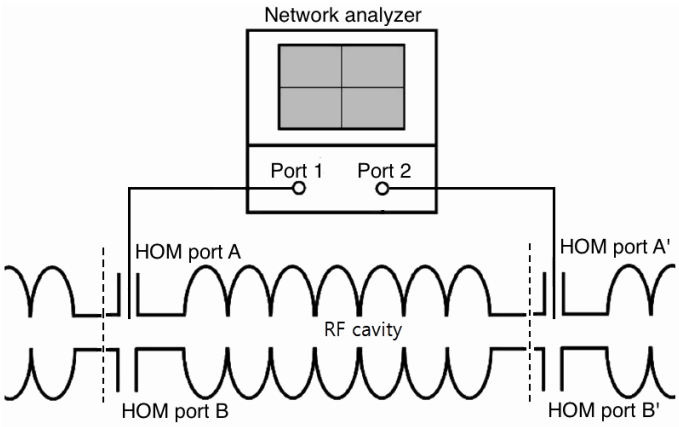

(b) Schematic of the HOM survey setup. The dotted lines separate cavities in a cryomodule. Two HOM couplers are oriented 120 degrees with respect to each other [13,40]. Four S_{21} were measured by connecting to port A and A′; A and B′; B and A′; B and B′.

Fig. 4.4: HOM measurements in the CMTF.

HOM	Survey range
TE_{111} mode	$1850 \sim 2050$ MHz
TM_{110} mode	$2050 \sim 2250$ MHz
TM_{111} mode	$2850 \sim 3050$ MHz

Table 4.1: C100 HOMs survey ranges. TE_{111}, TM_{110}, and TM_{111} modes are trapped within the cavities. Any dipole HOM above approximately 3 GHz propagates through the beam pipe [13, 41].

points (20001) were taken to guarantee a sufficient spectral resolution of the three modes. Figure 4.2a shows the screenshots of the full range of spectrum, and TE_{111}, TM_{110}, and TM_{111} modes are also shown in Figures 4.2b, 4.3a, and 4.3b.

A laptop computer took the RF measurement data and saved it as a spreadsheet (*Microsoft Excel*) through a data taking application provided by the NWA company. The saved data were analyzed using a *Mathematica* program, named *Polfit* [42], which read the data in the spreadsheet and fit the data with the Lorentzian function to extract the quality factor, Q_λ, as shown in Figure 4.5. This method saved time in measurement of resonance frequencies and Q_λ values compared to direct on-line measurements from a NWA.

Figure 4.6 shows the impedances of TE_{111}, TM_{110}, and TM_{111} modes for all cavities in the C100-1 and C100-2 cryomodules. The impedance values are quite consistent over all cavities. The impedances circled in red are of the most concern

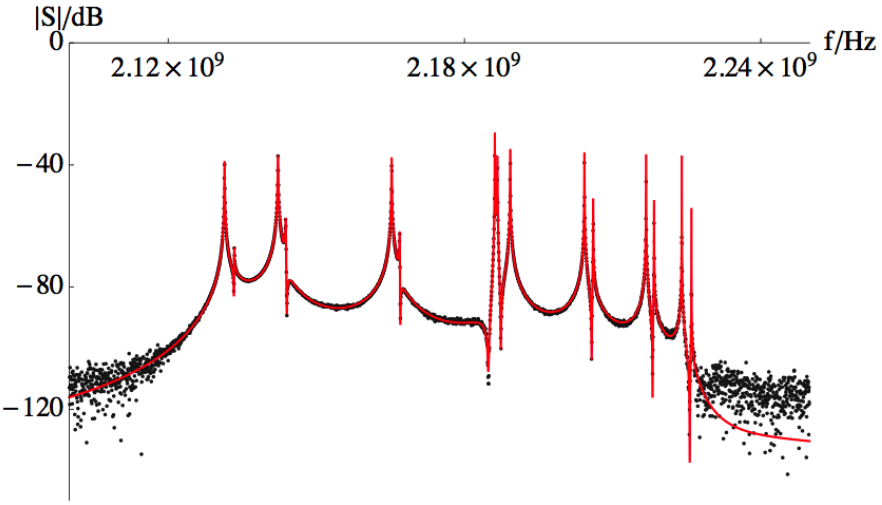

Fig. 4.5: An example of *Polfit* output for TM_{110} mode. Magnitude of $S_{21}^{[dB]}$ versus frequency. The black dots are measured values, and the red line is a fitted value to extract the quality factor, Q_λ. The 7 pairs of peaks corresponds to 7 dipole modes in the 7-cell cavity. (Picture from [42]).

for the BBU performance, but at worst they are still nearly an order of magnitude below the baseline impedance, 10^{10} Ω/m, for the 12 GeV Upgrade.

4.4 HOM Measurement with Beam

4.4.1 Beam Transfer Function Measurement

The beam transfer function (BTF) is a diagnostic method that excites a beam with a periodic signal and measures the resulting beam response, which contains important information on beam and machine properties. An important advantage is the non-destructive nature of the method; a rather weak excitation

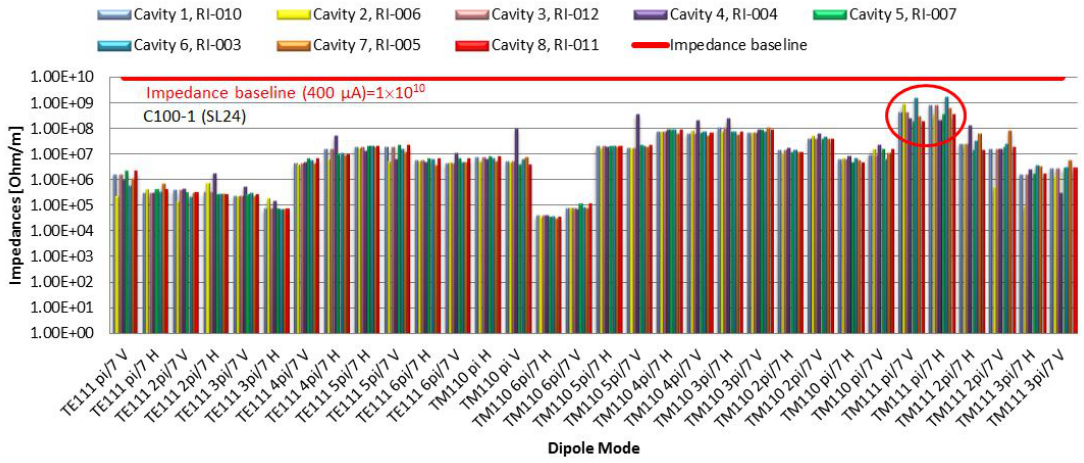

(a) Impedances of C100-1.

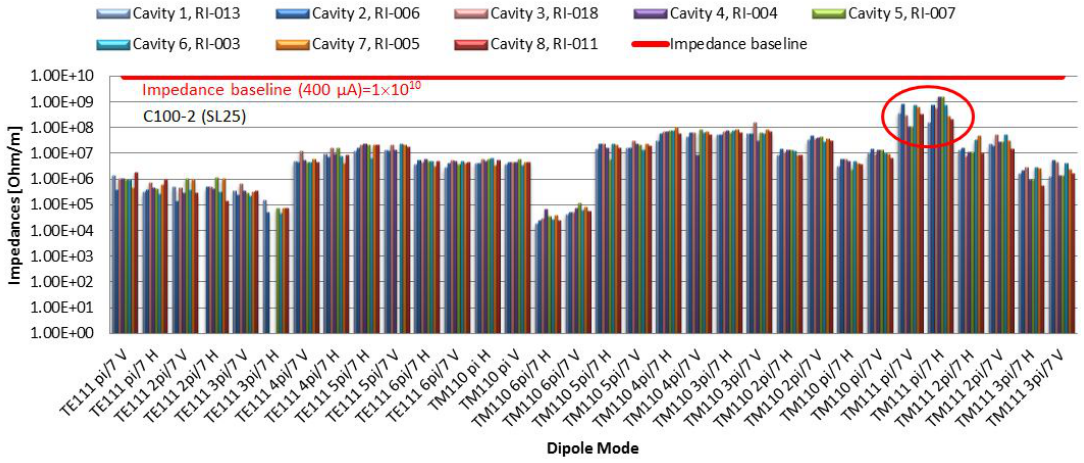

(b) Impedances of C100-2.

Fig. 4.6: Dipole HOM impedances for C100-1 and C100-2. The impedances in the graphs are $(R/Q)_\lambda Q_\lambda k_\lambda$ values in Equation 2.51 . The baseline impedance for 12 GeV with 400 μA is 10^{10} Ω/m. The highest impedances, circled in red, are TM_{111} $\pi/7$ modes near 2893 MHz.

is enough and the beam operation is not disturbed [43, 44]. For the BBU experiment, the BTF measurement allows one to determine the BBU threshold when an accelerator is operated below the threshold current.

Because of the accessibility to the HOM couplers of the cavities, the BTF measurement was simplified substantially by exciting the beam directly through the HOM couplers of the cavity. The response signal was measured from the other HOM coupler of a neighboring cavity.

4.4.2 Optics Modeling

Optics calculations were performed using accelerator simulation codes, *OptiM* and *elegant*. The optics calculations using the two codes provided transfer matrices of the arc optics. These matrices were used for *TDBBU* to compute threshold currents.

To make some variations on the matrix elements, M_{12} and M_{34}, the FODO cells in linacs were set to three different phase advances: 90°, 105°, and 120°. Figure 4.7, 4.8, and 4.9 display the lattice functions for the three setups. The arc optics are the same as the 4 GeV nominal arc optics, and the linacs and the arcs are matched at the spreaders and recombiners as in Figure 4.7d.

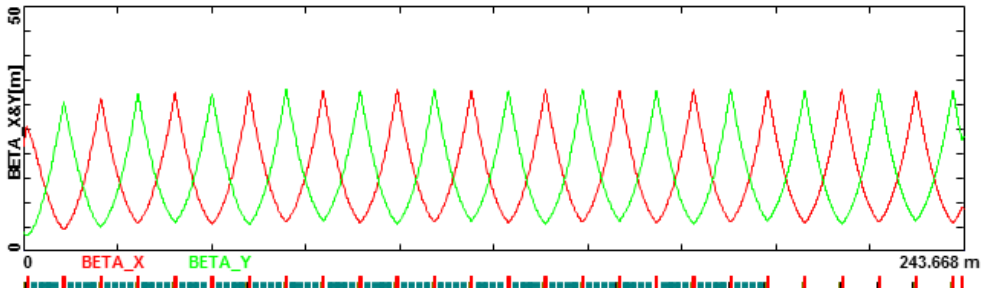

(a) Horizontal (red) and vertical (green) beta functions for the first-pass north linac.

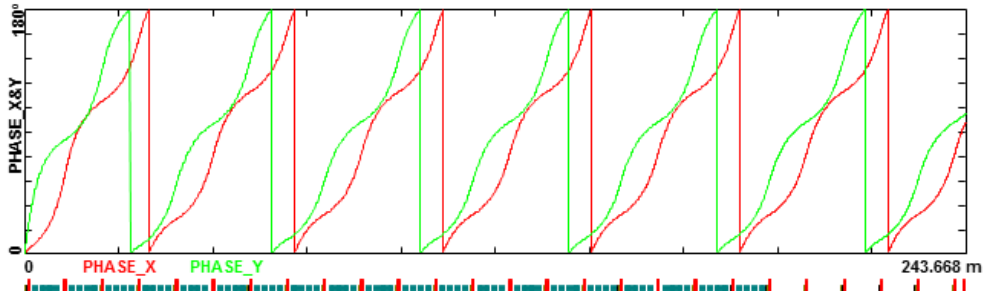

(b) Horizontal (red) and vertical (green) phase advances for the first-pass north linac.

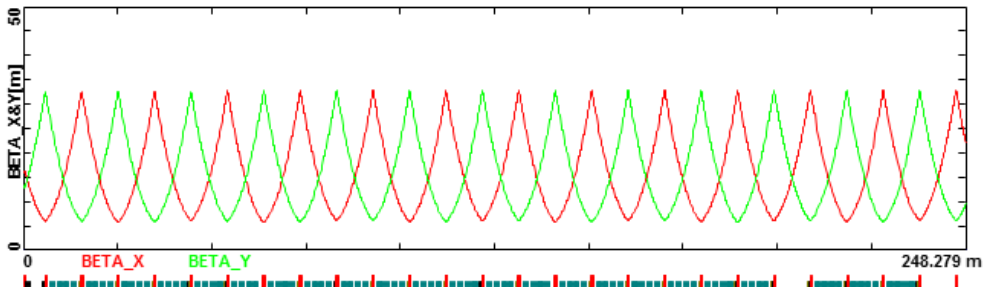

(c) Horizontal (red) and vertical (green) beta functions the first-pass south linac.

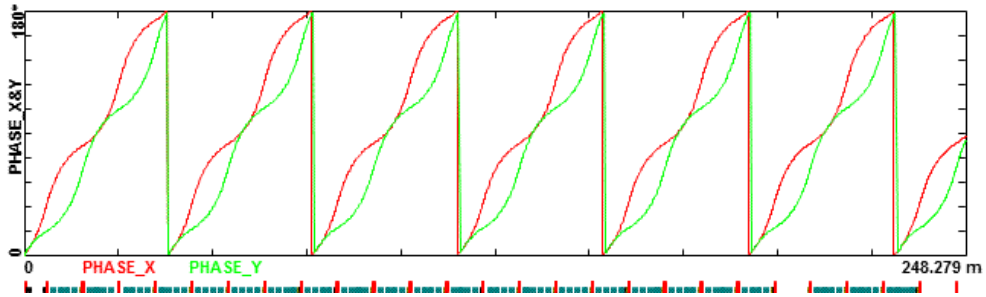

(d) Horizontal (red) and vertical (green) phase advances for the first-pass south linac.

Fig. 4.7: Optics for phase advance 90° setup.

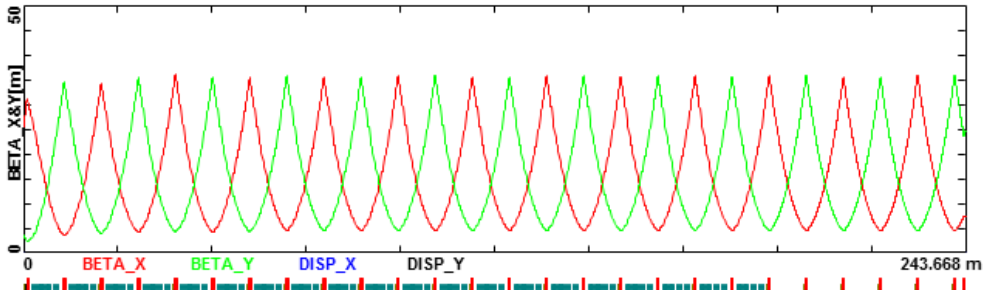

(a) Horizontal (red) and vertical (green) beta functions for the first-pass north linac.

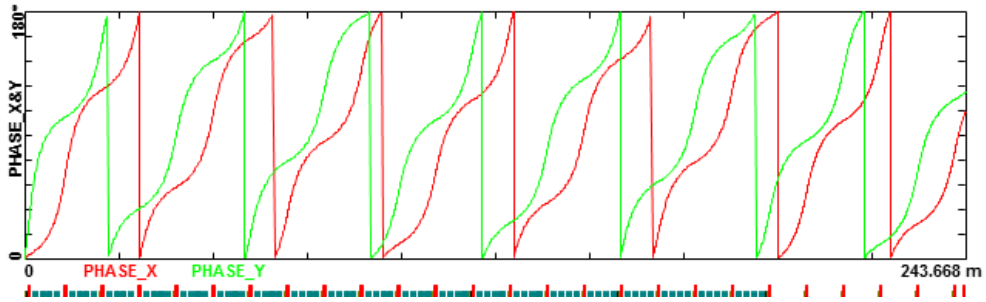

(b) Horizontal (red) and vertical (green) phase advances for the first-pass north linac.

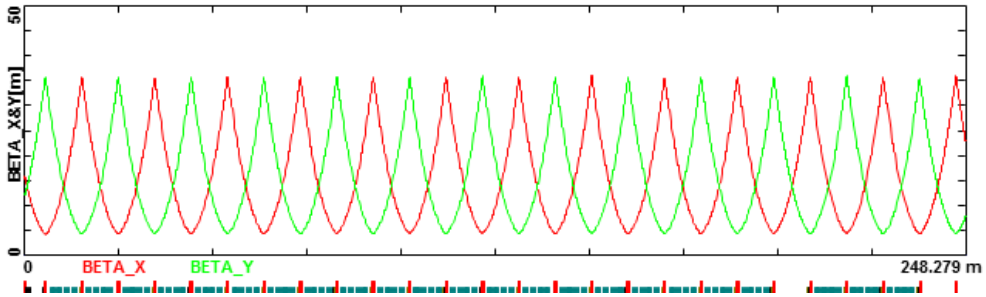

(c) Horizontal (red) and vertical (green) beta functions the first-pass south linac.

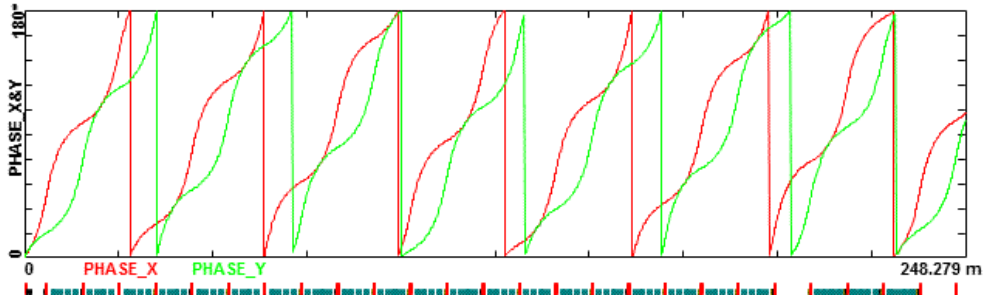

(d) Horizontal (red) and vertical (green) phase advances for the first-pass south linac.

Fig. 4.8: Optics for phase advance 105° setup.

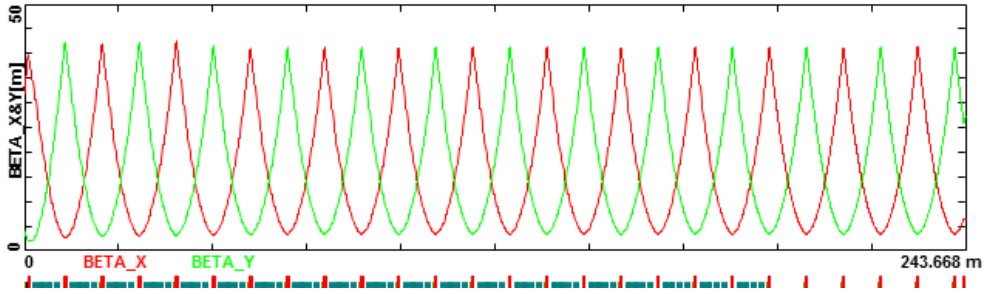

(a) Horizontal (red) and vertical (green) beta functions for the first-pass north linac.

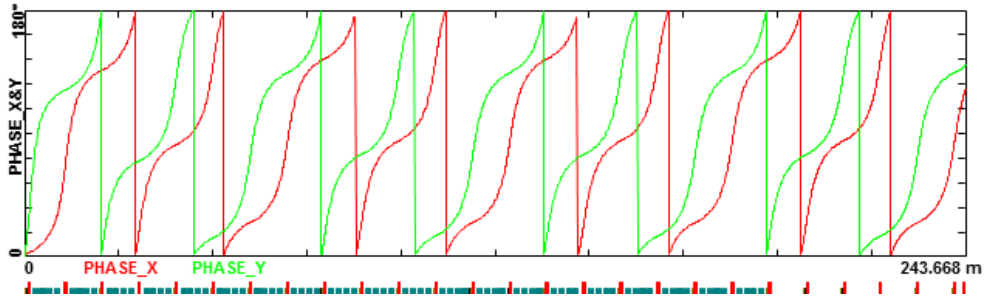

(b) Horizontal (red) and vertical (green) phase advances for the first-pass north linac.

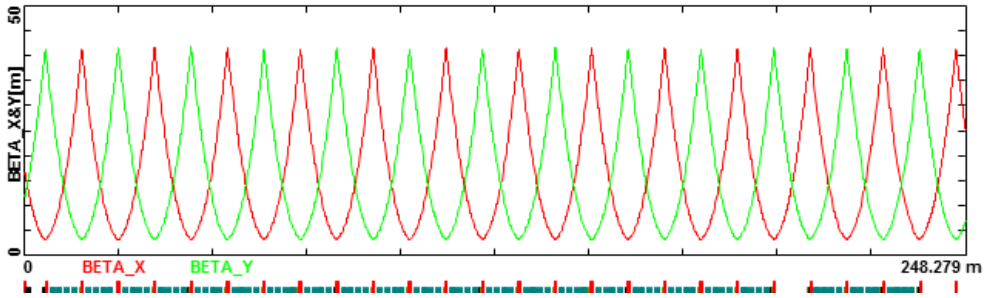

(c) Horizontal (red) and vertical (green) beta functions the first-pass south linac.

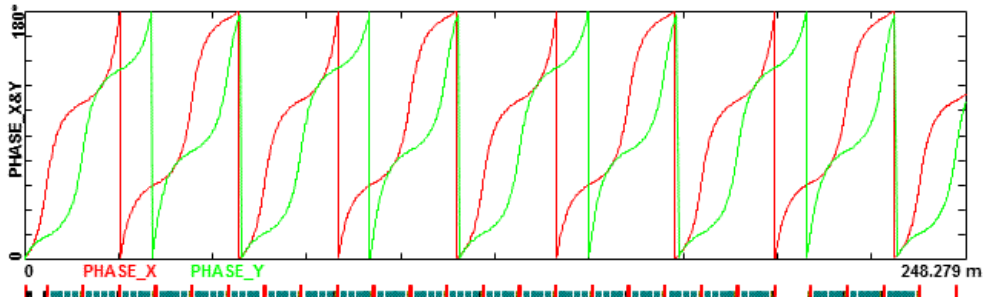

(d) Horizontal (red) and vertical (green) phase advances for the first-pass south linac.

Fig. 4.9: Optics for phase advance 120° setup.

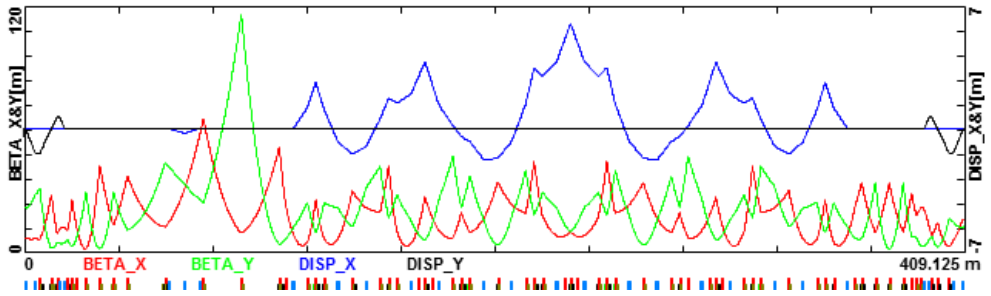

(a) Arc 1.

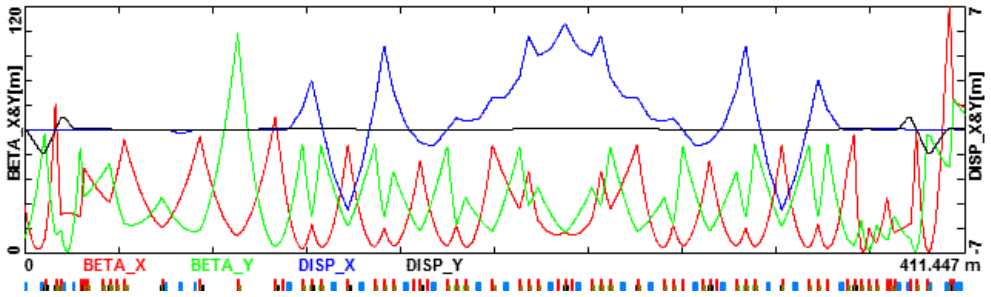

(b) Arc 2.

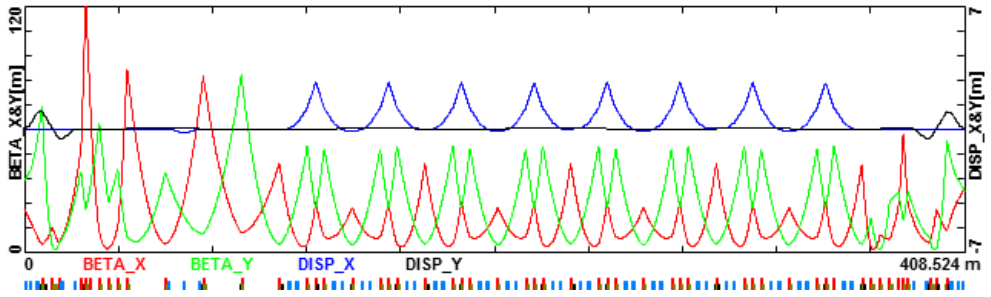

(c) Arc 3.

Fig. 4.10: Optics of arc 1, 2, and 3. Horizontal and vertical beta functions are in red and green respectively. Horizontal and vertical dispersions are in blue and black respectively.

4.4.3 Experimental Setups

After the HOM surveys in the CMTF, the two cryomodules were installed at the end of the CEBAF south linac during the 2011 summer shutdown as part of the 12 GeV Upgrade project at Jefferson Lab. The BTF measurement was performed as shown in Figure 4.11. Table 4.2 lists the experimental configurations.

Pass setup	2 pass
Energy gain/linac	282 MeV
Beam current I	0, 40, 80, 180 μA
Phase advance/cell in linacs	90, 105, 120°

Table 4.2: BBU experimental parameters.

Efforts were made to lower the BBU threshold current, I_{th}, to approach to the actual onset of BBU and hopefully directly observe the BBU phenomena. Since cavity characteristics can not be manipulated during the experiment, the only variables available to lower I_{th} for the BBU experiment are the momentum, p, and the transfer matrix element, M_{12}, in Equation 2.51. Attempts to lower p and thus I_{th} by tuning CEBAF to 150 MeV/linac failed after several attempts because the optics control was not good enough to work at these very low energies. A low-energy setup of 282 MeV/linac (compare to nominal 551 MeV/linac) succeeded, providing p =1160 MeV/c after two passes.

Unfortunately, the Hall C high-current dump was not available, so opera-

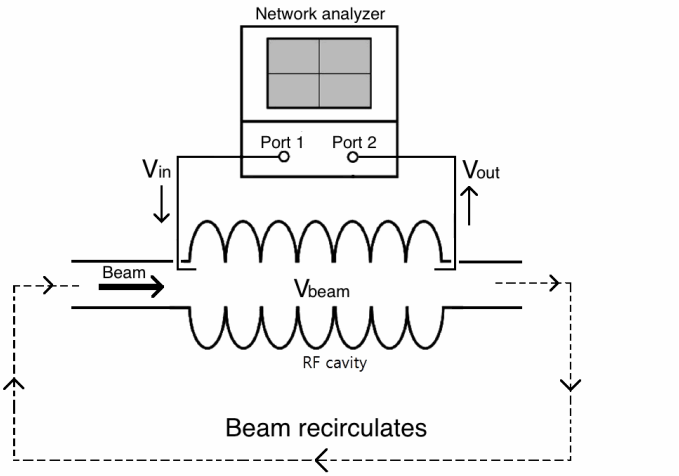

(a) Schematic of beam transfer function measurement

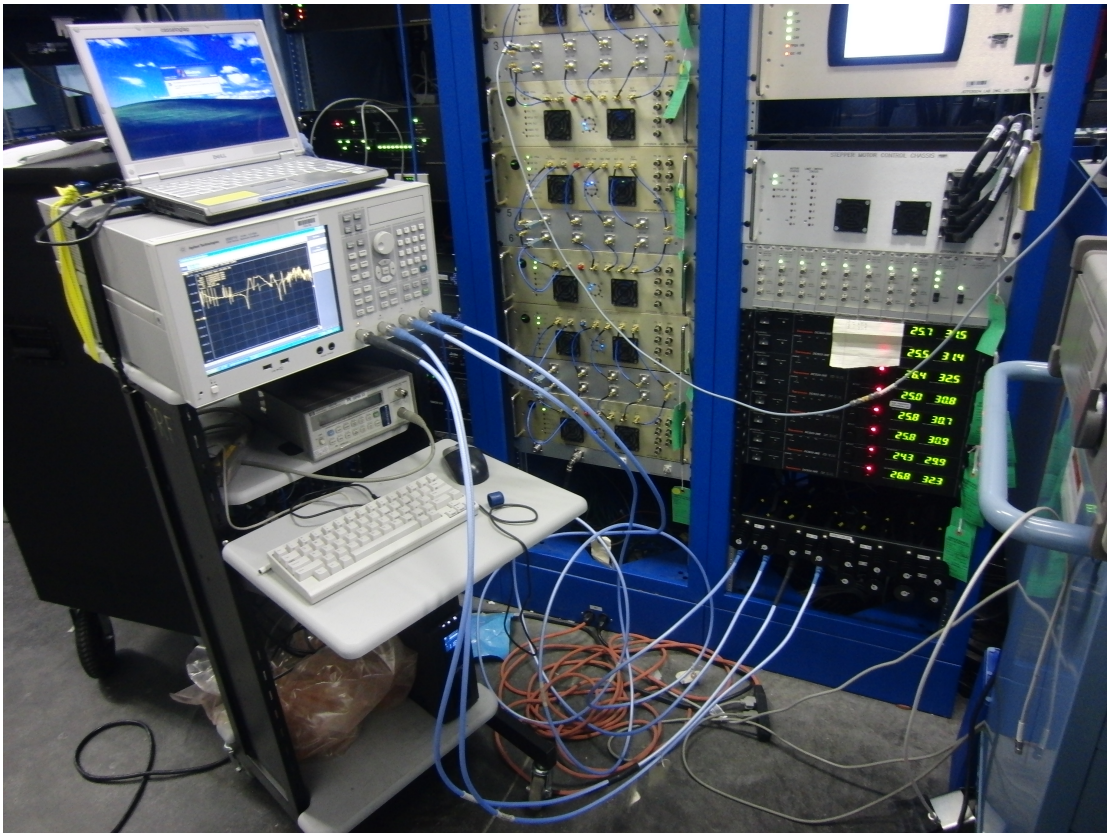

(b) Measurement setup at the Service Building in the South Linac. The cables are connected to the cryomodules in the underground accelerator tunnel.

Fig. 4.11: Measurement setup at the Service Building in the South Linac.

tional beam current was limited to 80 μA. The measurements were performed for beam currents of 40 μA and 80 μA. Later data at 180 μA was acquired parasitically during the CEBAF experimental program. During the experiment, we did not observe any evidence of BBU onset. Note that the experimental beam current is much lower than the analytically estimated threshold currents of about 4.5 mA.

Although multipass BBU is a threshold phenomenon, it is not necessary to exceed the threshold current to measure it. This can be measured by the BTF measurement. The next chapter describes the theoretical background of the data analysis method using the BTF data, followed by the results of data analysis.

Chapter 5

Data Analysis

5.1 Overview

This chapter describes the data analysis method and its theoretical background. By analyzing transmission coefficients of HOMs as a function of beam current, the BBU threshold currents will be obtained. The analysis results will be compared with the simulation results to verify that the 12 GeV Upgrade can be operated with maximum design current without multipass BBU instability.

5.1.1 Analysis Method

Previously, BTF measurements were performed to determine the BBU threshold current for the FEL Upgrade Driver at Jefferson Lab [45, 46]. Figure 5.1a shows an example of the measurements. It is evident that the effective quality factor, Q_{eff}, of the curve increases as the current increases. By measuring Q_{eff} as a function of the beam current, the threshold current can be calculated from the

relation [45, 46]:

$$Q_{\text{eff}} = \left(\frac{I_{th}}{I_{th} - I} \right) Q_L, \tag{5.1}$$

where Q_L is the loaded quality factor without beam. For the BBU experiment, I expected that the same method was applicable to our experiment, but it was not. As seen in Figure 5.1b, the difference in the effective quality factor was difficult to resolve. However, this means that the threshold current is far off from the experimental current of 180 μA. Note that the experimental currents for the FEL Upgrade Driver are within a factor of five from the threshold current, 2.4 mA. From this fact, one can infer that the threshold current for the BBU experiment is much greater than the experimental current of 180 μA.

Even though they are very small, there clearly exists a consistency in the maximum values of the peak as a function of the average beam current as shown in Table 5.1.

Frequency	$S_{21}^{[dB]}$ at I=0	$S_{21}^{[dB]}$ at I=40 μA	$S_{21}^{[dB]}$ at I=80 μA
2891.6840 MHz	-46.4208	-45.9827	-45.9359
2892.0760 MHz	-29.2581	-29.1133	-29.0918

Table 5.1: $S_{21}^{[dB]}$ at different currents for TM_{111} mode of Cavity 1 in C100-1.

Analysis using this maximum peak value was previously performed by Nicholas Sereno for his dissertation in the injector linac recirculator [19], but the experimental setup was different. A stripline kicker made the beam oscillate and the

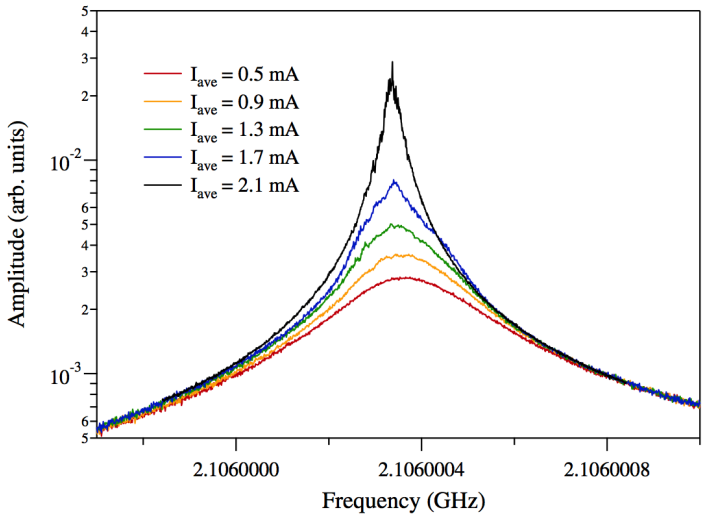

(a) Resonant curve as a function of average beam current in the FEL Upgrade Driver. Note that the lowest beam current is 500 μA and the BBU threshold current is approximately 2.4 mA. (Picture from [46]).

(b) A NWA screen shot of our BBU experiment. Beam on and off data are superimposed. Blue and black lines are measured when beam off; red and magenta lines are measured when a beam current is 180 μA.

Fig. 5.1: Comparison of BTF measurement for the FEL Upgrade Driver and our BBU experiment.

cavity response was measured as a function of the beam current. In our measurement, the experimental setup was simpler because the beam was excited through the HOM port without the stripline kicker.

Due to the different experimental setup, a different formalism for data analysis must be developed. The next sections will theoretically validate the data analysis method for our experiment.

5.2 Data Analysis Theory

5.2.1 HOM Voltages Induced by a NWA and a Beam

As in Figure 5.2, a network analyzer sends a signal, V_{in}, into the cavity and excites an HOM. The beam also excites the HOM. The HOM field kicks the beam, and the HOM kick defines the HOM voltage to be proportional to the kick imparted on the beam as Equation 2.22. The HOM voltage is proportional to the measured signal, V_{out}, at port 2.

Consider a constant of proportionality, α_{in}, which takes into account the transformation efficiency of V_{in} into the HOM field, V_{NWA}. It includes an effective coupling to the HOM field by an HOM coupler antenna and any other cable attenuation factors. The HOM voltage, V_{NWA}, excited by the input signal from a network analyzer may be written as

$$V_{NWA} = \alpha_{in} V_{in}. \tag{5.2}$$

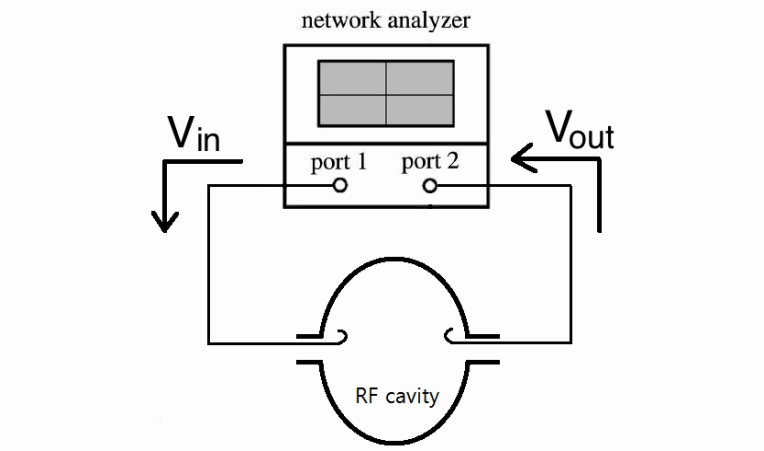

Fig. 5.2: Schematic of the experimental setup for HOM measurements using a network analyzer. The driving signal, V_{in}, from port 1, is sent into the cavity and excites an HOM voltage, V_{NWA}, through an HOM coupler in the cavity. A beam also excites an HOM voltage, V_{beam}. Port 2 measures the output signal, V_{out}, coming out of the cavity through another HOM coupler. The network analyzer measures the transmission parameters, $S_{21} = V_{out}/V_{in}$.

Consider that V_{NWA} is excited in the cavity when a beam is off. Then, the output signal, V_{out}, emerging from the cavity may be expressed by introducing a constant of proportionality, α_{out}, similar to α_{in} in Equation 5.2:

$$V_{out} = \alpha_{out} V_{NWA}. \tag{5.3}$$

The transmission coefficient, $S_{21}|_{I=0}$, when a beam current is $I = 0$, is defined by

$$\begin{aligned} S_{21}|_{I=0} &\equiv \frac{V_{out}}{V_{in}} \\ &= \alpha_{in}\alpha_{out}. \end{aligned} \tag{5.4}$$

When a beam is on, the beam can excite the HOM. The beam-induced voltage, V_{beam}, contributes to the total HOM voltage, V, of the HOM in the cavity:

$$V = V_{NWA} + V_{beam}. \tag{5.5}$$

Considering a constant proportionality, α_{out}, the output signal, V_{out}, is written as

$$\begin{aligned} V_{out} &= \alpha_{out} V & (5.6)\\ &= \alpha_{out}(V_{NWA} + V_{beam}). & (5.7) \end{aligned}$$

The transmission coefficient, $S_{21}|_{I=I_0}$, when a beam current is $I = I_0$, can be written using Equation 5.4:

$$\begin{aligned} S_{21}|_{I=I_0} &\equiv \frac{V_{out}}{V_{in}} & (5.8)\\ &= \alpha_{in}\alpha_{out}\left(1 + \frac{V_{beam}}{V_{NWA}}\right)\\ &= S_{21}|_{I=0}\left(1 + \frac{V_{beam}}{V_{NWA}}\right). & (5.9) \end{aligned}$$

The beam-induced voltage, V_{beam}, contains the BBU threshold information. If V_{beam} can be expressed in terms of the threshold current explicitly, then one may be able to determine the threshold current experimentally. In the next sections, the BBU threshold current will be extracted using Equation 5.9.

In Chapter 2, the instability condition for multipass BBU was found in terms of the wake potential and current moment in the time domain. The analysis in the frequency domain is needed because the RF measurement was performed in the

frequency domain. Hereafter, the calculation of HOM voltage in the frequency domain will be developed to find an analytical expression from which one can extract the threshold current using the experimental data.

5.2.2 HOM Voltage in the Frequency Domain

In this section, the HOM voltage will be obtained in the time domain first, and then it will be transformed into the frequency domain. Shown in Equation 5.5, the HOM voltage, $V(t)$, in the time domain is written as

$$V(t) = V_{NWA}(t) + V_{beam}(t), \tag{5.10}$$

and, by taking the Fourier transform of the above equation, the expression in the frequency domain will be given by

$$\tilde{V}(\omega) = \tilde{V}_{NWA}(\omega) + \tilde{V}_{beam}(\omega), \tag{5.11}$$

where the tilde represents a Fourier transformed function in the frequency domain. The goal of all the calculations in this section is to obtain the $\tilde{V}(\omega)$ in the frequency domain.

Consider the HOM voltage, $V_{NWA}(t)$, generated by the input from an NWA. It may be expressed as

$$V_{NWA}(t) = V_0 \cos(\omega_\lambda t), \tag{5.12}$$

where ω_λ is the HOM frequency, and V_0 is the amplitude of voltage. The Fourier

transform of $V_{NWA}(t)$ is

$$\begin{aligned}\tilde{V}_{NWA}(\omega) &= \int_{-\infty}^{\infty} V_{NWA}(t)\, e^{i\omega t} dt \\ &= \pi V_0 \{\delta(\omega+\omega_\lambda) + \delta(\omega-\omega_\lambda)\}. \end{aligned} \tag{5.13}$$

When a beam enters the cavity on axis and returns to the cavity on the second pass, from Equation 2.35, the HOM voltage, V_{beam}, excited by the beam is

$$V_{beam}(t) = \frac{eM_{12}}{pc} \int_{-\infty}^{t} W(t-t')\, I(t'-T_r)\, V(t'-T_r)\, dt'. \tag{5.14}$$

Letting $\tau = t - t'$ and requiring $W(\tau) = 0$ for $\tau < 0$, $V_{beam}(t)$ is written as

$$\begin{aligned} V_{beam}(t) &= \frac{eM_{12}}{pc} \int_{-\infty}^{\infty} W(\tau)\, I(t-\tau-T_r)\, V(t-\tau-T_r) d\tau \\ &= \frac{eM_{12}}{pc} \int_{-\infty}^{\infty} W(\tau)\, I_V(t-\tau) d\tau \\ &= \frac{eM_{12}}{pc}\, W(t) * I_V(t), \end{aligned} \tag{5.15}$$

where

$$I_V(t-\tau) \equiv I(t-\tau-T_r)\, V(t-\tau-T_r), \tag{5.16}$$

and $W(t) * I_V(t)$ is a convolution:

$$W(t) * I_V(t) \equiv \int_{-\infty}^{\infty} W(\tau)\, I_V(t-\tau) d\tau. \tag{5.17}$$

Taking the Fourier transform of $V_{beam}(t)$ and applying the convolution the-

orem yields

$$\begin{aligned}\tilde{V}_{beam}(\omega) &= \int_{-\infty}^{\infty} V_{beam}(t)e^{i\omega t}dt \\ &= \frac{eM_{12}}{pc}\int_{-\infty}^{\infty} W(t) * I_V(t)\; e^{i\omega t}dt \\ &= \frac{eM_{12}}{pc}\;\tilde{W}(\omega)\;\tilde{I_V}(\omega), \end{aligned} \tag{5.18}$$

where $\tilde{W}(\omega)$ and $\tilde{I_V}(\omega)$ are the Fourier transform of $W(t)$ and $I_V(t)$:

$$\tilde{W}(\omega) = \int_{-\infty}^{\infty} W(t)e^{i\omega t}dt \tag{5.19}$$

$$\tilde{I_V}(\omega) = \int_{-\infty}^{\infty} I_V(t)e^{i\omega t}dt. \tag{5.20}$$

Equation 5.20 can be calculated employing the convolution theorem,

$$\int_{-\infty}^{\infty} I(t)\,V(t)\,e^{i\omega t}dt \;=\; \frac{1}{2\pi}\tilde{I}(\omega) * \tilde{V}(\omega), \tag{5.21}$$

and the relations for currents,

$$I(t) \;=\; I_0 t_0 \sum_{n=-\infty}^{\infty} \delta(t - nt_0) \tag{5.22}$$

$$\begin{aligned}\tilde{I}(\omega) &= \int_{-\infty}^{\infty} I(t)e^{i\omega t}dt \\ &= I_0 t_0 \sum_{n=-\infty}^{\infty} e^{int_0\omega} \\ &= 2\pi I_0 \sum_{n=-\infty}^{\infty} \delta(\omega - n\omega_b), \end{aligned} \tag{5.23}$$

where t_0 is the bunching period, $t_0 = \frac{2\pi}{\omega_b}$, and I_0 is the average beam current.

The Fourier transform of Equation 5.20 becomes:

$$\begin{aligned}
\tilde{I_V}(\omega) &= \int_{-\infty}^{\infty} I_V(t) e^{i\omega t} dt \\
&= \int_{-\infty}^{\infty} I(t-T_r)\, V(t-T_r) e^{i\omega t} dt \\
&= e^{i\omega T_r} \int_{-\infty}^{\infty} I(t-T_r)\, V(t-T_r) e^{i\omega(t-T_r)} dt \\
&= e^{i\omega T_r} \frac{\tilde{I}(\omega) * \tilde{V}(\omega)}{2\pi} \\
&= \frac{e^{i\omega T_r}}{2\pi} \int_{-\infty}^{\infty} \tilde{I}(\omega')\tilde{V}(\omega-\omega') d\omega' \\
&= \frac{e^{i\omega T_r}}{2\pi} \int_{-\infty}^{\infty} 2\pi I_0 \sum_{n=-\infty}^{\infty} \delta(\omega' - n\omega_b)\tilde{V}(\omega-\omega') d\omega' \\
&= I_0 e^{i\omega T_r} \sum_{n=-\infty}^{\infty} \tilde{V}(\omega - n\omega_b). \qquad (5.24)
\end{aligned}$$

Substituting Equation 5.24 into Equation 5.18, the beam-induced HOM voltage, $\tilde{V}_{beam}(\omega)$, is

$$\tilde{V}_{beam}(\omega) = \frac{eM_{12}I_0}{pc} e^{i\omega T_r}\, \tilde{W}(\omega) \sum_{n=-\infty}^{\infty} \tilde{V}(\omega - n\omega_b). \qquad (5.25)$$

Substituting Equation 5.13 and 5.25 into Equation 5.11, the total HOM voltage, $\tilde{V}(\omega)$, in the frequency domain is obtained as

$$\tilde{V}(\omega) = \pi V_0\{\delta(\omega+\omega_\lambda)+\delta(\omega-\omega_\lambda)\} + \frac{I_0 eM_{12}}{pc} e^{i\omega T_r} \tilde{W}(\omega) \sum_{n=-\infty}^{\infty} \tilde{V}(\omega - n\omega_b), \quad (5.26)$$

where $\tilde{V}(\omega)$ is given in terms of itself evaluated at all other harmonics of the bunching frequency. To express the summation term in Equation 5.26 in closed form, the equation is modified in the form of $\tilde{V}(\omega - m\omega_b)$ by substituting $\omega - m\omega_b$

for ω:

$$\begin{aligned}\tilde{V}(\omega - m\omega_b) &= \pi V_0\{\delta(\omega - m\omega_b + \omega_\lambda) + \delta(\omega - m\omega_b - \omega_\lambda)\} \\ &+ \frac{I_0 e M_{12}}{pc} e^{i(\omega - m\omega_b)T_r} \tilde{W}(\omega - m\omega_b) \sum_{n=-\infty}^{\infty} \tilde{V}(\omega - m\omega_b - n\omega_b) \\ &= \pi V_0\{\delta(\omega - m\omega_b + \omega_\lambda) + \delta(\omega - m\omega_b - \omega_\lambda)\} \\ &+ \frac{I_0 e M_{12}}{pc} e^{i\omega T_r} \tilde{W}(\omega - m\omega_b) \sum_{n=-\infty}^{\infty} \tilde{V}(\omega - n\omega_b), \end{aligned} \tag{5.27}$$

where the relations,

$$e^{i(\omega - m\omega_b)T_r} = e^{i\omega T_r} \tag{5.28}$$

$$\sum_{n=-\infty}^{\infty} \tilde{V}(\omega - m\omega_b - n\omega_b) = \sum_{n=-\infty}^{\infty} \tilde{V}(\omega - n\omega_b), \tag{5.29}$$

are used.

Summing up Equation 5.27 over m for all integers, the equation becomes

$$\begin{aligned}\sum_{m=-\infty}^{\infty} \tilde{V}(\omega - m\omega_b) = &\sum_{m=-\infty}^{\infty} \pi V_0\{\delta(\omega - m\omega_b + \omega_\lambda) + \delta(\omega - m\omega_b - \omega_\lambda)\} \\ &+ \frac{I_0 e M_{12}}{pc} e^{i\omega T_r} \sum_{m=-\infty}^{\infty} \tilde{W}(\omega - m\omega_b) \sum_{n=-\infty}^{\infty} \tilde{V}(\omega - n\omega_b). \end{aligned} \tag{5.30}$$

Solving the equation in terms of $\sum_{m=-\infty}^{\infty} \tilde{V}(\omega - m\omega_b)$ produces

$$\sum_{n=-\infty}^{\infty} \tilde{V}(\omega - n\omega_b) = \frac{\sum_{k=-\infty}^{\infty} \pi V_0\{\delta(\omega - k\omega_b + \omega_\lambda) + \delta(\omega - k\omega_b - \omega_\lambda)\}}{1 - \frac{I_0 e M_{12}}{pc} e^{i\omega T_r} \sum_{m=-\infty}^{\infty} \tilde{W}(\omega - m\omega_b)}. \tag{5.31}$$

Finally, by substituting this equation into Equation 5.26, the wake potential in the frequency domain is obtain:

$$\begin{aligned}\tilde{V}(\omega) &= \pi V_0\{\delta(\omega + \omega_\lambda) + \delta(\omega - \omega_\lambda)\} \\ &+ \frac{I_0 e M_{12}}{pc} e^{i\omega T_r} \tilde{W}(\omega) \frac{\sum_{k=-\infty}^{\infty} \pi V_0\{\delta(\omega - k\omega_b + \omega_\lambda) + \delta(\omega - k\omega_b - \omega_\lambda)\}}{1 - \frac{I_0 e M_{12}}{pc} e^{i\omega T_r} \sum_{m=-\infty}^{\infty} \tilde{W}(\omega - m\omega_b)}. \end{aligned} \tag{5.32}$$

Equation 5.32 represents the total HOM voltage. In the next section, the HOM voltage will be expressed in terms of the BBU threshold current, and a data analysis method to determine the threshold current will be described.

5.2.3 Threshold Current in the Frequency Domain

From Equation 2.28, the wake function can be obtained:

$$\begin{aligned}
\tilde{W}_\lambda(\omega) &= \int_{-\infty}^{+\infty} W_\lambda(t)\, e^{i\omega t}\, dt \\
&= \int_{0}^{+\infty} \left(\frac{(R/Q)_\lambda k_\lambda \omega_\lambda}{2}\right) e^{-\frac{\omega_\lambda}{2Q_\lambda}t} \sin(\omega_\lambda t)\, e^{i\omega t}\, dt \\
&= \frac{1}{2}\left(\frac{R}{Q}\right)_\lambda k_\lambda \frac{1}{1-\left(\frac{\omega}{\omega_\lambda}\right)^2 + \frac{1}{4Q_\lambda^2} - \frac{i}{Q_\lambda}\frac{\omega}{\omega_\lambda}} \\
&= \frac{1}{2}\left(\frac{R}{Q}\right)_\lambda Q_\lambda k_\lambda \frac{1}{Q_\lambda\left(1-\left(\frac{\omega}{\omega_\lambda}\right)^2 + \frac{1}{4Q_\lambda^2}\right) - i\frac{\omega}{\omega_\lambda}} \\
&= \frac{1}{2}\left(\frac{R}{Q}\right)_\lambda Q_\lambda k_\lambda \mathcal{A}_\lambda(\omega) e^{-i\phi_\lambda(\omega)}, \qquad (5.33)
\end{aligned}$$

where

$$\mathcal{A}_\lambda(\omega) \equiv \left[Q_\lambda^2\left\{1-\left(\frac{\omega}{\omega_\lambda}\right)^2 + \frac{1}{4Q_\lambda^2}\right\}^2 + \left(\frac{\omega}{\omega_\lambda}\right)^2\right]^{-\frac{1}{2}} \qquad (5.34)$$

$$\phi_\lambda(\omega) \equiv \tan^{-1}\left(\frac{\frac{\omega}{\omega_\lambda}}{Q_\lambda\left(1-\left(\frac{\omega}{\omega_\lambda}\right)^2 + \frac{1}{4Q_\lambda^2}\right)}\right). \qquad (5.35)$$

The resonance condition for an HOM is found by setting the derivative of $\mathcal{A}_\lambda(\omega)$ equal to zero so that on resonance,

$$\frac{\omega_r}{\omega_\lambda} = \sqrt{1-\frac{1}{4Q_\lambda^2}} \tag{5.36}$$

$$\mathcal{A}_\lambda(\omega_r) = 1 \tag{5.37}$$

$$\phi_\lambda(\omega_r) = \tan^{-1}\sqrt{4Q_\lambda^2-1}, \tag{5.38}$$

where ω_λ is an HOM resonant frequency when $Q_\lambda = \infty$, and ω_r is a resonant frequency when Q_λ is finite. At $\omega = \omega_r$, $\mathcal{A}_\lambda(\omega)$ is maximum. Figure 5.3a shows the frequency shift for small Q_λ values, but for $Q_\lambda \gg 1$, the wake function, $\tilde{W}_\lambda(\omega)$, has a maximum peak at $\omega_r \approx \omega_\lambda$ as in Figure 5.3b.

For example, $|\omega_r - \omega_\lambda| \approx 6 \times 10^{-3}$ Hz for 2893 MHz dipole mode with $Q_\lambda = 6.27 \times 10^5$. We can consider $\omega_r \approx \omega_\lambda$ in measurement precision.

An instability results in when the denominator is zero in Equation 5.32:

$$1 - \frac{I_0 e M_{12}}{pc} e^{i\omega T_r} \sum_{m=-\infty}^{\infty} \tilde{W}(\omega - m\omega_b) = 0. \tag{5.39}$$

For a very large Q_λ resonance, the summation of the above equation has an appreciable contribution from only a single term, as shown in Figure 5.4. The wake function is strongly peaked at each HOM frequency. Near a particular HOM frequency, the wake function is dominated by the mode at that frequency and all other modes do not contribute appreciably. In this case, each HOM may be treated individually without contribution from the other HOMs. Therefore, the analytical calculations based on the simple model in Chapter 2 can be applied to

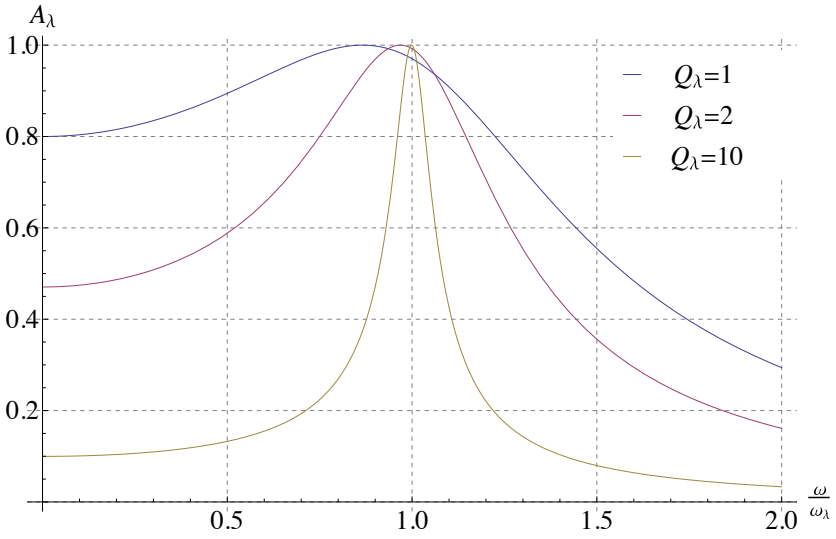

(a) The amplitude $\mathcal{A}_\lambda(\omega)$ of the wake function in Equation 5.34 for three Q_λ values. Note the frequency shift as a function of Q_λ.

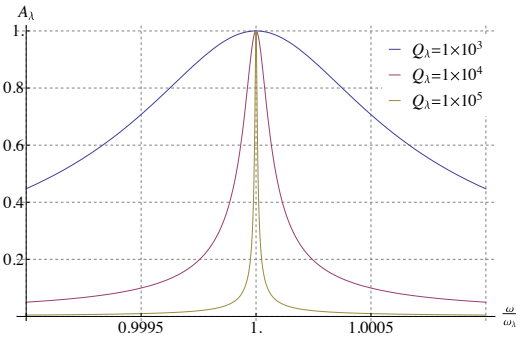

(b) Amplitude $\mathcal{A}_\lambda(\omega)$ versus frequency for three different Q_λ values.

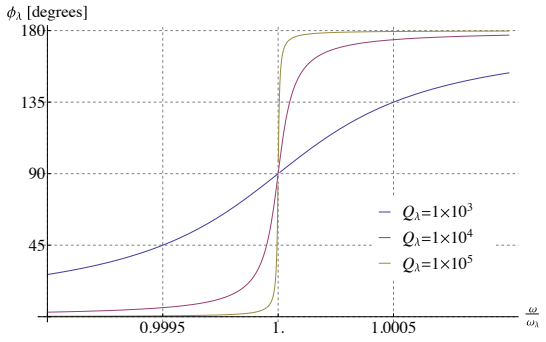

(c) Phase $\phi_\lambda(\omega)$ versus frequency for three different Q_λ values.

Fig. 5.3: The amplitude $\mathcal{A}_\lambda(\omega)$ and phase $\phi_\lambda(\omega)$ of the wake function in Equation 5.34 and 5.35 for different Q_λ values.

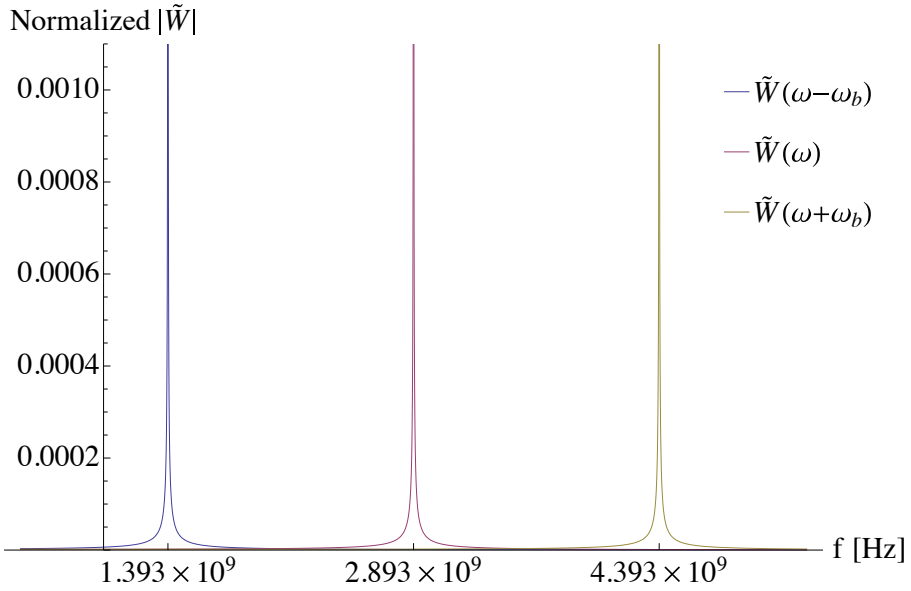

Fig. 5.4: Normalized wake functions, $\tilde{W}_{norm} = \mathcal{A}_\lambda(\omega)e^{-i\phi_\lambda(\omega)}$, around 2893 MHz mode. Note that the y-axis is zoomed in between 0 and 0.001 to easily check on the overlap of the peaks. Each peak is very sharp so that the wake functions, $\tilde{W}$, hardly overlap each other. Only peak dominates the wake function at 2893 MHz. $\omega_b = 2\pi \times 1.5$ GHz, $Q_\lambda = 6.27 \times 10^5$, $(R/Q)_\lambda = 44.8\ \Omega$.

the data analysis. Only one HOM near $\omega \approx \omega_r$ will be considered in the following calculations.

Considering only around $\omega \approx \omega_r$, Equation 5.39 is reduced to:

$$1 - \frac{I_0 e M_{12}}{pc} e^{i\omega T_r} \tilde{W}_\lambda(\omega) = 0. \tag{5.40}$$

Equation 5.40 can be rewritten using Equation 5.33 as

$$1 - \frac{I_0 e M_{12}}{pc} \frac{1}{2} \left(\frac{R}{Q}\right)_\lambda Q_\lambda k_\lambda \mathcal{A}_\lambda(\omega) e^{i(\omega T_r - \phi_\lambda(\omega))} = 0. \tag{5.41}$$

For this equation to be real, the phase term in Equation 5.41 should satisfy a transcendental equation:

$$\omega T_r - \phi_\lambda(\omega) = k\pi, \quad k = \text{integer}. \tag{5.42}$$

This equation is graphically illustrated in Figure 5.5.

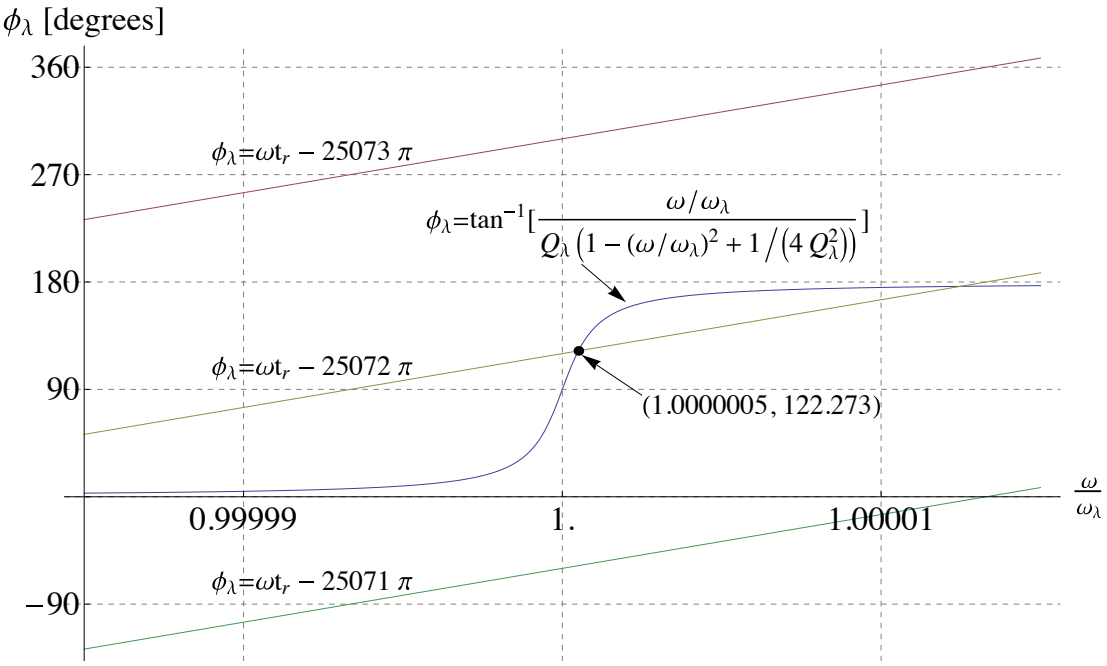

Fig. 5.5: Numerical solution of the transcendental Equation 5.42 for an TM_{111} 2893 MHz mode. There exists a solution near $\frac{\omega_{th}}{\omega_\lambda} = 1.0000005036$ and $\phi_\lambda = 122.173°$ when integer $k = 25072$. The threshold condition frequency, ω_{th}, is different from the mode frequency, ω_r, only by 1457 Hz. One may approximate $\omega_{th} \approx \omega_r$ for this case in I_{th} calculations, but in general the approximation is not valid. More details are discussed in Section 5.2.5.

Let $\omega \equiv \omega_{th}$, which satisfies Equation 5.42, and define $\mathrm{I}_0 \equiv I_{th}$ which satisfies

Equation 5.41 when $\omega = \omega_{th}$. The threshold current, I_{th}, can be expressed from Equation 5.40 and 5.41:

$$I_{th} = \frac{pc/e}{M_{12}e^{i\omega_{th}T_r}\tilde{W}_\lambda(\omega_{th})} \tag{5.43}$$

$$= \frac{2pc/e}{(R/Q)_\lambda Q_\lambda k_\lambda M_{12}\mathcal{A}_\lambda(\omega_{th})}. \tag{5.44}$$

At $\omega = \omega_{th}$, Equation 5.13 becomes

$$\tilde{V}_{NWA}(\omega_{th}) = \pi V_0\{\delta(\omega_{th}+\omega_\lambda) + \delta(\omega_{th}-\omega_\lambda)\}, \tag{5.45}$$

and substituting Equation 5.43 into Equation 5.32 results in

$$\begin{aligned}
\tilde{V}(\omega_{th}) &= \pi V_0\{\delta(\omega_{th}+\omega_\lambda) + \delta(\omega_{th}-\omega_\lambda)\} \\
&+ \frac{I_0 eM_{12}}{pc}e^{i\omega_{th}T_r}\tilde{W}_\lambda(\omega_{th})\frac{\pi V_0\{\delta(\omega_{th}+\omega_\lambda) + \delta(\omega_{th}-\omega_\lambda)\}}{1-\frac{I_0 eM_{12}}{pc}e^{i\omega_{th}T_r}\tilde{W}_\lambda(\omega_{th})} \\
&= \tilde{V}_{NWA}(\omega_{th}) + \tilde{V}_{NWA}(\omega_{th})\frac{\frac{I_0}{I_{th}}}{1-\frac{I_0}{I_{th}}} \\
&= \tilde{V}_{NWA}(\omega_{th})\left(\frac{I_{th}}{I_{th}-I_0}\right).
\end{aligned} \tag{5.46}$$

5.2.4 Threshold Current by NWA Measurement Data

Recall Equation 5.2 and 5.6:

$$\tilde{V}_{NWA} = \alpha_{in}\tilde{V}_{in}$$

$$\tilde{V}_{out} = \alpha_{out}\tilde{V}.$$

Equation 5.46 can be written as

$$\begin{aligned}
\tilde{V}(\omega_{th}) &= \tilde{V}_{NWA}(\omega_{th})\left(\frac{I_{th}}{I_{th}-I_0}\right) \\
\frac{\tilde{V}_{out}(\omega_{th})}{\alpha_{out}} &= \alpha_{in}\tilde{V}_{in}(\omega_{th})\left(\frac{I_{th}}{I_{th}-I_0}\right) \\
\frac{\tilde{V}_{out}(\omega_{th})}{\tilde{V}_{in}(\omega_{th})} &= \alpha_{in}\alpha_{out}\left(\frac{I_{th}}{I_{th}-I_0}\right). \qquad (5.47)
\end{aligned}$$

Recall Equations 5.4 and 5.8:

$$\begin{aligned}
S_{21}|_{I=0} &= \alpha_{in}\alpha_{out} \\
S_{21}|_{I=I_0} &= \frac{\tilde{V}_{out}}{\tilde{V}_{in}}.
\end{aligned}$$

Equation 5.47 becomes

$$\frac{S_{21}(\omega_{th})|_{I=I_0}}{S_{21}(\omega_{th})|_{I=0}} = \frac{I_{th}}{I_{th}-I_0}. \qquad (5.48)$$

Finally, the threshold current, I_{th}, is expressed in terms of measured quantities:

$$I_{th} = \frac{I_0}{1-\frac{S_{21}(\omega_{th})|_{I=0}}{S_{21}(\omega_{th})|_{I=I_0}}}. \qquad (5.49)$$

By measuring S_{21} for two average currents, $I = 0$ and $I = I_0$, the threshold current can be calculated according to Equation 5.49. In practice, it is better for I_0 to be as large as possible in order to obtain better signals. Equation 5.49 agrees with the result of C. M. Lyneis *et al.* [47], where the measurement was performed in the time domain.

For the measurements performed using a NWA, S_{21} was measured in dB

defined as

$$S_{21}(\omega_{th})^{[dB]} \equiv 10\log|S_{21}(\omega_{th})|^2 \tag{5.50}$$

$$= 20\log|S_{21}(\omega_{th})|. \tag{5.51}$$

To utilize the measured values in dB, Equation 5.51 is modified as

$$|S_{21}(\omega_{th})| = 10^{\frac{S_{21}(\omega_{th})^{[dB]}}{20}}, \tag{5.52}$$

and substituting this equation into Equation 5.49 results in

$$I_{th} = \frac{\mathcal{B}}{\mathcal{B}-1}I_0, \tag{5.53}$$

where

$$\mathcal{B} \equiv 10^{\frac{S_{21}(\omega_{th})|_{I=I_0}^{[dB]} - S_{21}(\omega_{th})|_{I=0}^{[dB]}}{20}}. \tag{5.54}$$

Here $S_{21}(\omega_{th})|_{I=I_0}^{[dB]}$ and $S_{21}(\omega_{th})|_{I=0}^{[dB]}$ are the transmission coefficients measured in dB with an NWA when beam current $I = I_0$ and $I = 0$.

It is hard to exactly determine ω_{th} and $S_{21}(\omega_{th})$ experimentally because they depend on Q and the resonant curve is peaked very sharply. Instead, the peak frequency, ω_r, can be used to determine lower bounds of the threshold current as described in the next section.

5.2.5 Data Analysis with Measured Data

As shown in Figure 5.5, the approximation, $\omega_{th} \approx \omega_r$ can not always apply to the I_{th} calculation. However, one may determine a lower bound using ω_r at which the scattering parameter, $|S_{21}|$, has a maximum value.

Recall the threshold current expression, Equation 5.44,

$$I_{th} = \frac{2pc/e}{(R/Q)_\lambda Q_\lambda k_\lambda M_{12} \mathcal{A}_\lambda(\omega_{th})}, \tag{5.55}$$

and define I_{ω_r} as

$$I_{\omega_r} \equiv \frac{2pc/e}{(R/Q)_\lambda Q_\lambda k_\lambda M_{12} \mathcal{A}_\lambda(\omega_r)}. \tag{5.56}$$

Note that

$$\mathcal{A}(\omega_r) \geq \mathcal{A}(\omega_{th}), \tag{5.57}$$

and then

$$I_{\omega_r} \leq I_{th}. \tag{5.58}$$

The resonant frequency, ω_r, can be obtained from the measured data, and I_{ω_r} can be calculated using ω_r. Instead of computing I_{th}, one can determine a lower bound of the threshold current using I_{ω_r}. In the data analysis for this experiment, the resonant frequency, ω_r, was determined by taking the frequency at the measured peak, so there was an uncertainty of about half the spacing between consecutive measurement frequencies in 2 kHz step. The lower bounds of the threshold current were calculated as described in the next section.

5.3 Data Analysis Results

The lower bounds of the threshold current were calculated using two beam currents, 40 μA and 80 μA, as well as zero current S_{21} measurement data. Threshold currents were obtained for HOMs in C100-1, but not for HOMs in C100-2

because the measurement for C100-2 at zero current was not obtained. However, the consistency between C100-1 and C100-2 CMTF survey data in Figure 4.6 provides a good reason not to be concerned about the lack of zero current data for C100-2.

In principle, the threshold current can be calculated using two beam currents data from Equation 5.49, but 40 μA and 80 μA data for C100-2 do not have strong enough signals to produce meaningful consistent results. However, zero current data for C100-1 was obtained, and this data along with 40 μA and 80 μA data provided consistent results. Tables 5.2, 5.3, and 5.4 summarize the lower bounds of threshold currents for the highest impedance HOMs, TM_{111} $\pi/3$ modes in C100-1 cavities at each optical setting. The tables also list the *TDBBU* simulation results for the comparison with the experimental results. All the simulation results are greater than the threshold lower bounds which are experimentally estimated.

TM_{111} horizontal mode in cavity 5 was not able to be resolved because of the overlap of the modes and poor signal-to-noise ratios. This is due to cavity configurations in the cryomodule. Figure 5.6 shows the cavity orientation in the cryomodule.

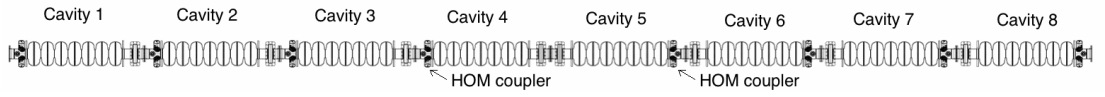

Fig. 5.6: Cavity configuration in C100 cryomodules.

For the first four cavities, the HOM ports are located at the beginning of the

cavity, and the HOM ports are located after the cavities for the last four cavities. No HOM ports exist in between the forth and fifth cavities. This means that, when using a network analyzer to measure HOMs through the HOM ports, one must measure over two cavities. Because of this, the modes were overlapped and signal to noise ratios were worse.

Figure 5.7 shows the threshold current behavior with respect to the HOM frequency. The threshold current is very sensitive and rapidly changes in HOM frequencies. Even though the threshold currents for specific HOM frequencies were simulated as listed in Tables 5.2, 5.3, and 5.4, we should consider the possibility for the threshold current to be lower due to the measurement uncertainty. The lowest threshold current was found to be about 9 mA for TM_{111} $\pi/3$ modes in cavity 2, as shown in Figure 5.7. This is the worst case for the all HOMs, and we can consider 9 mA as the minimum threshold current for the three BBU experimental setups.

By the actual operation, we proved that BBU instability does not occur at 180 μA for the 2-pass, 1.16 GeV setup at the three optical settings; by the experiment, a lower bound estimate based on the experimental results is approximately 2 mA; by the simulations, the threshold current was found to be approximately 9 mA as shown in Figure 5.7, Table 5.2, 5.3, and 5.4. The data from C. Tennant's thesis, as in Figure 5.1a, shows that the peak value goes up quite perceptibly when a current is even within a factor of 5 from the threshold current. This fact

was applied in estimating lower bounds from the experiment. The lower bounds on the threshold currents resulting from the experiment were below the values calculated from the simulations.

These results of measurements and simulations can be used to estimate the threshold current for the 12 GeV Upgrade using the calculated *TDBBU* threshold currents as a figure of merit. From the results of Chapter 3, the threshold current for the 12 GeV Upgrade is inferred to be approximately 4.5 mA. We may conclude that the actual BBU threshold current is greater than the maximum designed current of 80 μA. It is noted that all of these estimates are based on the assumption that the theoretical description of BBU by *TDBBU* is valid.

Phase advance 90° setup			
Cavity number	Frequency [MHz]	I_{ω_r} [mA] (measurement)	I_{th} [mA] (simulation)
cavity 1	2891.6840	1.73	85
	2892.0760	4.22	2910
cavity 2	2890.8520	1.53	330
	2891.0920	0.94	820
cavity 3	2895.1525	0.39	370
	2895.4195	0.34	2920
cavity 4	2892.4668	0.71	320
	2892.5292	2.33	310
cavity 5	2892.6436	0.67	380
cavity 6	2893.1055	2.12	17
	2893.4960	0.20	36
cavity 7	2894.6274	1.12	125
	2894.7652	0.95	255
cavity 8	2895.0380	2.30	235
	2895.1340	8.79	245

Table 5.2: Threshold currents from the BBU experiment and simulations for phase advance 90° setup. I_{ω_r} is the lower bound of the threshold current estimated from the experiment, and I_{th} is the threshold current from simulations.

Phase advance 105° setup			
Cavity number	Frequency [MHz]	I_{ω_r} [mA] (measurement)	I_{th} [mA] (simulation)
cavity 1	2891.6840	1.99	240
	2892.0760	10.63	2400
cavity 2	2890.8520	1.65	10
	2891.0920	0.86	1390
cavity 3	2895.1525	0.37	100
	2895.4195	0.48	3030
cavity 4	2892.4668	0.73	22
	2892.5292	4.68	2800
cavity 5	2892.6436	0.99	105
cavity 6	2893.1055	2.44	320
	2893.4960	0.65	345
cavity 7	2894.6274	2.15	540
	2894.7652	2.97	20
cavity 8	2895.0380	2.38	1850
	2895.1340	5.43	95

Table 5.3: Threshold currents from the BBU experiment and simulations for phase advance 105° setup.

Phase advance 120° setup			
Cavity number	Frequency [MHz]	I_{ω_r} [mA] (measurement)	I_{th} [mA] (simulation)
cavity 1	2891.6840	1.43	770
	2892.0760	3.18	1360
cavity 2	2890.8520	0.67	75
	2891.0920	4.55	1210
cavity 3	2895.1525	1.48	720
	2895.4195	1.71	1120
cavity 4	2892.4668	0.47	150
	2892.5292	1.93	175
cavity 5	2892.6436	0.92	570
cavity 6	2893.1055	10.71	90
	2893.4960	1.13	28
cavity 7	2894.6274	6.95	1850
	2894.7652	3.87	225
cavity 8	2895.0380	3.22	1720
	2895.1340	1.50	235

Table 5.4: Threshold currents from the BBU experiment and simulations for phase advance 120° setup.

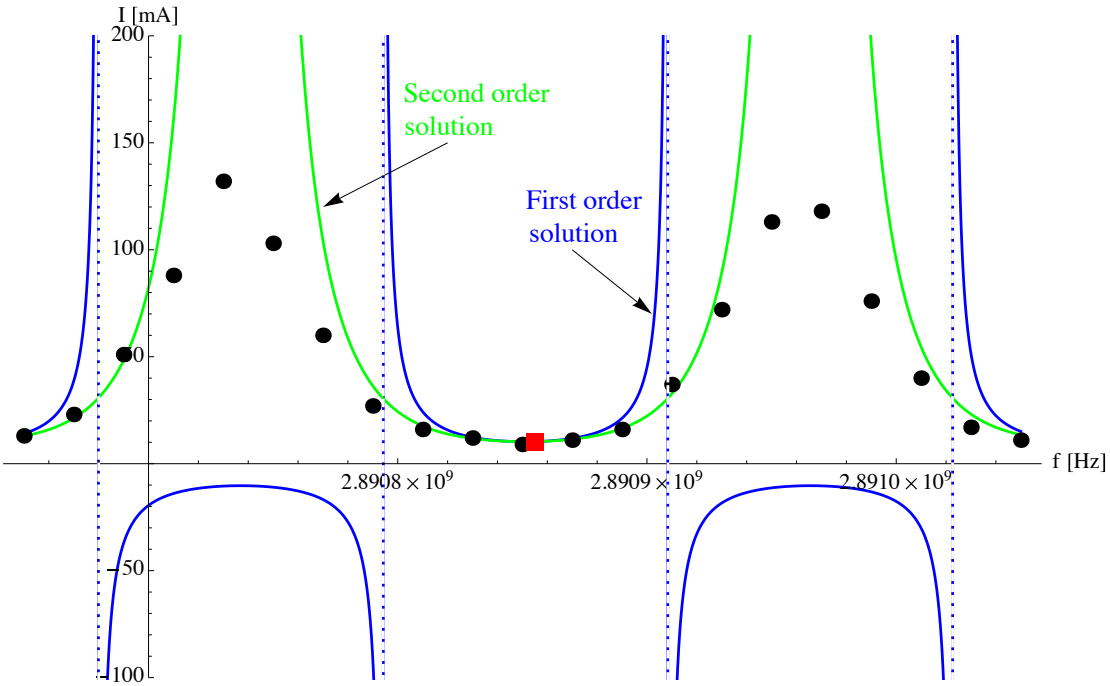

Fig. 5.7: Threshold current behavior around 2890.8520 MHz TM_{111} $\pi/3$ mode in cavity 2 for the 105° optics setup. The black points and red rectangle are TDBBU simulation results. The red rectangle indicates a simulated threshold current of 10 mA at 2890.8520 MHz. The blue and green lines are first and second order solutions of Equations 2.51 and 2.54. In this case, the threshold current is very close to the minimum value of approximately 9 mA, but in general it is not. One should consider this behavior in estimating BBU threshold currents.

Chapter 6

Conclusions

The experimental study of multipass BBU was performed to determine possible machine performance limitations for the 12 GeV Upgrade accelerator. A simulation study also was carried out using computer programs, *TDBBU* and *MATBBU*. These results indicated that the multipass BBU would not occur in the 12 GeV CEBAF accelerator at the maximum design current of 80 μA. The threshold current from simulations is approximately 4.5 mA in support of the BBU experiment. Even though C100-2 was not fully analyzed, the consistency of the CMTF data between C100-1 and C100-2 justifies that both cryomodule satisfies the 12 GeV HOM specifications.

A similar measurement method was used to determine the threshold current by Nicholas Sereno [19] using the CEBAF injector recirculator, where a kicker was used to excite a beam and cavity HOMs. In our experiment, the cavity was excited directly using an NWA with an HOM coupler as an input antenna. The HOM signal was then detected using another HOM coupler in a neighboring cavity as

an output antenna. The method using HOM couplers substantially simplified the data analysis as well as the experimental setup and measurements. Based on Nicholas Sereno's work, I derived the formula for the BBU threshold current in the frequency domain, Equation 5.49, which agrees with the result of C. M. Lyneis *et al.* in the time domain [47]. Since the BBU experiment operated far from threshold currents, the previous data analysis method by C. Tennant [45] was not applicable to this experiment. I developed a formalism to determine threshold lower bounds, Equation 5.58.

To examine the applicability of DBA arc optics to the 12 GeV Upgrade, simulation studies of the BBU instability were performed. Additionally, these studies allowed for investigation as to the availability of the maximum beam current for the 6.6 GeV beam in the 12 GeV accelerator. The work for the DBA arc optics revealed that the DBA arc optics is applicable to the 12 GeV Upgrade within the extent of the HOM damping requirements for the standard 4 GeV arc optics.

For 6.6 GeV beam in the 12 GeV accelerator, two setups were considered: the 3-pass, 6.6 GeV and 5-pass, 6.6 GeV setups. The maximum beam dump power, 1 MW, limits the maximum beam current to 151 μA; the 3-pass, 6.6 GeV setup is able to use the maximum beam current without the occurrence of BBU instability. A simulation study of cumulative BBU for the 12 GeV injector prototype was performed. The results revealed that the transient behavior amplitude is not a concern at all even in extreme cases.

The theoretical calculation for longitudinal BBU showed that longitudinal BBU is not a problem as long as the HOM damping requirements for transverse BBU are met. The longitudinal damping requirements are more than two orders of magnitude greater than the transverse, even in very conservative choice of the parameters.

Bibliography

[1] C. Leemann, D. Douglas, and G. A. Krafft, "THE CONTINUOUS ELECTRON BEAM ACCELERATOR FACILITY: CEBAF at the Jefferson Laboratory," *Annu. Rev. Nucl. Part. Sci.*, vol. 51, pp. 413–450, 2001.

[2] CAS, "CERN Accelerator School 2003 ." CERN, 2003.

[3] G. Hoffstaetter and I. Bazarov, "Beam-breakup Instability Theory for Energy Recovery Linacs," *Phys. Rev. ST Accel. Beams*, vol. 7, p. 054401, May 2004.

[4] N. Nakamura, "Review of ERL Projects at KEK and Around the World," in *IPAC 2012*, (New Orleans, LA), 2012.

[5] R. E. Rand, *Recirculating Electron Accelerators*. New York: Harwood Academic Publishers, 1984.

[6] G. A. Krafft, J. J. Bisognano, and S. Laubach, "Calculating Beam Breakup in Superconducting Linear Accelerators," Tech. Rep. Unpublished, Thomas Jefferson Accelerator Facility.

[7] R. Kazimi, A. P. Freyberger, C. Hovater, G. A. Krafft, F. Marhauser, T. E. Plawski, C. E. Reece, J. S. Sekutowicz, C. Tennant, M. G. Tiefenback, and H. Wang, "Observation and Mitigation of Multipass BBU in CEBAF," in *EPAC 2008*, (Genoa, Italy), 2008.

[8] F. Marhauser, J. Henry, and H. Wang, "Critical Dipole Modes in JLab Upgrade Cavities," in *Linac 2010*, (Tsukuba, Japan), Oct. 2010.

[9] R. L. Gluckstern, R. K. Cooper, and P. J. Channell, "CUMULATIVE BEAM BREAKUP IN RF LINACS," *Particle Accelerators*, vol. 16, pp. 125–153, 1985.

[10] T. P. Wangler, *RF Linear Accelerators*. Weinheim: WILEY-VCH Verlag Gmbh & Co. KGaA, 2 ed., 2008.

[11] S. Ahmed, I. Shin, R. Kazimi, F. Marhauser, F. Hannon, A. S. Hofler, G. A. Krafft, B. Yunn, and A. Hofler, "Beam Breakup Studies for New Cryo-Unit," in *PAC 2011*, (New York, NY), 2011.

[12] J. D. Jackson, "Classical Electrodynamics," John Wiley & Sons, Inc., 1999.

[13] F. Marhauser and H. Wang, "HOM Survey of Low Loss Seven Cell Cavities for theCEBAF 12 GeV Upgrade," Tech. Rep. JLAB-TN-08-37, 2008.

[14] H. Padamsee, J. Knobloch, and T. Hays, *RF Superconductivity for Accelerators*. Weinheim: WILEY-VCH Verlag Gmbh & Co. KGaA, 2 ed., 2008.

[15] P. B. Wilson, "Introduction to wakefields and wake potentials," in *AIP Conf. Proc.*, pp. 525–564, AIP, 1989.

[16] P. B. Wilson, "High Energy Electron Linac: Applications to Storage Ring RF Systems and Linear Colliders," Tech. Rep. SLAC-PUB-2884 (Rev.), 1991.

[17] E. U. Condon, "Forced Oscillations in Cavity Resonators," *Journal of Applied Physics*, vol. 12, no. 2, pp. 129–132, 1941.

[18] B. Yunn, "Expressions for the threshold current of multipass beam breakup in recirculating linacs from single cavity models," *Phys. Rev. ST Accel. Beams*, vol. 8, p. 104401, Oct. 2005.

[19] N. Sereno, *EXPERIMENTAL STUDIES OF MULTIPASS BEAM BREAKUP AND ENERGY RECOVERY USING THE CEBAF INJECTOR LINAC*. PhD thesis, University of Illinois at Urbana-Champaign, 1994.

[20] J. J. Bisognano and M. L. Fripp, "Requirements for Longitudinal HOM Damping in Superconducting Recirculating Linacs," Tech. Rep. CEBAF-PR-89-018, Thomas Jefferson Accelerator Facility, 1989.

[21] C. Song and G. H. Hoffstaetter, "Longitudinal BBU Threshold Current in Recirculating Linacs," Tech. Rep. Cornell-ERL-06-04, 2006.

[22] G. A. Krafft and J. J. Bisognano, "Two Dimensional Simulations of Multipass Beam Breakup," in *PAC 1987*, p. 1356, 1987.

[23] J. J. Bisognano and R. L. Gluckstern, "Multipass beam breakup in recirculating linacs," in *PAC 1987*, p. 6, 1987.

[24] K. Beard, L. Merminga, and B. Yunn, "Tools to predict beam breakup in recirculating linacs," in *PAC 2003*, (Portland, OR), 2003.

[25] K. L. Brown, F. Rothacker, and D. C. Carey, *THIRD-ORDER TRANSPORT: A COMPUTER PROGRAM FOR DESIGNING CHARGED PARTICLE BEAM TRANSPORT SYSTEMS*, 1995.

[26] M. Borland, *User's Manual for elegant*, 2012.

[27] S. C. Hartman and J. B. Rosenzweig, "Ponderomotive focusing in axisymmetric rf linacs," *Physical Review E*, vol. 47, pp. 2031–2037, 1993.

[28] R. H. Helm and R. Miller, "Linear Accelerators," p. 115, 1970.

[29] J. Rosenzweig and L. Serafini, "Transverse particle motion in radio-frequency linear accelerators," *Physical Review E*, vol. 49, no. 2, pp. 1599–1602, 1994.

[30] P. Piot and G. A. Krafft, "Transverse RF Focussing in Jefferson Lab Superconducting Cavities," in *EPAC 1998*, (Stockholm, Sweden), 1998.

[31] I. Shin, T. Satogata, B. C. Yunn, and S. Ahmed, "Comparison of RF Cavity Transport Models for BBU Simulations," *IPAC 2011*, 2011.

[32] B. C. Yunn, "HOM DAMPING REQUIREMENT FOR 12 GeV UPGRADE," Tech. Rep. JLAB-TN-04-035, Jefferson Lab, 2004.

[33] A. Bogacz, "Double Bend Achromat Arc Optics for 12 GeV CEBAF," Tech. Rep. JLAB-TN-07-010, 2007.

[34] D. Douglas, "CEBAF-ER: An Energy Recovery and Current Doubleing Operational Mode for the Continuous Electron Beam Accelerator Facility," Tech. Rep. JLAB-TN-01-045, 2001.

[35] P. B. Wilson, "A Simple Analysis of Cumulative Beam Breakup for the Steady-State Case," Tech. Rep. HEPL-TN-67-8, 1967.

[36] R. L. Gluckstern, F. Neri, and R. K. Cooper, "CUMULATIVE BEAM BREAKUP WITH RANDOMLY FLUCTUATING PARAMETERS," *Particle Accelerators*, vol. 23, pp. 37–52, 1988.

[37] A. W. Chao, *Physics of Collective Beam Instabilities in High Energy Accelerators*. John Wiley & Sons, Inc., 1993.

[38] J. Byrd and F. Casper, "Beam Measurement." World Scientific Pub Co Inc, 1999.

[39] R. E. Collin, *Foundations for Microwave Engineering*. Wiley-IEEE Press, 2001.

[40] W. Fang, W. Er-Dong, Z. Bao-Cheng, and Z. Kui, "Measuring the performance of the coaxial HOM coupler on a 2-cell TESLA-shape copper cavity," *Chinese Physics C*, vol. 33, no. 6, pp. 440–443, 2009.

[41] F. Marhauser and K. Tian, "Optimization of the Cryomodule Cold-to-Warm Transitions and the VTA QA Test Configurationfor CEBAF Upgrade Cavitieswith Regard to Critical HOMs above Cutoff," Tech. Rep. JLAB-TN-09-61, 2009.

[42] C. Potratz, H. W. Glock, V. Kornilov, and F. Marhauser, "AUTOMATIC POLE AND Q-VALUE EXTRACTION FOR RF STRUCTURES," in *IPAC 2011*, (New York, NY), 2011.

[43] J. Borer, G. Guignard, A. Hofmann, E. Peschardt, F. Sacherer, and B. Zotter, "INFORMATION FROM BEAM RESPONSE TO LONGITUDINAL AND TRANSVERSE EXCITATION," in *PAC 1979*, pp. 1–4, 1979.

[44] V. Kornilov, O. Boine-Frankenheim, W. Kaufmann, and P. Moritz, "Measurements and Analysis of the Transverse Beam Transfer Function (BTF) at the SIS 18 Synchrotron," Tech. Rep. GSI-Acc-Note-2006-12-001, GSI, Dec. 2012.

[45] D. Douglas, K. Jordan, L. Merminga, E. Pozdeyev, C. Tennant, H. Wang, T. Smith, S. Simrock, I. Bazarov, and G. Hoffstaetter, "Experimental investigation of multibunch, multipass beam breakup in the Jefferson Laboratory Free Electron Laser Upgrade Driver," *Phys. Rev. ST Accel. Beams*, vol. 9, p. 064403, June 2006.

[46] C. Tennant, *Studies of Energy Recovery Linacs at Jefferson Laboratory*. PhD thesis, College of William and Mary, 2006.

[47] C. M. Lyneis, R. E. Rand, H. A. Schwettman, and A. M. Vetter, "STANDING WAVE MODEL OF REGENERATIVE BEAM BREAKUP IN RECIRCULATING ELECTRON ACCELERATORS," *Nucl Instrum Meth*, vol. 204, pp. 269–284, 1983.

[48] S. A. Bogacz, I. Shin, D. Schulte, and F. Zimmermann, "LHeC ERL Design and Beam-dynamics Issues," in *IPAC 2011*, (New York, NY), 2011.

[49] D. Douglas, W. Akers, S. Benson, G. Biallas, K. Blackburn, J. Boyce, B. Bullard, J. Coleman, C. Dickover, F. Ellingsworth, P. Evtushenko, S. Fisk, C. Gould, J. Gubeli, F. Hannon, D. Hardy, C. Hernandez-Garcia, K. Jordan, M. Klopf, J. Kortze, R. Legg, R. Li, M. Marchlik, W. Moore, G. Neil, T. Powers, D. Sexton, I. Shin, M. Shinn, C. Tennant, B. Terzic, R. Walker,

G. Williams, G. Wilson, and S. Zhang, "USE OF MULTIPASS RECIRCULATION AND ENERGY RECOVERY IN CW SRF X-FEL DRIVER ACCELERATORS," in *FEL 2010*, (Malmö, Sweden), 2010.

[50] I. Shin and B. Yunn, "Beam breakup study for JLAMP," Tech. Rep. JLAB-TN-10-033, 2010.

Appendix A

BBU Simulations for LHeC at CERN

The LHeC is a proposed colliding beam facility at CERN. A new electron

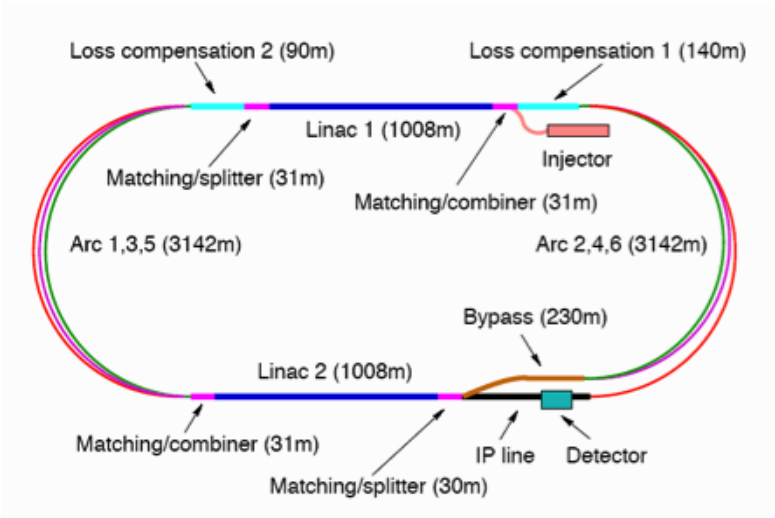

Fig. A.1: Schematic of the energy recovery linac in the LHeC.

accelerator is to be added to the exiting LHC, and an electron beam collides with a proton or a heavy ion beam of the LHC. One of the electron accelerator options is an energy recovery linac, for which BBU simulation study was conducted [48].

The ERL LHeC is designed in 720 MHz cw mode, but a real cavity does not manufactured yet. The BNL3 5-cell SRF cavity data would be good reference for HOM data even though BNL3 fundamental mode frequency, 703.79 MHz, is

slightly different from LHeC RF frequency. Table A.1 lists HOM parameters used for simulations. These modes have relatively high R/Q modes.

f [MHz]	Q_L	R/Q [Ω]
1003	1×10^6	32
1337	1×10^6	32
1820	1×10^6	32

Table A.1: HOM parameters used for LHeC simulations.

Even though the HOM data were really conservative and were obtained for the worst cases (highest Q and highest R/Q), the threshold current is about 5 mA. This result suggests that it is feasible to achieve the design current, 6 mA, if Q_L is damped to the order of 10^5.

Injection energy to linac	0.5 GeV
Energy gain per linac	10 GeV
Maximum beam energy	60.5 GeV
Total number of passes	3 up + 3 down
Start of energy recovery	4th passes
RF frequency	720 MHz
Bunching frequency	720 MHz

Table A.2: Accelerator parameters used for LHeC simulations.

Appendix B

BBU Simulations for JLAMP at Jefferson Lab

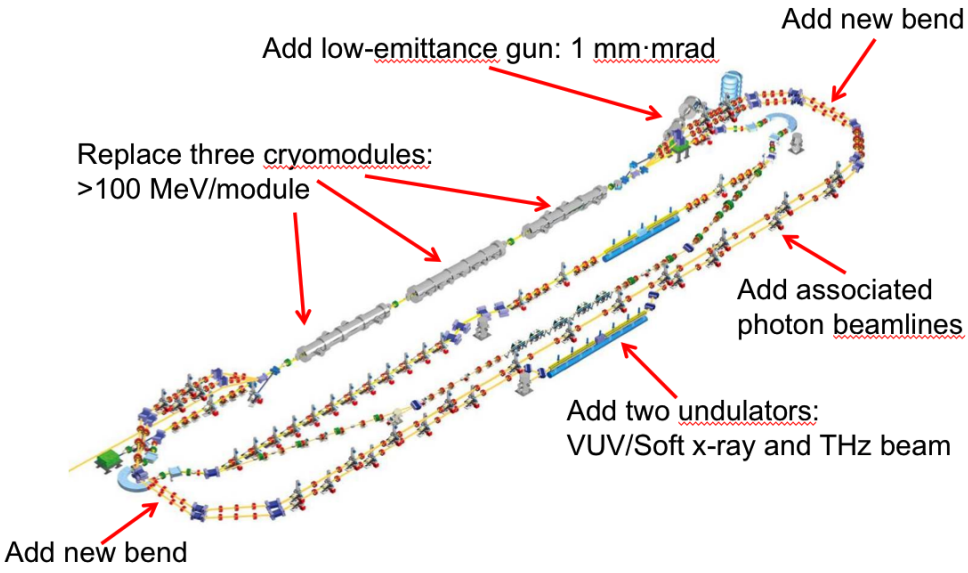

Fig. B.1: Schematic of the JLAMP. The inner beamline is the existing FEL. New JLAMP beamline is outer one.

The JLAMP(**JL**ab **AMP**lifier) is a 4th generation light source proposed by Jefferson Lab. A BBU simulation study for the JLAMP was performed with *TDBBU* using the C100 cavity data which will be used for the 12 GeV CEBAF Upgrade [49,50]. Table B.1 lists parameters used for the simulations. The simula-

tion results state that the lowest threshold current is about 0.67 mA which is lower than the designed current, 1 mA. This means that a stricter damping requirement or a cure on the beam optics is needed to increase the threshold current.

Injection energy	10 MeV
Energy gain for a pass	307.5 MeV
Maximum beam energy	625 MeV
Total number of passes	4 passes
Start of energy recovery	3rd pass
RF frequency	1497 MHz
Bunching frequency	1497 MHz/320 = 4.678 MHz

Table B.1: Accelerator parameters used for JLAMP simulations.